

SIGNATURES OF NONCLASSICAL EFFECTS IN TOMOGRAMS

A THESIS

submitted by

B. SHARMILA

for the award of the degree

of

DOCTOR OF PHILOSOPHY



**DEPARTMENT OF PHYSICS
INDIAN INSTITUTE OF TECHNOLOGY MADRAS
SEPTEMBER 2020**

THESIS CERTIFICATE

This is to certify that the thesis entitled **Signatures of nonclassical effects in tomograms**, submitted by **B. Sharmila** to the Indian Institute of Technology Madras for the award of the degree of **Doctor of Philosophy**, is a bona fide record of the research work done by her under my supervision. The contents of this thesis, in full or in part, have not been submitted to any other Institute or University for the award of any degree or diploma.

Prof. S. Lakshmi Bala

Thesis Guide and Professor

Dept. of Physics

IIT Madras

Place: Chennai, India.

Date: September 22, 2020

ACKNOWLEDGMENTS

I shall remain eternally grateful to my guide Dr. S. Lakshmi Bala, for teaching me to think independently and analyse critically anything presented to me, both academically and otherwise. She has been a pillar of support through my tough times. I aspire to achieve her level of dedication, expertise in a variety of topics, and attention to detail. She has been a source of inspiration, encouragement and advice. Her constructive criticisms have always helped me understand my limitations and build upon my strengths. There will never be enough words or actions to express my gratitude.

I am blessed to have had the opportunity to work with Dr. V. Balakrishnan. Every interaction with him has been an enriching experience. I have benefitted immensely from his teaching and meticulous attention to detail. I shall cherish every one of his witty remarks and his kind words of advice. I sincerely hope that some day I will be able to inspire at least one student as much as he has inspired me. It has been my great privilege to have been taught and mentored by him.

I am extremely grateful to my doctoral committee members - Dr. Suresh Govindarajan, Dr. Sunethra Ramanan and Dr. R. Radha, for their discussions, feedback and constant support. I especially gained a lot from regular interactions with Dr. Suresh Govindarajan and Dr. Sunethra Ramanan. I am grateful for all the encouragement and advice from my doctoral committee chairman, Dr. M. V. Satyanarayana. Since the time I had first met him as an undergraduate student, he had always encouraged me to work harder. My learning as a research scholar has been enhanced by all the inputs that I have received from Dr. Arul Lakshminarayan, Dr. Prabha Mandayam and Dr. Rajesh Narayanan. It is my pleasure to have known Dr. M. S. Sriram and Dr. Radha Balakrishnan, and I thank them for their support and encouragement.

I am grateful to Dr. K. Sethupathi, Head of the Department of Physics, and Dr. M. S. R. Rao and Dr. P. B. Sunil Kumar, former Heads of the Department of Physics, for their kind help and advice during my doctoral programme. I am thankful to IIT Madras for providing generous financial support and excellent departmental and central computing

facilities. I also thank Dr. Sunethra Ramanan for allowing me access to the computing facility of her research group, whenever it was necessary. I thank the IITM Alumni Association for providing partial financial support to attend the conference ‘Quantum Information and Measurement (QIM V) 2019’ in Rome, Italy.

I take this opportunity to thank Prof. Prasanta Panigrahi, IISER Kolkata, for useful discussions and suggestions regarding my work. In Chapter 5 of this thesis, I have used experimental data supplied by the NMR-QIP group, IISER Pune, India. I acknowledge with thanks that these raw experimental data helped me in my study of spin systems. I thank Prof. T. S. Mahesh and the NMR-QIP group for their help. I also personally thank Mr. Soham Pal for discussions and clarifications regarding the experiment.

I have gained a fantastic set of friends in my office mates. I am especially thankful to Pradip Laha for all the help and discussions, academic and otherwise. As a senior, Pradip is the best one could ask for, and as a friend, he and his wife were most supportive and encouraging. I had the best fun and learnt a lot at the same time with Sashi, Sarath, Swaminath and Malayaja. Be it coding, networking in a conference, or binge-watching a sitcom series, I will always remember their tips and encouragement. I also thank Athreya Shankar for discussions and feedback on my work. I take this opportunity to thank Sutapa, Tanya, Akshaya, Vasumathi, Sai Smruti and Madhuparna for all our academic discussions and chit-chat that kept me going through thick and thin. I also thank my juniors, Soumyabrata Paul and Vishnu, for discussions.

I also take this opportunity to express my gratitude to all my teachers. Specifically, I shall always be grateful to my science teacher Mrs. Hemalatha Murthy, (Late) Dr. Nirupama Raghavan, and Dr. N. Lakshminarayanan, for inspiring me to choose physics and work in it.

I thank my best friend Shakthi, for her unconditional support and presence in the darkest hours of need. A ‘Thank you’ is insufficient and, according to my parents, unnecessary, for all their support, encouragement, love and frank criticisms. It is not in my power to ever finish thanking my parents for all that they have done for me. I thank God for having blessed me with all these people who have made this journey not only possible but incredibly enjoyable.

ABSTRACT

KEYWORDS: Tomograms; full and fractional revivals; super-revivals; quadrature, higher-order, entropic and spin squeezing; entanglement; tomographic entanglement indicators; mutual information; participation ratio; Bhattacharyya distance; Pearson correlation coefficient; avoided energy-level crossings; Bose-Einstein condensate; atom-field interaction models; IBM quantum computer; NMR; chronocyclic tomograms; local Lyapunov exponents.

Investigations on nonclassical effects such as revivals, squeezing and entanglement in quantum systems require, in general, knowledge of the state of the system as it evolves in time. The state (equivalently, the density matrix) is reconstructed from a tomogram obtained from experiments. A tomogram is a set of histograms of appropriately chosen observables. Reconstruction of the quantum state from a tomogram typically involves statistical procedures that could be cumbersome and inherently error-prone. It is therefore desirable to extract as much information as possible about the properties of the state *directly* from the tomogram. The theme of this thesis is the identification and quantification of nonclassical effects from appropriate tomograms. We have examined continuous-variable (CV) systems, hybrid quantum (HQ) systems and spin systems. The program is two-fold: (a) To compute tomograms of known states numerically at various instants during temporal evolution under specific Hamiltonians, and to examine their revival, squeezing and entanglement properties at these instants; (b) to compute tomograms from available experimental data, and to investigate their nonclassical features. The CV systems considered are primarily (i) a Bose-Einstein condensate (BEC) trapped in a double-well potential, and (ii) a radiation field interacting with a nonlinear multi-level atomic medium. The HQ systems considered are two-level atoms interacting with radiation fields. This allows for the possibility of examining both optical tomograms and qubit tomograms. Several initial states have been considered, including the standard coherent state (CS), the two-mode squeezed state, the binomial state, and

states which display quantifiable departure from coherence, such as the photon-added coherent state and the boson-added coherent state.

Wave packet revival phenomena including full, fractional and super-revivals have been examined tomographically in the context of a single-mode field system and the bipartite BEC system. Squeezing properties such as quadrature, higher-order Hong-Mandel and Hillery-type squeezing, and entropic squeezing have been investigated in detail in CV systems by evaluating appropriate moments of observables, from tomograms. A major part of the thesis is devoted to a comparison between the performance of different entanglement indicators (computed from tomograms) that we have proposed.

We have also obtained and examined tomograms directly related to experiments reported in the literature. (i) We have analysed appropriate tomograms to distinguish between two 2-photon states produced in an experiment on a CV bipartite system. While photon coincidence count measurements were used for this purpose in the experiment, our investigation demonstrates that tomograms provide another powerful tool for examining differences between various quantum states. (ii) We have computed spin tomograms from data, obtained using liquid-state NMR techniques, from an experimental group. (iii) Equivalent circuits of multipartite HQ systems were provided by us to the IBM quantum computing platform. Based on these circuits, tomograms were generated by the platform by experiment as well as simulation. Corresponding tomograms were computed by us using the HQ model. The entanglement indicators calculated from these three sources of tomograms have been compared and contrasted.

The thesis highlights and elaborates upon the very useful and significant role played by tomograms in assessing nonclassical effects displayed by quantum systems, without resorting to detailed state reconstruction procedures.

TABLE OF CONTENTS

ACKNOWLEDGMENTS	i
ABSTRACT	iii
LIST OF FIGURES	xi
ABBREVIATIONS	xii
GLOSSARY OF SYMBOLS	xiii
1 Introduction	1
2 Signatures of wave packet revivals and squeezing in optical tomograms	8
2.1 Introduction	8
2.2 Tomograms: A brief review	9
2.3 Single-mode system: A tomographic approach	11
2.3.1 Revivals and fractional revivals	11
2.3.2 Squeezing and higher-order squeezing properties	18
2.4 The double-well BEC: A tomographic approach	21
2.4.1 The model	21
2.4.2 The Revival Phenomena	23
2.4.3 Squeezing and higher-order squeezing properties of the condensate	25
2.4.4 Subsystem entropies from tomograms	27
2.5 Concluding remarks	29
3 Tomographic entanglement indicators and avoided energy-level crossings	31
3.1 Introduction	31
3.2 Entanglement indicators from tomograms	32
3.3 Avoided energy-level crossings in bipartite CV models	36

3.3.1	The double-well BEC model	36
3.3.2	Atom-field interaction model	40
3.4	Avoided crossings in multipartite HQ systems	43
3.4.1	The Tavis-Cummings model	43
3.5	Concluding remarks	45
4	Assessment and comparison of entanglement indicators in continuous-variable systems	46
4.1	Introduction	46
4.2	ξ -indicators and averaging procedures	47
4.3	Entanglement indicators in generic bipartite models	48
4.3.1	Atom-field interaction model	48
4.3.2	The double-well BEC model	52
4.4	Time-series analysis of $d_1(t)$	55
4.4.1	Atom-field interaction model	56
4.4.2	The double-well BEC model	57
4.5	Tomographic signatures in a 2-photon bipartite system	59
4.6	Concluding remarks	62
5	Dynamics of entanglement indicators in hybrid quantum systems and spin systems	64
5.1	Introduction	64
5.2	Hybrid multipartite models	65
5.2.1	The double Jaynes-Cummings model	65
5.2.2	The double Tavis-Cummings model	69
5.3	The spin system	71
5.4	Concluding remarks	75
6	Conclusion	77
A	Eigenvectors of rotated quadrature operators	80
B	Normal-ordered moments from optical tomograms	82
C	Numerical computation of the time-evolved density matrix of the bipartite BEC system	84

D	Estimation of the maximal local Lyapunov exponent Λ_L	86
E	The 2-photon frequency combs	89
F	Expressions for the chronocyclic tomograms	91

LIST OF FIGURES

2.1	Tomograms of an initial CS for a cubic Hamiltonian and $\alpha = \sqrt{10}e^{i\pi/4}$ at instants (a) 0 and T_{rev} , (b) $T_{rev}/2$, (c) $T_{rev}/3$, (d) $T_{rev}/4$, (e) $T_{rev}/5$, (f) $T_{rev}/6$, (g) $T_{rev}/9$, (h) $T_{rev}/12$, and (i) $T_{rev}/15$	13
2.2	Tomogram of an initial CS at $t = \pi/\chi_2$ for $\alpha = \sqrt{10}e^{i\pi/4}$, $\chi_1 = 1$ and $\chi_2 = 10^{-7}/\sqrt{2}$	14
2.3	Tomograms of an initial CS at $t = T_{rev}/2$ for $\alpha = \sqrt{10}e^{i\pi/4}$, $\chi_1 = 1$ and (a) $\chi_2 = 2.048 \times 10^{-7}$, (b) $\chi_2 = 1.024 \times 10^{-7}$	15
2.4	Tomograms of an initial CS at $t = T_{rev}/3$ for $\alpha = \sqrt{10}e^{i\pi/4}$, $\chi_1 = 1$ and (a) $\chi_2 = 2.048 \times 10^{-7}$, (b) $\chi_2 = (4/3) \times 10^{-7}$	15
2.5	Tomograms of an initial CS at $t = T_{rev}/4$ for $\alpha = \sqrt{10}e^{i\pi/4}$, $\chi_1 = 1$ and (a) $\chi_2 = 2.048 \times 10^{-7}$, (b) $\chi_2 = 1.024 \times 10^{-7}$, and (c) $\chi_2 = 4.096 \times 10^{-7}$	15
2.6	Tomograms of an initial CS at $T_{rev}/2$ in the amplitude decay model for $\alpha = \sqrt{10}e^{i\pi/4}$, $\Gamma\tau = 1$, $\chi_1 = 1$ and (a) $\chi_2 = 2.048 \times 10^{-7}$, (b) $\chi_2 = 1.024 \times 10^{-7}$. (c) $\text{Tr}(\rho^2)$ vs. $\Gamma\tau$ for $\chi_1 = 1$ and $\chi_2 = 2.048 \times 10^{-7}$ (green), $\chi_2 = 1.024 \times 10^{-7}$ (red).	17
2.7	Tomograms of an initial CS at $T_{rev}/2$ in the phase damping model for $\alpha = \sqrt{10}e^{i\pi/4}$, $\Gamma_p\tau = 0.1$, $\chi_1 = 1$ and (a) $\chi_2 = 2.048 \times 10^{-7}$, (b) $\chi_2 = 1.024 \times 10^{-7}$	18
2.8	Hong-Mandel squeezing as a function of scaled time t/T_{rev} for initial states (a) $ \alpha\rangle$ and (b) $ \alpha, 1\rangle$ for $\alpha = 1$, corresponding to the Kerr (solid) and cubic (dashed) Hamiltonians. The horizontal line at 0.75 denotes the value below which the state is squeezed.	20
2.9	(a) D_1 for initial $ \alpha\rangle$, (b) D_2 for initial $ \alpha, 1\rangle$, and (c) $\langle(\Delta x)^4\rangle$ for initial $ \alpha, 1\rangle$ vs. ν at instant $T_{rev}/2$, corresponding to the Kerr (solid) and cubic (dashed) Hamiltonians. The horizontal line at 0 in (a) and (b) (3/4 in (c)) denotes the value below which the state is squeezed.	20
2.10	Sections of the optical tomogram for $\theta_A = \theta_B = 0$ at instants (a) $T_{rev}/4$, (b) $T_{rev}/3$, (c) $T_{rev}/2$, and (d) T_{rev} . $\alpha_a = \alpha_b = \sqrt{10}$, and initial state $ \Psi_{00}\rangle$	25
2.11	$2q$ -order moment of $\eta = (a + a^\dagger + b + b^\dagger)/2\sqrt{2}$ vs. t/T_{rev} for initial state $ \Psi_{00}\rangle$, $ \alpha_a = \alpha_b = 1$, and $q =$ (a) 1, (b) 2, (c) 3, and (d) 4. Moments calculated from the tomogram (green) and moments from unitarily evolved state (red). The horizontal line denotes the value below which q -order squeezing occurs ($1/4$, $3/16$, $15/64$, and $105/256$ for $q = 1, 2, 3, 4$ respectively).	26

2.12	$D_q(t)$ vs. t/T_{rev} for initial state $ \Psi_{00}\rangle$, $ \alpha_a = \alpha_b = 1$, and $q =$ (a) 1, (b) 2, (c) 3, and (d) 4. Squeezing parameter from the tomogram (green) and from unitarily evolved state (red). The horizontal line corresponds to $D_q(t) = 0$	27
2.13	Subsystem entropy S_0 vs. t/T_{rev} for initial states (a) $ \Psi_{00}\rangle$, (b) $ \Psi_{10}\rangle$, and (c) $ \Psi_{11}\rangle$ with $\alpha_a = \alpha_b = 1$	28
2.14	Variation of S_0 with $ \alpha_a ^2$ and $ \alpha_b ^2$ at $T_{rev}/2$ for initial states (a) $ \Psi_{00}\rangle$, (b) and (c) $ \Psi_{10}\rangle$, and (d) $ \Psi_{11}\rangle$. Figures (a), (b) and (d) correspond to subsystem A and (c) to B.	29
3.1	(a) $E(N, k)$ vs. ω_1 for $N = 4$ and $k = 0, 2, 4$ in the BEC model. (b) ξ_{SVNE} vs. ω_1 for $N = 4$, $k = 0, 1, 2$. The curves correspond to $k = 0$ (red), 1 (blue), 2 (green) and 4 (orange). $\lambda = 0.25$	37
3.2	$\theta_A = 0, \theta_B = \pi/2$ slice of the tomogram for $N = 4$ in the BEC model. Left to right, $k = 0, 1$ and 2. Top to bottom, $\omega_1 = 0, 0.1$ and 1. . . .	38
3.3	ξ_{SVNE} (red), ξ_{TEI} (blue) and ξ_{IPR} (green) vs. ω_1 , for the state $ \psi_{4,2}\rangle$ in the BEC model.	39
3.4	Correlation of ξ_{SVNE} with ξ -indicators (left), with ε -indicators for the slice $\theta_A = 0, \theta_B = \pi/2$ (centre), and with ε -indicators for the slice $\theta_A = 0, \theta_B = 0$ (right), for the eigenstates $ \psi_{4,k}\rangle$, $0 \leq k \leq 4$ in the BEC model.	39
3.5	ξ_{SVNE} vs. λ for $N = 4$, $k = 0, 1, 2$, in the BEC model. The curves correspond to $k = 0$ (red), 1 (blue) and 2 (green). $\omega_1 = 0.25$	40
3.6	(a) $E_{AF}(N, k)$ and (b) ξ_{SVNE} vs. g for $N = 4$, $k = 0, 1, 2$ in the atom-field interaction model. The curves correspond to $k = 0$ (red), 1 (blue) and 2 (green). $\omega_F = 1.5$, $\omega_A = 1$, $\gamma = 1$	41
3.7	(a) $E_{AF}(N, k)$ and (b) ξ_{SVNE} vs. g for $N = 4$, $k = 0, 1, 2$ in the atom-field interaction model, in the degenerate case $\omega_F = \omega_A = 1$. The curves correspond to $k = 0$ (red), 1 (blue) and 2 (green). $\gamma = 1$	42
3.8	Correlation of ξ_{SVNE} with ξ -indicators (left), with ε -indicators for the slice $\theta_A = 0, \theta_B = \pi/2$ (centre), and with ε -indicators for the slice $\theta_A = 0, \theta_B = 0$ (right), for the eigenstates $ \phi_{4,k}\rangle$, $0 \leq k \leq 4$ in the atom-field interaction model. $\omega_F = \omega_A = \gamma = 1$	43
3.9	Correlation of ξ_{SVNE} with ξ -indicators (left) and with ε -indicators for the slice corresponding to $\theta = \pi/2$ for the field, and the σ_x basis for each qubit (right) for different values of Λ . The figures are for the eigenstates $ \psi_{5,6,k}\rangle$, $0 \leq k \leq 2^5 - 1$ in Case (i) in the Tavis-Cummings model.	44
3.10	Correlation between ξ_{SVNE} and ξ -indicators for different values of disorder strength and eigenstates $ \zeta_{5,6,k}\rangle$ $0 \leq k \leq 2^5 - 1$. Left to right, Cases (i), (ii) and (iii) respectively in the Tavis-Cummings model.	45

4.1	Histogram of $\varepsilon_{\text{TEI}}(\theta_A, \theta_B)$ from 100 combinations of θ_A and θ_B . The shaded area marks the values of $\varepsilon_{\text{TEI}}(\theta_A, \theta_B)$ that exceed the mean value ~ 0.07 by one standard deviation.	48
4.2	$d_1(t)$ (black) and $d_2(t)$ (pink) vs. scaled time gt/π , for $\omega_F = \omega_A = \gamma = 1$ in the atom-field interaction model. (a) $g = 0.2$, initial two-mode squeezed state $ \zeta\rangle$, $\zeta = 0.1$ (b) $g = 100$, initial state $ \alpha\rangle_F \otimes 0\rangle$, $ \alpha ^2 = 1$	49
4.3	$d_2(t)$ (blue) and $\Delta(t)$ (pink) vs. scaled time gt/π , with $\omega_F = \omega_A = \gamma = 1$, $g = 100$ in the atom-field interaction model. Initial state $ \alpha\rangle_F \otimes 0\rangle$, $ \alpha ^2 = 1$	50
4.4	$d_2(t)$ (blue) and $d_3(t)$ (brown) vs. scaled time gt/π , for $\omega_F = \omega_A = \gamma = \alpha ^2 = 1$ in the atom-field interaction model. (a) and (b): Initial state $ \alpha\rangle_F \otimes 0\rangle$, $g = 100$ and 0.2 respectively. (c) and (d): Initial state $ \alpha, 5\rangle_F \otimes 0\rangle$, $g = 100$ and 0.2 respectively.	50
4.5	$d_2(t)$ (blue) and $d_3(t)$ (brown) vs. scaled time gt/π , for $\omega_F = \omega_A = \gamma = 1$, $g = 0.2$ in the atom-field interaction model. Initial two-mode squeezed state $ \zeta\rangle$, (a) $\zeta = 0.1$ and (b) $\zeta = 0.7$	51
4.6	$d_2(t)$ (blue) and $d_3(t)$ (brown) vs. scaled time gt/π , for $\omega_F = \omega_A = \gamma = 1$, $g = 0.2$ in the atom-field interaction model. Initial state $ \psi_{\text{bin}}\rangle$ with $N = 10$	51
4.7	$d_2(t)$ (blue) and $d_3(t)$ (brown) vs. scaled time Ut/π , for $\omega_0 = U = \alpha ^2 = 1$ in the BEC model. (a) $\omega_1 = \lambda = 1$, initial state $ \alpha\rangle \otimes \alpha\rangle$; (b) $\omega_1 = \lambda = 0.1$, initial state $ \alpha\rangle \otimes \alpha\rangle$; (c) $\omega_1 = \lambda = 1$, initial state $ \alpha, 1\rangle \otimes \alpha\rangle$	53
4.8	$d_2(t)$ (blue) and $d_3(t)$ (brown) vs. scaled time Ut/π , for $\omega_0 = U = \omega_1 = \lambda = 1$ in the BEC model. (a) and (b): Initial state $ \zeta\rangle$, $\zeta = 0.1$ and 0.7 respectively. (c) Initial state $ \psi_{\text{bin}}\rangle$, $N = 10$	53
4.9	ξ'_{TEI} (black), $\xi_{\text{SVNE}}^{(A)}$ (blue) and ξ_{QMI} (red) vs. $\Gamma\tau/\pi$ for amplitude decay with $\Gamma = 0.001$ in the BEC model.	54
4.10	ξ'_{TEI} (black), $\xi_{\text{SVNE}}^{(A)}$ (blue) and ξ_{QMI} (red) vs. $\Gamma_p\tau/\pi$ for phase damping with $\Gamma_p = 0.001$ in the BEC model.	55
4.11	Λ_L obtained from the time series of $d_1(t)$ (blue) and the fit $\Lambda_\infty + (m/L^q)$ (red) vs. L , for $\omega_F = \omega_A = \gamma = 1$ in the atom-field interaction model. Initial state $ \alpha\rangle_F \otimes 0\rangle$: (a) $g = 100$, $ \alpha ^2 = 1$ (b) $g = 100$, $ \alpha ^2 = 5$ (c) $g = 0.2$, $ \alpha ^2 = 1$. (d) Initial state $ \alpha, 5\rangle_F \otimes 0\rangle$, $g = 100$, $ \alpha ^2 = 1$	56
4.12	Logarithm of $PS(f)$ vs. f/g (red) in the atom-field interaction model, corresponding to the initial states and parameter values in Figs. 4.11 (a)–(d) respectively.	57
4.13	Λ_L obtained from the time series of $d_1(t)$ (blue) and the fit $\Lambda_\infty + (m/L^q)$ (red) vs. L , for $\omega_0 = \omega_1 = \alpha = 1$ in the BEC model. Initial state $ \alpha, 1\rangle \otimes \alpha\rangle$ and (a) hopping frequency $\lambda = 5$, $U = 0.5$ (b) $\lambda = U = 1$. (c) Initial state $ \alpha, 5\rangle \otimes \alpha, 5\rangle$, $\lambda = U = 1$	58

4.14	Logarithm of $PS(f)$ vs. f/U (red) in the BEC model, corresponding to the initial states and parameter values in Figs. 4.13 (a)–(c) respectively.	58
4.15	Tomographic time-time slice (a) $w^\alpha(t_s; t_1)$ and (b) $w^\beta(t_s; t_1)$ vs. t_s and t_1 in seconds. (c) Difference $ w^\alpha(t_s; t_1) - w^\beta(t_s; t_1) $ vs. t_s and t_1 in seconds.	61
5.1	ξ_{TEI} (black), ξ'_{TEI} (blue) and $0.1 \xi_{\text{QMI}}$ (red) vs. scaled time $g_0 t$ for the field subsystem in the DJC model. Initial state (a) $ 0; 0; \phi_+\rangle$; (b), (c) $ 0; 0; \psi_+\rangle$. Detuning parameter (a),(b) 0 and (c) 1.	66
5.2	ξ_{TEI} (black), ξ'_{TEI} (blue) and $0.1 \xi_{\text{QMI}}$ (red) vs. scaled time $g_0 t$ for the atomic subsystem in the DJC model. Initial state (a) $ 0; 0; \phi_+\rangle$; (b), (c) $ 0; 0; \psi_+\rangle$. Detuning parameter (a),(b) 0 and (c) 1.	67
5.3	Equivalent circuit for the DJC model (created using IBM Q).	68
5.4	Tomograms from (a) IBM Q experiment (b) QASM simulation (c) numerical computations of the DJC model.	68
5.5	Equivalent circuit of the entangled state $ \psi_+; \psi_+\rangle$ in the DTC model (created using IBM Q).	70
5.6	ξ_{TEI} (black), ξ'_{TEI} (blue) and $0.1 \xi_{\text{QMI}}$ (red) vs. scaled time $g_0 t$ for the field subsystem in the DTC model with zero detuning. Initial field state $ 0; 0\rangle$, initial atomic state (a) $ \psi_+; \psi_+\rangle$ (b) $ \phi_+; \phi_+\rangle$ (c) $ \psi_+; \phi_+\rangle$	71
5.7	ξ_{TEI} (black), ξ'_{TEI} (blue) and $0.1 \xi_{\text{QMI}}$ (red) vs. scaled time $g_0 t$ for the bipartite atomic subsystem CD in the DTC model with zero detuning. Initial field state $ 0; 0\rangle$, initial atomic state (a) $ \psi_+; \psi_+\rangle$ (b) $ \phi_+; \phi_+\rangle$ (c) $ \psi_+; \phi_+\rangle$	71
5.8	Tomograms of spin coherent states with (ϑ, φ) equal to (a) $(0, 0)$, (b) $(\pi/4, \pi/2)$, (c) $(\pi/4, 0)$, and (d) $(2\pi/3, 4\pi/3)$. The bases are denoted by x , y and z and the outcomes by 0 and 1.	73
5.9	(a) $2(\Delta J_{\min})^2$ (b) $8(\Delta \mathcal{J}_{\min})^2$ (c) $N(\rho_{\text{AB}})$ (red), ξ_{TEI} (blue), $0.1 \xi_{\text{QMI}}$ (black) vs. scaled time $\chi_s t$. The solid curves are computed using Eq. (5.10) and the dotted curves from experimental data. The black horizontal line in (a) and (b) sets the limit below which the state is squeezed.	75
5.10	$2 N(\rho_{\text{AB}})$ (black), $2 \xi_{\text{TEI}}$ (blue), $0.2 \xi_{\text{QMI}}$ (orange), and (a) $[1 - 2(\Delta J_{\min})^2]$ (red) (b) $[1 - 8(\Delta \mathcal{J}_{\min})^2]$ (red) vs. scaled time $\chi_s t$. The solid curves are computed using Eq. (5.10) and the dotted curves from experimental data.	75

ABBREVIATIONS

CV	continuous-variable
HQ	hybrid quantum
BEC	Bose-Einstein condensate
CS	coherent state
PACS	photon-added coherent state
QED	quantum electrodynamics
IPR	inverse participation ratio
PCC	Pearson correlation coefficient
GKP	Gottesman-Kitaev-Preskill
DJC	double Jaynes-Cummings
DTC	double Tavis-Cummings
QASM	quantum assembly language
NMR	nuclear magnetic resonance

NOTATION

θ	angle (similarly, $\theta_A, \theta_B, \theta_{Ap}, \theta_{Bq}, \vartheta, \varphi, \theta', \varphi', v$)
\mathbb{X}_θ	rotated quadrature operator (similarly, $\mathbb{X}_{\theta_A}, \mathbb{X}_{\theta_B}$)
(a, a^\dagger)	ladder operators (similarly, $(b, b^\dagger), (a_A, a_A^\dagger), (a_B, a_B^\dagger)$)
(σ_+, σ_-)	spin ladder operators (additional subscripts denote subsystems labels)
$ X_\theta, \theta\rangle$	eigenstate of rotated quadrature operator (similarly, $ X_{\theta_A}, \theta_A\rangle, X_{\theta_B}, \theta_B\rangle, X\rangle$)
$ X_{\theta_A}, \theta_A; X_{\theta_B}, \theta_B\rangle$	factored product of $ X_{\theta_A}, \theta_A\rangle$ and $ X_{\theta_B}, \theta_B\rangle$
X_θ	eigenvalue of rotated quadrature operator (similarly, $X_{\theta_A}, X_{\theta_B}, X_{A0}, X_{B0}, X_{\theta_{Ap}}, X_{\theta_{Bq}}, X$)
ρ	density matrix (similarly, $\varrho, \bar{\varrho}, \bar{\rho}, \rho_{AB}, \rho_S, \rho_A, \rho_B, \rho_{m_1, m_2}, \rho_{MAB}, \rho_+, \rho_-$)
$w(X_\theta, \theta)$	single-mode tomogram
$w(X_{\theta_A}, \theta_A; X_{\theta_B}, \theta_B)$	bipartite tomogram (similarly, $w^\alpha(t_S; t_1), w^\beta(t_S; t_1)$)
$w_A(X_{\theta_A}, \theta_A)$	reduced tomogram (similarly, $w_B(X_{\theta_B}, \theta_B)$)
α	a complex number (similarly, $\zeta, \alpha_a, \alpha_b, \alpha(t), \beta(t)$)
ν	$ \alpha ^2$
$ \alpha\rangle$	coherent state of a single-mode continuous-variable system
$ \alpha\rangle_{tcs}$	truncated coherent state
$ n\rangle$	a Fock state/ an n -photon state/ an n -boson state
$ \alpha, m\rangle$	m -photon-added coherent state/ m -boson-added coherent state
$ \psi_{\text{bin}}\rangle$	binomial state
$ \zeta\rangle$	two-mode squeezed state
$ \ell, m\rangle$	factored product of number states $ \ell\rangle$ and $ m\rangle$
L_m	Laguerre polynomial of order m
H_n	Hermite polynomial of order n
T_{rev}	revival time
H	Hamiltonian of a single-mode radiation field (similarly, H')
χ_1	strength of nonlinearity (similarly, χ_2, U, γ, χ)
\mathcal{N}	photon number operator $a^\dagger a$
$F_q(\mathcal{N})$	$[Z_1, Z_2]$, a polynomial of order $q - 1$ in \mathcal{N}
$ \psi(t)\rangle$	state of the radiation field at instant t
$\text{LCM}\left(\frac{1}{\chi_1}, \frac{1}{\chi_2}\right)$	least common multiple of $(1/\chi_1)$ and $(1/\chi_2)$
Γ	rate of decoherence (similarly, Γ_p)
x	position quadrature (similarly, two-mode position quadrature η)
p	momentum quadrature
$\langle(\Delta x)^{2q}\rangle$	$2q$ -order central moment (similarly, $\langle(\Delta \eta)^{2q}\rangle, \langle(\Delta Z_1)^{2q}\rangle$)
(Z_1, Z_2)	conjugate pair in Hillery-type squeezing
D_q	squeezing parameter
H_{BEC}	Hamiltonian of the double-well BEC system (on transformation, \tilde{H}_{BEC})
N_{tot}	total number operator that commutes with the Hamiltonian (similarly, \mathcal{N}_{tot})
ω_0	frequency (similarly, $\omega_1, \lambda_1, \omega_A, \omega_F, \Omega_F, \epsilon, \omega_p, \bar{\omega}, \omega_S, \omega_1, \Omega, \Omega_0, \chi_F, \chi_0, \chi_S, \Omega_i, \Delta_i$ where $i = 1, 2, \dots, M$)
λ	hopping frequency (similarly, $g, \Lambda, \Lambda_s, g_0$)

$ \Psi_{m_1 m_2}(t)\rangle$	state of BEC system for initial $ \alpha_a, m_1\rangle \otimes \alpha_b, m_2\rangle$ at instant t
M_{m_1, m_2}	unitary operator (similarly, \mathcal{U} , V , $U(\mathbf{n})$, U_3 , S^\dagger , C' , Z_{t_s}); identity operator \mathbb{I} .
ξ_{SVNE}	subsystem von Neumann entropy (similarly, $\xi_{\text{SVNE}}^{(A)}$, $\xi_{\text{SVNE}}^{(B)}$, $\xi_{\text{SVNE}}^{(AB)}$)
ξ_{SLE}	subsystem linear entropy
ξ_{QMI}	quantum mutual information
ε_{TEI}	single-slice entanglement indicator (similarly, ε_{IPR} , ε_{BD} , ε_{PCC})
ξ_{TEI}	averaged entanglement indicator (similarly, ξ'_{TEI} , ξ_{IPR} , ξ_{BD} , ξ_{PCC})
$S(\theta_A)$	subsystem tomographic entropy (similarly, $S(\theta_B)$, S_0)
$S(\theta_A, \theta_B)$	two-mode tomographic entropy
$\eta_A(\theta_A)$	inverse participation ratio (similarly, $\eta_B(\theta_B)$, $\eta_{AB}(\theta_A, \theta_B)$)
D_{KL}	Kullback-Leibler divergence
D_B	Bhattacharyya distance
$PCC(X, Y)$	Pearson correlation coefficient between X and Y
$\text{Cov}(X, Y)$	covariance of X and Y
$(\Delta X)^2$	variance (similarly, $(\Delta Y)^2$, $(\Delta \mathbf{J} \cdot \mathbf{v}_\perp)^2$, $(\Delta J_{\min})^2$, $(\Delta \mathcal{J})^2$, $(\Delta \mathcal{J}_{\min})^2$, $(\Delta \omega)^2$, $(\Delta \Omega)^2$)
$(\sigma_x, \sigma_y, \sigma_z)$	spin operators
$ \mathbf{n}, m\rangle$	eigenstate of spin operators for \mathbf{n} chosen appropriately (for instance, $\mathbf{n} = \mathbf{e}_z$ corresponds to eigenstate of σ_z)
$w(\mathbf{n}, m)$	spin tomogram
$ \psi_{N,k}\rangle$	eigenstate of H_{BEC} ($N = 0, 1, 2 \dots$ and $k = 0, 1, \dots, N$)
$E(N, k)$	eigenvalue of H_{BEC}
H_{AF}	Hamiltonian of the atom-field interaction system
$ \phi_{N,k}\rangle$	eigenstate of H_{AF}
$E_{\text{AF}}(N, k)$	eigenvalue of H_{AF}
H_{TC}	Tavis-Cummings Hamiltonian for M two-level systems interacting with a radiation field
$ \psi_{M,N,k}\rangle$	eigenstate of H_{TC}
$d_1(t)$	difference between entanglement indicators at instant t (similarly, $d_2(t)$, $d_3(t)$, $\Delta(t)$)
τ_d	time delay
d_{emb}	embedding dimension
$I(T)$	mutual information
$C(r)$	correlation integral
DF	Jacobian obtained from time-series (similarly, product of Jacobians DF ^{L})
M _{os}	Oseledec matrix
Λ_L	maximum local Lyapunov exponent over L time steps
Λ_∞	maximum Lyapunov exponent
$PS(f)$	power spectrum as a function of frequency f
$ \Psi_\alpha\rangle$	frequency combs (similarly, $ \Psi_\beta\rangle$, $ \psi'\rangle$, $ \tilde{+}\rangle_{\omega_s}$, $ \tilde{-}\rangle_{\omega_s}$, $ \tilde{+}\rangle_{\omega_1}$, $ \tilde{-}\rangle_{\omega_1}$)
f_+	Gaussian function (similarly, f_-)
f_{cav}	superposition of Gaussian functions (similarly, g_{cav} , \mathcal{F} , \mathcal{G})
t	time (similarly, τ , δt , τ_p , T , t_s , t_1)
$ \psi_+\rangle$	maximally entangled state (similarly, $ \phi_+\rangle$)
H_{DJC}	double Jaynes-Cummings Hamiltonian
H_{DTC}	double Tavis-Cummings Hamiltonian
H_s	effective Hamiltonian of 3-qubit system
$(\uparrow\rangle, \downarrow\rangle)$	eigenstates of σ_z (similarly, in two-level atoms ($ e\rangle$, $ g\rangle$))
$(+\rangle, -\rangle)$	eigenstates of σ_x

\mathbf{J}	total spin operator with dyad $\mathbf{J}\mathbf{J}$
\mathbf{v}_s	vector (similarly, \mathbf{v}_\perp , \mathbf{v}_1 , \mathbf{v}_2)
\mathcal{J}	spin operator defined in terms of $\mathbf{J}\mathbf{J}$, \mathbf{v}_1 and \mathbf{v}_2
$N(\rho_{AB})$	negativity
$\rho_{AB}^{T_A}$	partial transpose with respect to subsystem A (similarly, $\rho_{AB}^{T_B}$)
μ	normalisation constants (similarly, d_{10} , d_{11} , \mathcal{N}_α , \mathcal{N}_β , \mathcal{M}_α , \mathcal{M}_β)

CHAPTER 1

Introduction

Measurement of any observable in a quantum mechanical system yields a histogram of the state of the system in the basis of that observable. Measurements of a judiciously chosen *quorum* of appropriate observables of a system that are informationally complete, yield a set of histograms called a tomogram. In the context of atoms interacting with radiation fields, both the optical tomogram and the tomogram pertaining to atomic observables would yield, in principle, information about the full system and its subsystems. Quantum state reconstruction seeks to obtain the density matrix from the tomogram. However, even in the simple case of a bipartite system comprising two 2-level atoms (two qubits), state reconstruction from relevant tomograms typically employs statistical tools that are inherently error-prone [1]. The reconstruction procedure is significantly more difficult in the case of entangled multipartite qubit states [2]. Attempts at scalable reconstruction programs for systems with a large number of qubits, and the challenges faced in this context, have been reported in the literature (see, for instance, [3, 4]). It is therefore desirable to extract information about the state *directly from the tomogram*, avoiding the reconstruction procedure. This has been demonstrated in bipartite qubit systems by estimating state fidelity with respect to a specific target state directly from the tomogram, and comparing the errors that arise with the corresponding errors in procedures involving detailed state reconstruction [5]. Further, efficient methods have been proposed to estimate entanglement entropies directly from experimental data in the context of qubit systems [6–9].

Reconstruction of the state of a radiation field from optical tomograms is more challenging. Even in the case of a single-mode radiation field, the Hilbert space is infinite-dimensional. Thus, for optical tomography, the infinite set of rotated quadrature operators [10, 11] given by

$$\mathbb{X}_\theta = \frac{1}{\sqrt{2}}(a^\dagger e^{i\theta} + ae^{-i\theta}), \quad \theta \in [0, \pi) \quad (1.1)$$

constitutes the quorum of observables that carries complete information about the state.

Here (a, a^\dagger) are the photon annihilation and creation operators satisfying the commutation relation $[a, a^\dagger] = 1$. We note that $\theta = 0$ corresponds to the x -quadrature and $\theta = \frac{1}{2}\pi$ corresponds to the conjugate p -quadrature. The eigenvalue equation for \mathbb{X}_θ is given by $\mathbb{X}_\theta |X_\theta, \theta\rangle = X_\theta |X_\theta, \theta\rangle$, and the optical tomogram [10, 12] is

$$w(X_\theta, \theta) = \langle X_\theta, \theta | \rho | X_\theta, \theta \rangle \quad (1.2)$$

where ρ is the field density matrix. It is worth noting that even in the simple case of a two-level atom interacting with a radiation field, the state of the field subsystem was experimentally reconstructed from the corresponding tomogram at various instants of temporal evolution only as recently as 2017 [13]. With an increase in the number of field modes interacting with an atomic system, the inevitable entanglement that arises during dynamical evolution makes state reconstruction a more formidable task. The problem posed by the size of the Hilbert space holds for other continuous-variable (CV) systems, such as a Bose-Einstein condensate (BEC) in a double-well potential and hybrid quantum (HQ) systems such as an atomic array interacting with many radiation fields. It would therefore be efficient to *read off* information about a state, wherever possible, directly from the tomogram. In particular, identifying signatures of nonclassical effects through simple manipulations of the relevant tomograms *alone* becomes an interesting and important exercise. Investigations carried out in this regard employ the ‘inverse procedure’ of starting with a known state, and obtaining the corresponding tomogram with the purpose of understanding how tomographic patterns carry signatures of nonclassical effects such as revivals, squeezing and entanglement. Such an exercise also helps to build a dictionary of signatures that can be captured in tomograms corresponding to known states. This would be the first step in applying the tomographic approach in experiments where the state is not known *a priori*. The programme just described is essentially the central theme of this thesis. We have identified and quantified nonclassical effects in both CV and HQ systems for known states, and applied the lessons learnt to extract information from experimental data when the state is not initially known. We now give a brief outline of the nonclassical effects examined in this thesis.

We first consider the revival phenomena. An initial wave packet $|\psi(0)\rangle$ governed by a nonlinear Hamiltonian is said to revive fully at an instant T_{rev} during its dynamical evolution if the wave packet $|\psi(T_{rev})\rangle$ differs from $|\psi(0)\rangle$ only by an overall phase.

The state revives due to very specific quantum interference between the basis states that comprise the wave packet. In certain systems, revivals occur *periodically* at integer multiples of T_{rev} . Under certain circumstances, ℓ -subpacket fractional revivals of the wave packet (where ℓ is a positive integer) can occur at specific instants between two successive revivals [14, 15]. At these instants the initial wave packet becomes ℓ superposed copies of itself, each with an amplitude less than that of the initial state. For instance, a radiation field governed by the Kerr Hamiltonian $\hbar\chi_1 a^{\dagger 2} a^2$ can exhibit periodic revivals and fractional revivals, with $T_{rev} = \pi/\chi_1$. (Here χ_1 is the third-order nonlinear susceptibility of the medium). For an initial coherent state (CS) $|\alpha\rangle$ ($\alpha \in \mathbb{C}$), expressed in the photon number basis $\{|p\rangle\}$ as

$$|\alpha\rangle = e^{-|\alpha|^2/2} \sum_{p=0}^{\infty} \frac{\alpha^p}{\sqrt{p!}} |p\rangle, \quad (1.3)$$

the time evolved state is a superposition of ℓ coherent states [16] at instants mT_{rev}/ℓ (where $m = 1, 2, \dots, \ell - 1$). The optical tomogram corresponding to an ℓ -subpacket fractional revival of the CS is an ℓ -strand pattern [17]. With the addition of higher-order nonlinearities (and hence more than one time scale) to the Hamiltonian, this simple picture gets modified. Super-revivals then occur in the system, when a delicate balance is struck between two or more time scales [18, 19]. Straightforward correlations between tomograms and fractional revivals are therefore not to be expected. Investigations on these lines gain impetus because super-revivals have been experimentally detected in systems of alkali atoms subject to an external field (see, for instance, [20]). In this thesis, we have examined tomograms of CV systems subject to Hamiltonians with more than one time scale both in the case of a single-mode field and the double-well BEC system.

We now turn to the squeezing properties of the states considered in this thesis. We have used the tomographic approach to examine quadrature, higher-order and entropic squeezing in CV systems, and spin squeezing from experimental data obtained by employing NMR techniques on a 3-qubit system. Quadrature squeezing is quantified by the numerical value of the variance of the corresponding observable. For instance, the state of the field is squeezed in x if the corresponding variance $\langle(\Delta x)^2\rangle$ is less than the variance of x in a CS $|\alpha\rangle$. Generalisation of this definition to include higher-order squeezing allows for two possibilities, namely, Hong-Mandel [21] and Hillery-type [22]

higher-order squeezing. Hong-Mandel squeezing of order q in x requires that the $(2q)^{\text{th}}$ central moment of x in the given state be less than the corresponding moment for the CS. Hillery-type squeezing of order q refers to squeezing in either $Z_1 = (a^q + a^{\dagger q})/\sqrt{2}$ or $Z_2 = (a^q - a^{\dagger q})/(\sqrt{2}i)$ ($q = 2, 3, \dots$). We note that the tomogram slice corresponding to a specific value of θ gives the probability distribution in that quadrature basis. Thus the central moments calculated from appropriate slices of the tomogram can be used to estimate quadrature and Hong-Mandel higher-order squeezing of the state. An elegant method has been proposed [23] for estimating Hillery-type higher-order squeezing in single-mode systems. In this thesis, we have extended this procedure to two-mode squeezing.

Further, the information entropy $S(\theta) = -\int_{-\infty}^{\infty} dX_{\theta} w(X_{\theta}, \theta) \ln w(X_{\theta}, \theta)$ corresponding to a given value of θ can be computed readily from the tomogram. The information entropies in conjugate quadrature bases, such as x and p ($\theta = 0$ and $\frac{1}{2}\pi$, respectively), satisfy an entropic uncertainty relation [24] $S(0) + S(\frac{1}{2}\pi) \geq (1 + \ln \pi)$. If the entropy in either quadrature is less than $\frac{1}{2}(1 + \ln \pi)$, entropic squeezing occurs in that quadrature. We have examined entropic squeezing in the double-well BEC system.

A major part of this thesis is devoted to finding an efficient entanglement indicator *directly* from relevant tomograms in CV, HQ and spin systems. Entanglement is an essential resource in quantum information processing. Interesting phenomena such as sudden death and birth of entanglement [25], and its collapse to a constant non-zero value over a significant interval of time [26] have been found in model systems. A standard measure of entanglement between the two subsystems A and B of a bipartite system is the subsystem von Neumann entropy $\xi_{\text{SVNE}} = -\text{Tr}(\rho_i \log_2 \rho_i)$ where ρ_i ($i = A, B$) is the reduced density matrix of the subsystem concerned. Computation of this measure, however, requires a knowledge of the density matrix. Qualitative signatures of entanglement in the output state of a quantum beamsplitter have been identified solely from tomograms, and reported in the literature [27]. We have carried out detailed *quantitative* analysis of entanglement, using indicators obtained directly from tomograms in a variety of multipartite systems of experimental interest. We have assessed their efficacy by comparing them with ξ_{SVNE} and other standard measures of entanglement. In particular, we have undertaken this study on two experimentally viable bipartite CV systems, namely, the double-well BEC and a multi-level atom modelled as an oscillator interacting with the radiation field. We have examined the performance of

these entanglement indicators in multipartite HQ systems of two-level atoms interacting with radiation fields.

We have also examined how the entanglement indicator can be used to distinguish between two 2-photon states produced in a recent experiment [28] using ultrashort light pulses. In this experiment, photon coincidence count measurements were used to distinguish between the two states, and further, a quantum logic operation was implemented. The relevant tomogram in this experiment is a chronocyclic tomogram [29] (i.e., where time and frequency are the relevant observables analogous to the x and p quadratures in an optical tomogram). We have demonstrated that entanglement indicators computed from the chronocyclic tomograms corresponding to these two states distinguish unambiguously between them. The purpose of this investigation was to provide an alternative method for distinguishing between two optical states.

Of particular interest and relevance is the performance of the tomographic entanglement indicators computed directly from experimental data. In this context, we have examined HQ systems using the IBM quantum computer and also the spin system mentioned earlier. In the former case, equivalent circuits that mimic the atomic subsystem of the multipartite HQ system considered, were provided to the IBM quantum computer for generation of the tomogram. The purpose of this investigation was to assess the extent to which experimental losses affected entanglement indicators. In the latter case, the NMR-QIP group in IISER Pune, India, provided us with experimentally reconstructed density matrices from an NMR spectroscopy experiment [30]. We have computed the corresponding tomograms and from these, the entanglement indicators. The purpose of this investigation was to assess, using a simple experimentally viable entangled system, the limitations that could possibly arise by neglecting the off-diagonal elements of the density matrix. A significant outcome of this thesis is the identification of *useful and reliable entanglement indicators directly from tomograms* in generic quantum systems. The thesis showcases the advantages of extracting information from the tomogram. These outweigh the limitations that this approach entails in certain contexts.

A variety of initial states of the radiation field have been considered in our investigation. This facilitates understanding of the sensitivity of the nonclassical effects to the specific initial state considered. Apart from the standard CS (Eq. (1.3)), states such as the photon-added coherent states, which exhibit quantifiable departure from coherence,

have been used. The m -photon-added coherent state $|\alpha, m\rangle$ (m -PACS) is given by [31]

$$|\alpha, m\rangle = \frac{a^{\dagger m}}{\sqrt{L_m(-|\alpha|^2)m!}} |\alpha\rangle, \quad (1.4)$$

where L_m is the Laguerre polynomial of order m . In bipartite systems comprising two field modes, we have considered both unentangled and entangled initial states. The former are factored products of combinations of coherent and photon-added coherent states. The latter are the binomial state $|\psi_{\text{bin}}\rangle$ and the two-mode squeezed state $|\zeta\rangle$. For a non-negative integer N , the binomial state $|\psi_{\text{bin}}\rangle$ is given by [32]

$$|\psi_{\text{bin}}\rangle = 2^{-N/2} \sum_{n=0}^N \binom{N}{n}^{1/2} |N-n, n\rangle, \quad (1.5)$$

where $|N-n, n\rangle \equiv |N-n\rangle \otimes |n\rangle$. The two-mode squeezed state is given by [33]

$$|\zeta\rangle = e^{\zeta^* ab - \zeta a^\dagger b^\dagger} |0, 0\rangle, \quad (1.6)$$

where $\zeta \in \mathbb{C}$, ζ^* is its complex conjugate, and $|0, 0\rangle$ is the product state corresponding to $N = 0, n = 0$.

The contents of the rest of this thesis are as follows:

In **Chapter 2**, we summarise the salient features of the tomograms corresponding to single-mode radiation fields and bipartite CV systems that are relevant for our purpose. This is followed by an illustration of how full, fractional and super-revivals are identified from tomograms corresponding to the state of a single-mode radiation field governed by a Hamiltonian with more than one time scale, at appropriate instants of temporal evolution. We comment on the decoherence properties of states at the instant $\frac{1}{2}T_{\text{rev}}$. We have investigated the (quadrature and higher-order) squeezing properties of states of the radiation field directly from their tomograms. We have extended our investigations on the revival and squeezing phenomena to the double-well BEC system. The results have been published in Ref. [34].

In **Chapter 3**, we propose several entanglement indicators that can be obtained directly from tomograms. We compare the performance of these indicators and assess them quantitatively in bipartite CV systems (the double-well BEC, and the radiation field interacting with a multi-level atom modelled as an oscillator) and in a multipartite

HQ system (two-level atoms interacting with a radiation field). The contents of this chapter are based on Ref. [35].

In **Chapter 4**, we assess the performance of the tomographic entanglement indicators in comparison with standard measures of entanglement during temporal evolution in CV systems, using tools of nonlinear time-series analysis. These results have been published in Ref. [36]. We also give details pertaining to the manner in which we have used tomograms to distinguish between the two optical states reported in the experiment [28] mentioned earlier.

In **Chapter 5**, we have examined entanglement indicators in the context of the double Jaynes-Cummings and the double Tavis-Cummings models. The IBM quantum computing platform has been used to simulate and execute equivalent circuits of these HQ models. Quantitative comparison of the extent of entanglement obtained from experimental runs, simulation, and direct calculation from the HQ models, has been carried out. These results have been published in Ref. [37]. We have also assessed the performance of the entanglement indicator in the spin system studied in [30].

Finally in **Chapter 6**, the results of the thesis are summarised, emphasising the novel aspects, and indicating avenues for future research. Appendices A to F augment the material presented in the main text.

CHAPTER 2

Signatures of wave packet revivals and squeezing in optical tomograms

2.1 Introduction

In this chapter, we examine the revival phenomena and the squeezing properties of quantum wave packets corresponding to both single-mode and bipartite systems. Our investigations are carried out by examining tomograms obtained at specific instants during temporal evolution of the system of interest. The effect of decoherence on the system state is also examined. Full, fractional and super-revivals are investigated in the case of a single-mode radiation field propagating through a nonlinear medium. Quantitative estimates of quadrature and higher-order squeezing of the field state have been obtained using procedures to compute the central moments and expectation values of appropriate observables *directly* from tomograms. The bipartite continuous-variable system that we have examined is a Bose-Einstein condensate (BEC) trapped in a double-well with nonlinear interactions. We identify and assess the manner in which the revival phenomena and two-mode amplitude squeezing properties manifest in this case, choosing initial states which are factored products of the subsystem states. We have determined the extent of entropic squeezing of the condensate in one of the wells from the corresponding tomogram.

To facilitate the discussion, we first review relevant properties of tomograms of single-mode and bipartite systems in Section 2.2. In Section 2.3, we consider single-mode systems governed by Hamiltonians with one or more time scales, and we identify full, fractional and super-revivals from tomograms. The manner in which a specific state of the system decoheres under amplitude and phase damping is studied. The quadrature and higher-order squeezing properties of the single-mode system are assessed tomographically. In Section 2.4, we carry out our investigations on the revival, quadrature and entropic squeezing phenomena in the double-well BEC system for initial states that

are unentangled coherent states or boson-added coherent states. We conclude with brief remarks.

2.2 Tomograms: A brief review

We recall from Chapter 1 that a tomogram is obtained by measuring a quorum of observables which, in principle, gives complete information about the state of the system. In the case of a single-mode radiation field the tomogram (Eq. (1.2)) is given by

$$w(X_\theta, \theta) = \langle X_\theta, \theta | \rho | X_\theta, \theta \rangle.$$

Here ρ is the density matrix, and $\mathbb{X}_\theta |X_\theta, \theta\rangle = X_\theta |X_\theta, \theta\rangle$. It is evident that for a pure state $|\psi\rangle$, $w(X_\theta, \theta) = |\langle X_\theta, \theta | \psi \rangle|^2$. We see that the tomogram is a collection of probability distributions corresponding to the rotated quadrature operators $\mathbb{X}_\theta = (ae^{-i\theta} + a^\dagger e^{i\theta})/\sqrt{2}$. For each θ ,

$$\int_{-\infty}^{\infty} dX_\theta w(X_\theta, \theta) = 1. \quad (2.1)$$

The tomogram $w(X_\theta, \theta)$ is plotted with X_θ on the x -axis and θ on the y -axis.

We can show that

$$\mathbb{X}_\theta = e^{i\theta a^\dagger a} \frac{(a + a^\dagger)}{\sqrt{2}} e^{-i\theta a^\dagger a}, \quad (2.2)$$

using the Baker-Campbell-Hausdorff identity for any operator \mathcal{O} , given by

$$e^{i\mathcal{Q}} \mathcal{O} e^{-i\mathcal{Q}} = \mathcal{O} + i[\mathcal{Q}, \mathcal{O}] + \frac{i^2}{2!}[\mathcal{Q}, [\mathcal{Q}, \mathcal{O}]] + \frac{i^3}{3!}[\mathcal{Q}, [\mathcal{Q}, [\mathcal{Q}, \mathcal{O}]]] + \dots, \quad (2.3)$$

where \mathcal{Q} is a Hermitian operator. Substituting $\mathcal{O} = (a + a^\dagger)/\sqrt{2}$ and $\mathcal{Q} = \theta a^\dagger a$ in Eq. (2.3), we get Eq. (2.2).

From Eq. (2.2) and $\mathbb{X}_\theta |X_\theta, \theta\rangle = X_\theta |X_\theta, \theta\rangle$, we get

$$|X_\theta, \theta\rangle = e^{i\theta a^\dagger a} |X\rangle, \quad (2.4)$$

where $|X\rangle$ is the eigenstate of the operator $((a + a^\dagger)/\sqrt{2})$. We note that $e^{i\pi a^\dagger a}$ is the parity operator since $\mathbb{X}_{\theta+\pi} = e^{i\pi a^\dagger a} \mathbb{X}_\theta e^{-i\pi a^\dagger a} = -\mathbb{X}_\theta$, which in turn implies that

$e^{i\pi a^\dagger a} |X_\theta, \theta\rangle = |-X_\theta, \theta\rangle$. Using this and Eq. (2.4), we get

$$w(X_{\theta+\pi}, \theta + \pi) = w(-X_\theta, \theta). \quad (2.5)$$

For state reconstruction, although it is sufficient to work with the range $0 \leq \theta < \pi$, the tomogram plotted for $0 \leq \theta < 2\pi$ helps visualise various features better.

The tomogram of a normalised pure state $|\psi\rangle$, which can be expanded in the photon number basis $\{|p\rangle\}$ as $\sum_{p=0}^{\infty} c_p |p\rangle$, is given by [38]

$$w(X_\theta, \theta) = \frac{e^{-X_\theta^2}}{\sqrt{\pi}} \left| \sum_{n=0}^{\infty} \frac{c_n e^{-in\theta}}{\sqrt{n!} 2^{\frac{n}{2}}} H_n(X_\theta) \right|^2, \quad (2.6)$$

where $H_n(X_\theta)$ is the Hermite polynomial. In this expression (derived in Appendix A), c_n alone is a function of time. Hence Eq. (2.6) is useful for numerical computation of tomograms at various instants of time.

These ideas can be extended in a straightforward manner to multimode systems. In particular, for a bipartite system we define rotated quadrature operators,

$$\mathbb{X}_{\theta_A} = (a^\dagger e^{i\theta_A} + a e^{-i\theta_A})/\sqrt{2}, \quad \text{and} \quad \mathbb{X}_{\theta_B} = (b^\dagger e^{i\theta_B} + b e^{-i\theta_B})/\sqrt{2}.$$

Here (a, a^\dagger) and (b, b^\dagger) are the particle annihilation and creation operators corresponding to subsystems A and B respectively, of the bipartite system. The bipartite tomogram

$$w(X_{\theta_A}, \theta_A; X_{\theta_B}, \theta_B) = \langle X_{\theta_A}, \theta_A; X_{\theta_B}, \theta_B | \rho_{AB} | X_{\theta_A}, \theta_A; X_{\theta_B}, \theta_B \rangle, \quad (2.7)$$

where ρ_{AB} is the bipartite density matrix and $\mathbb{X}_{\theta_i} |X_{\theta_i}, \theta_i\rangle = X_{\theta_i} |X_{\theta_i}, \theta_i\rangle$ ($i = A, B$). Here, and in the rest of the thesis, $|X_{\theta_A}, \theta_A\rangle \otimes |X_{\theta_B}, \theta_B\rangle$ is denoted by $|X_{\theta_A}, \theta_A; X_{\theta_B}, \theta_B\rangle$. The normalisation condition is given by

$$\int_{-\infty}^{\infty} dX_{\theta_A} \int_{-\infty}^{\infty} dX_{\theta_B} w(X_{\theta_A}, \theta_A; X_{\theta_B}, \theta_B) = 1 \quad (2.8)$$

for each θ_A and θ_B .

Analogous to the single-mode example, we now consider a pure state $|\psi\rangle$ expanded in the Fock bases $\{|m\rangle\}$, $\{|n\rangle\}$ corresponding to subsystems A and B respectively as

$|\psi\rangle = \sum_{m,n=0}^{\infty} c_{mn} |m, n\rangle$. Here, $|m, n\rangle$ is a short-hand notation for $|m\rangle \otimes |n\rangle$ and c_{mn} are the expansion coefficients.

It is straightforward to extend the procedure (Appendix A) used in deriving Eq. (2.6) to generic bipartite systems whose subsystems are infinite-dimensional. We then get

$$w(X_{\theta_A}, \theta_A; X_{\theta_B}, \theta_B) = \frac{\exp(-X_{\theta_A}^2 - X_{\theta_B}^2)}{\pi} \times \left| \sum_{m,n=0}^{\infty} \frac{c_{mn} e^{-i(m\theta_A + n\theta_B)}}{(m!n!2^{m+n})^{1/2}} H_m(X_{\theta_A}) H_n(X_{\theta_B}) \right|^2. \quad (2.9)$$

The tomograms corresponding to the subsystems A and B (reduced tomograms) are respectively given by

$$w_A(X_{\theta_A}, \theta_A) = \langle X_{\theta_A}, \theta_A | \rho_A | X_{\theta_A}, \theta_A \rangle = \int_{-\infty}^{\infty} w(X_{\theta_A}, \theta_A; X_{\theta_B}, \theta_B) dX_{\theta_B}, \quad (2.10)$$

for any fixed value of θ_B and

$$w_B(X_{\theta_B}, \theta_B) = \langle X_{\theta_B}, \theta_B | \rho_B | X_{\theta_B}, \theta_B \rangle = \int_{-\infty}^{\infty} w(X_{\theta_A}, \theta_A; X_{\theta_B}, \theta_B) dX_{\theta_A} \quad (2.11)$$

for any fixed value of θ_A . The reduced density matrix ρ_A (respectively, ρ_B) is given by $\text{Tr}_B(\rho_{AB})$ (resp., $\text{Tr}_A(\rho_{AB})$).

2.3 Single-mode system: A tomographic approach

2.3.1 Revivals and fractional revivals

As stated in Chapter 1, when an initial quantum wave packet $|\psi(0)\rangle$ evolves under a nonlinear Hamiltonian, it could revive at a later instant of time T_{rev} under certain circumstances. The fidelity $|\langle\psi(0)|\psi(T_{rev})\rangle|^2 = 1$. When an initial coherent state of light $|\alpha\rangle$ ($\alpha \in \mathbb{C}$) propagates through a nonlinear optical medium, a simple choice for the effective Hamiltonian is $\hbar\chi_1 a^{\dagger 2} a^2$ (Kerr Hamiltonian) where (a, a^\dagger) are photon destruction and creation operators respectively. In this example, the state of the radiation field exhibits both periodic revivals and fractional revivals. Here $T_{rev} = \pi/\chi_1$ and an

ℓ -subpacket fractional revival occurs at T_{rev}/ℓ ($\ell = 2, 3, \dots$).

In this system, it has been shown earlier [17], that the optical tomogram at instants of revivals and fractional revivals is composed of distinct strands in contrast to blurred patterns at other generic instants during temporal evolution of the field. By using the method of ‘strand-counting’, the authors infer that corresponding to an ℓ -subpacket fractional revival the field tomogram has ℓ strands. Thus for instance, at $T_{rev}/3$, the tomogram is comprised of only 3 distinct strands. A limitation in this method is that individual strands in the tomogram corresponding to an ℓ -subpacket fractional revival will not be distinct for ℓ sufficiently large (5 or more for $|\alpha| \sim 3$) due to quantum interference effects. However, to understand the broad features of the revival phenomena it suffices to employ this procedure without resorting to detailed quantitative methods.

We now proceed to apply this tomographic approach to a system whose dynamics is governed by the Hamiltonian $H = (\hbar\chi_1 a^{\dagger 2} a^2 + \hbar\chi_2 a^{\dagger 3} a^3)$. In what follows we set $\hbar = 1$ for convenience. To facilitate the discussion, we first consider an initial CS evolving in an effective cubic Hamiltonian $H' = \chi_2 a^{\dagger 3} a^3 = \chi_2 \mathcal{N}(\mathcal{N} - 1)(\mathcal{N} - 2)$, where $\mathcal{N} = a^{\dagger} a$ and χ_2 is a constant with appropriate dimensions. We will then move on to consider the effects of the full Hamiltonian H using the tomographic approach. We corroborate our numerical findings with analytical explanations wherever possible for the revival patterns that we observe.

It can be easily seen that an initial CS or 1-PACS governed by H' revives fully at instants $T_{rev} = \pi/\chi_2$. Of immediate interest to us is the nature of tomograms at instants T_{rev}/ℓ where ℓ is a positive integer. The optical tomograms for different values of ℓ are shown in Figs. 2.1 (a)-(i). The following observations are in order. (i) At initial time (equivalently at instant T_{rev}) and at $T_{rev}/3$, the tomograms look similar. This is in sharp contrast to the case of the system governed by the Kerr Hamiltonian mentioned earlier. While the system at hand is more complicated, the full revival at $T_{rev}/3$ is a simple consequence of the fact that $n(n-1)(n-2)/3$ is even $\forall n \in \mathbb{N}$. Here, $\mathcal{N}|n\rangle = n|n\rangle$, with $\{|n\rangle\}$ denoting the photon number basis. Hence corresponding to an initial state $|\psi(0)\rangle = \sum_{n=0}^{\infty} c_n |n\rangle$, the state at instant $T_{rev}/3$ is

$$|\psi(T_{rev}/3)\rangle = \mathcal{U}(T_{rev}/3) |\psi(0)\rangle = \sum_{n=0}^{\infty} e^{-i\pi n(n-1)(n-2)/3} c_n |n\rangle = |\psi(0)\rangle.$$

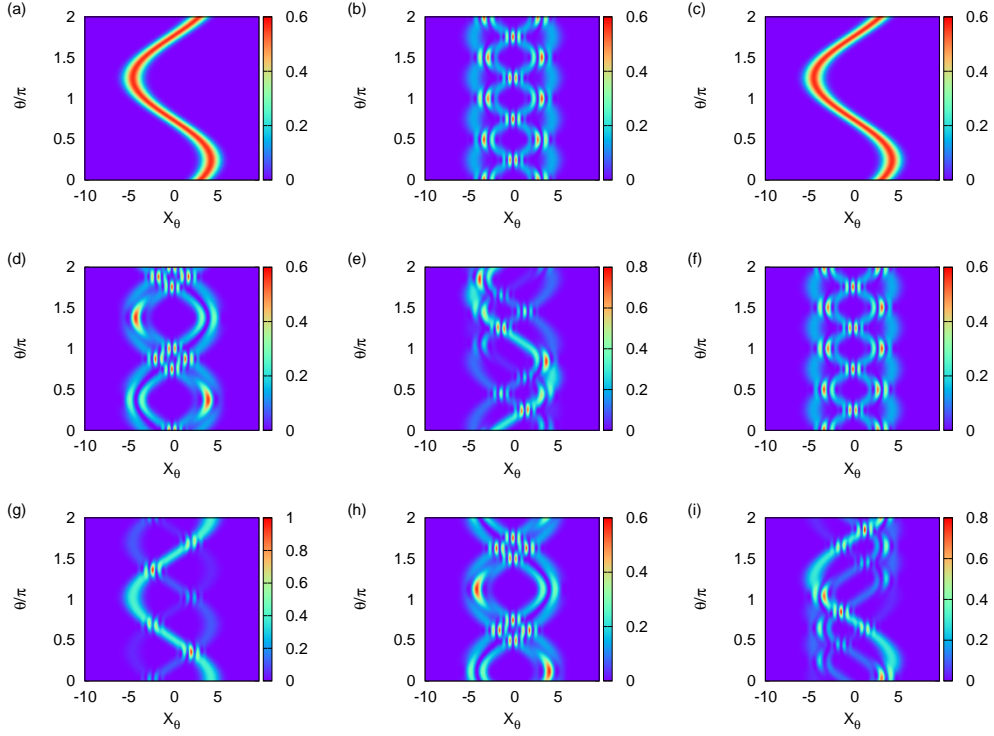


Figure 2.1: Tomograms of an initial CS for a cubic Hamiltonian and $\alpha = \sqrt{10}e^{i\pi/4}$ at instants (a) 0 and T_{rev} , (b) $T_{rev}/2$, (c) $T_{rev}/3$, (d) $T_{rev}/4$, (e) $T_{rev}/5$, (f) $T_{rev}/6$, (g) $T_{rev}/9$, (h) $T_{rev}/12$, and (i) $T_{rev}/15$.

(ii) At instants $T_{rev}/2$ and $T_{rev}/6$, the tomograms are similar and have four strands each, in contrast to what is reported in [17], where at $T_{rev}/2$ the tomogram has two strands and at $T_{rev}/6$ it has six strands.

The new features in our system obviously follow from the properties of the unitary time evolution operator corresponding to H' . An analysis of the properties of the time evolution operator would, in principle, explain the appearance of a specific number of strands in the tomogram at different instants T_{rev}/ℓ .

We are now in a position to investigate tomogram patterns for the full Hamiltonian

$$H = (\chi_1 a^{\dagger 2} a^2 + \chi_2 a^{\dagger 3} a^3). \quad (2.12)$$

In this case,

$$T_{rev} = \pi \text{LCM} \left(\frac{1}{\chi_1}, \frac{1}{\chi_2} \right). \quad (2.13)$$

It is easy to see that if the ratio χ_1/χ_2 is irrational, revivals are absent and the generic tomogram at any instant is blurred. This is illustrated in Fig. 2.2 for an initial CS with $\alpha = \sqrt{10} \exp(i\pi/4)$ with $\chi_1 = 1$, and $\chi_2 = 10^{-7}/\sqrt{2}$ at $t = \pi/\chi_2$.

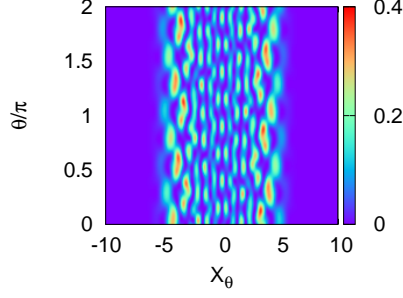


Figure 2.2: Tomogram of an initial CS at $t = \pi/\chi_2$ for $\alpha = \sqrt{10}e^{i\pi/4}$, $\chi_1 = 1$ and $\chi_2 = 10^{-7}/\sqrt{2}$.

For rational χ_1/χ_2 , revivals and fractional revivals are seen. Fractional revivals occur at instants T_{rev}/ℓ as before, but the corresponding tomogram patterns are sensitive to the ratio χ_1/χ_2 . We expect that for a given ℓ , the tomogram will have ℓ strands as a consequence of the Kerr term in H . The cubic term in H however allows for other possibilities. We illustrate this for an initial CS with Hamiltonian H and $\alpha = \sqrt{10}\exp(i\pi/4)$ in Figs. 2.3 – 2.5. At the instant $T_{rev}/2$, apart from the two-strand tomogram for $\chi_1 = 1$ and $\chi_2 = 2.048 \times 10^{-7}$, one of the other possibilities is a four-strand tomogram for $\chi_1 = 1$ and $\chi_2 = 1.024 \times 10^{-7}$ (Figs. 2.3 (a),(b)). Similarly at $t = T_{rev}/3$, the tomogram has three strands for $\chi_1 = 1$ and $\chi_2 = 2.048 \times 10^{-7}$ and a single strand similar to the tomogram of a CS for $\chi_1 = 1$ and $\chi_2 = (4/3) \times 10^{-7}$ (Figs. 2.4 (a),(b)). At $t = T_{rev}/4$ three specimen tomograms which are distinctly different from each other are shown in Figs. 2.5 (a)-(c) with $\chi_1 = 1$ and $\chi_2 = 2.048 \times 10^{-7}$, 1.024×10^{-7} and 4.096×10^{-7} respectively.

These features can be explained on a case by case basis as before, by examining the periodicity properties of the unitary time evolution operator at appropriate instants. It is however evident that the simple inference that an ℓ -subpacket fractional revival is associated with an ℓ -strand tomogram alone, does not hold when more than one time scale is involved in the Hamiltonian, and there can be several tomograms possible at a given instant depending on the interplay between the different time scales in the system.

Thus distinct signatures of higher-order nonlinearities are captured in tomograms corresponding to specific instants of fractional revivals. This observation could be of considerable use in understanding the role of higher-order susceptibilities through experiments. Practical difficulties arise because the susceptibility parameter is numerically small for the Kerr medium. (In our discussions we have scaled χ_1 to unity).

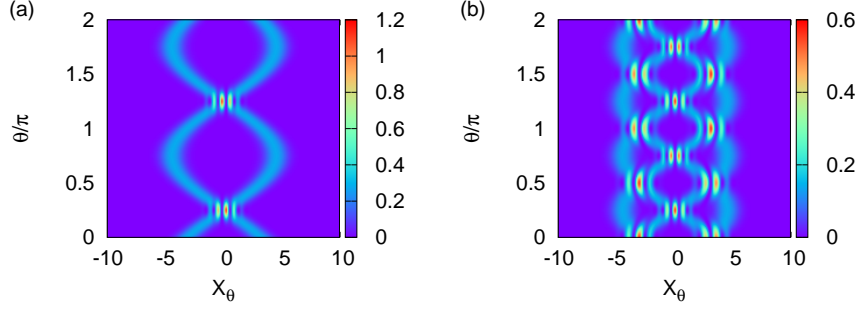


Figure 2.3: Tomograms of an initial CS at $t = T_{rev}/2$ for $\alpha = \sqrt{10}e^{i\pi/4}$, $\chi_1 = 1$ and (a) $\chi_2 = 2.048 \times 10^{-7}$, (b) $\chi_2 = 1.024 \times 10^{-7}$.

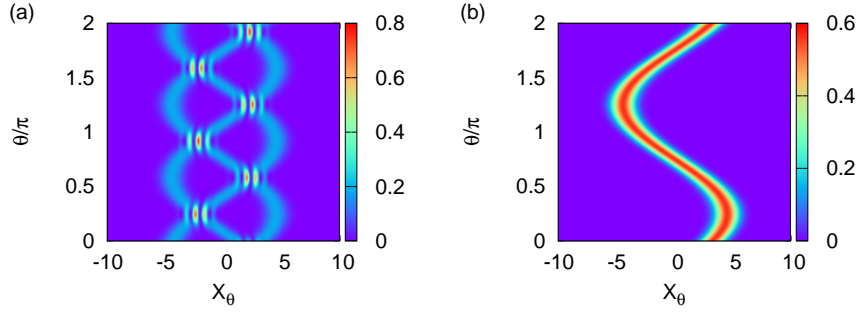


Figure 2.4: Tomograms of an initial CS at $t = T_{rev}/3$ for $\alpha = \sqrt{10}e^{i\pi/4}$, $\chi_1 = 1$ and (a) $\chi_2 = 2.048 \times 10^{-7}$, (b) $\chi_2 = (4/3) \times 10^{-7}$.

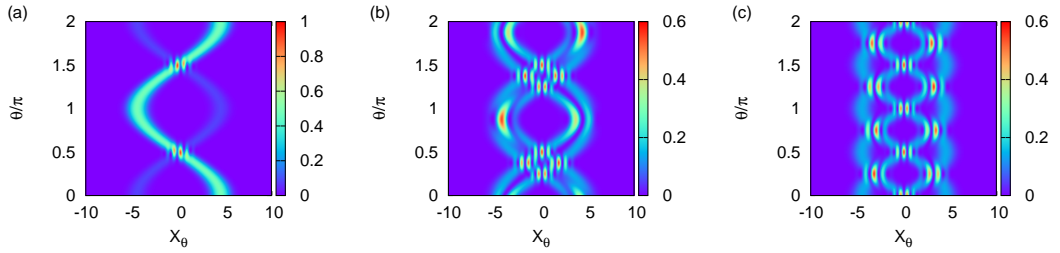


Figure 2.5: Tomograms of an initial CS at $t = T_{rev}/4$ for $\alpha = \sqrt{10}e^{i\pi/4}$, $\chi_1 = 1$ and (a) $\chi_2 = 2.048 \times 10^{-7}$, (b) $\chi_2 = 1.024 \times 10^{-7}$, and (c) $\chi_2 = 4.096 \times 10^{-7}$.

Typically, the loss rate of the field is such that damping occurs much faster than T_{rev} . It is therefore considerably difficult to sustain field collapses and revivals till T_{rev} in experiments. However a forerunner to such studies [39] has been successfully carried out by engineering an artificial Kerr medium with sufficiently high susceptibility in which collapses and revivals of a coherent state have been observed. Since then, several experiments (see, for instance, [40, 41]) have been performed in circuit QED to implement Kerr-type nonlinearities in single-mode and bipartite systems. The coherence time of the microwave cavity in circuit QED has also significantly increased to orders of milliseconds [42]. While effects of higher-order nonlinearities are more subtle as we have shown, it should still be possible in future to capture the tomographic signatures reported above, particularly because they can be seen even at the instant $T_{rev}/4$.

We now examine the role played by interaction of the single-mode system with an external environment, and the manner in which the purity of the system gets affected. For illustrative purposes, we consider the state at the instant $T_{rev}/2$ corresponding to an initial CS governed by the Hamiltonian (2.12). This is allowed to interact with the environment. The procedure used is similar to that employed for the Kerr Hamiltonian [17] so as to facilitate comparison of the two cases.

We consider two models of decoherence, namely, amplitude decay and phase damping of the state. First, dissipation is modelled using the master equation for amplitude decay

$$\frac{d\rho}{d\tau} = -\Gamma(a^\dagger a \rho - 2a \rho a^\dagger + \rho a^\dagger a). \quad (2.14)$$

Here ρ denotes the density matrix, Γ is the rate of loss of photons and τ the time parameter is reckoned from the instant $T_{rev}/2$.

The solution to this master equation is [43]

$$\rho(\tau) = \sum_{n,n'=0}^{\infty} \rho_{n,n'}(\tau) |n\rangle \langle n'|, \quad (2.15)$$

with matrix elements

$$\begin{aligned} \rho_{n,n'}(\tau) = e^{-\Gamma\tau(n+n')} \sum_{r=0}^{\infty} \sqrt{\binom{n+r}{r} \binom{n'+r}{r}} \\ (1 - e^{-2\Gamma\tau})^r \rho_{n+r,n'+r}(\tau=0). \end{aligned} \quad (2.16)$$

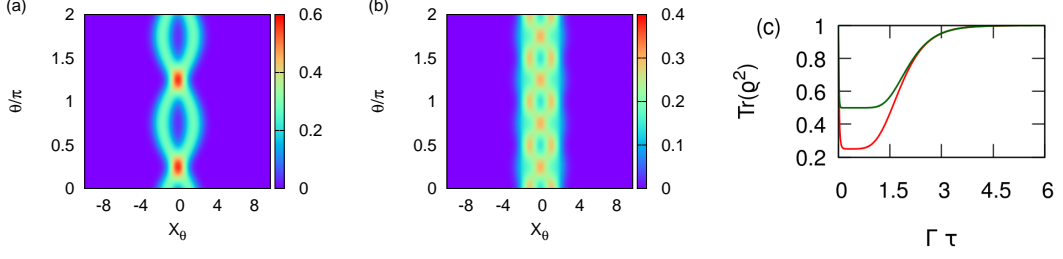


Figure 2.6: Tomograms of an initial CS at $T_{rev}/2$ in the amplitude decay model for $\alpha = \sqrt{10}e^{i\pi/4}$, $\Gamma\tau = 1$, $\chi_1 = 1$ and (a) $\chi_2 = 2.048 \times 10^{-7}$, (b) $\chi_2 = 1.024 \times 10^{-7}$. (c) $\text{Tr}(\rho^2)$ vs. $\Gamma\tau$ for $\chi_1 = 1$ and $\chi_2 = 2.048 \times 10^{-7}$ (green), $\chi_2 = 1.024 \times 10^{-7}$ (red).

As is to be expected from Eqs. (2.15) and (2.16) as $\Gamma\tau \rightarrow \infty$ the state evolves to $|0\rangle\langle 0|$. The purity of the state ($\text{Tr}(\rho^2)$) initially decreases from 1 corresponding to the initial pure state, and subsequently increases back to 1 when $\Gamma\tau \approx 4.5$ (Fig. 2.6 (c)). Depending on the ratio χ_1/χ_2 we see different extents of loss of purity of the state. The red (green) curve corresponds to $\chi_1 = 1$ and $\chi_2 = 1.024 \times 10^{-7}$ ($\chi_2 = 2.048 \times 10^{-7}$). Further, new aspects of decoherence in the system considered by us arise as a consequence of the possibility of more than one distinctly different tomograms at $T_{rev}/2$, depending on the ratio χ_1/χ_2 (Figs. 2.6 (a),(b)).

Dissipation through phase damping is modelled using the master equation [43],

$$\frac{d\bar{\rho}}{d\tau} = -\Gamma_p(\mathcal{N}^2\bar{\rho} - 2\mathcal{N}\bar{\rho}\mathcal{N} + \bar{\rho}\mathcal{N}^2), \quad (2.17)$$

where $\bar{\rho}$ is the density matrix in the phase damping model and Γ_p is the rate of decoherence. The solution to this master equation also can be expressed in the form given in Eq. (2.15), with matrix elements [43]

$$\bar{\rho}_{n,n'}(\tau) = e^{-\Gamma_p\tau(n-n')^2}\bar{\rho}_{n,n'}(\tau=0). \quad (2.18)$$

As $\Gamma_p\tau \rightarrow \infty$, it is evident that the off-diagonal terms of the density matrix vanish while the diagonal terms of $\bar{\rho}_{n,n'}(\tau=0)$ remain unchanged due to phase damping. In contrast to amplitude damping, the state does not go back to a pure state as $\Gamma_p\tau \rightarrow \infty$ but remains a mixed state. Further, the differences between tomograms with different strand structures (consequent to different ratios of χ_1/χ_2) disappear faster than in the case of amplitude damping. Figures 2.7 (a) and (b) show the effect of phase damping at $\Gamma_p\tau = 0.1$ for two such ratios. However, for $\Gamma_p\tau = 1$ the differences are barely visible.

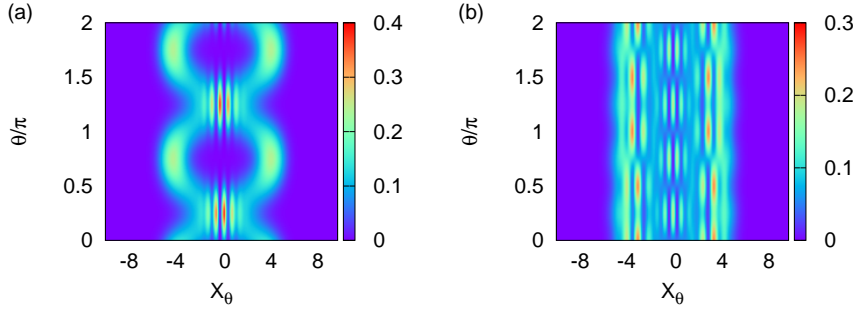


Figure 2.7: Tomograms of an initial CS at $T_{rev}/2$ in the phase damping model for $\alpha = \sqrt{10}e^{i\pi/4}$, $\Gamma_p\tau = 0.1$, $\chi_1 = 1$ and (a) $\chi_2 = 2.048 \times 10^{-7}$, (b) $\chi_2 = 1.024 \times 10^{-7}$.

2.3.2 Squeezing and higher-order squeezing properties

We now proceed to examine the squeezing and higher-order squeezing properties of the state of the system with Hamiltonian H . Once again, our aim is to identify and assess these nonclassical effects directly from the tomogram without attempting to reconstruct the state at any instant of time. As mentioned in Chapter 1, we will quantify the extent of quadrature, Hong-Mandel and Hillery-type higher-order squeezing. The extent of Hong-Mandel squeezing is obtained by calculating the central moments of the probability distribution corresponding to the appropriate quadrature. Thus for instance, to quantify the extent of second-order Hong-Mandel squeezing in the x -quadrature, we calculate the fourth central moment of a horizontal cut of the tomogram at $\theta = 0$. (For $q = 1$, Hong-Mandel squeezing is identical to quadrature squeezing).

We recall that Hillery-type squeezing of order q corresponds to squeezing in either $Z_1 = (a^q + a^{\dagger q})/\sqrt{2}$ or $Z_2 = (a^q - a^{\dagger q})/(\sqrt{2}i)$ ($q = 2, 3, \dots$). A useful quantifier D_q of q th-power squeezing in Z_1 for instance, is defined [22] in terms of the commutator $[Z_1, Z_2] = F_q(\mathcal{N})$ as

$$D_q = \frac{2\langle(\Delta Z_1)^2\rangle - |\langle F_q(\mathcal{N})\rangle|}{|\langle F_q(\mathcal{N})\rangle|}. \quad (2.19)$$

where $\langle(\Delta Z_1)^2\rangle$ is the variance in Z_1 . A similar definition holds for q th-power squeezing in Z_2 . We note that $F_q(\mathcal{N})$ is a polynomial function of order $(q-1)$ in \mathcal{N} . A state is q th-power squeezed if $-1 \leq D_q < 0$. It is clear that Z_1 and Z_2 cannot be obtained in a straightforward manner from the tomogram as they involve terms with products of powers of different rotated quadrature operators and hence cannot be assigned probability distributions directly from a set of tomograms.

However an illustrative treatment [23] of the problem of expressing the expectation value of a product of moments of creation and destruction operators in terms of the tomogram w and Hermite polynomials leads to the result (Appendix B)

$$\langle a^{\dagger k} a^l \rangle = C_{kl} \sum_{m=0}^{k+l} \exp \left(-i(k-l) \left(\frac{m\pi}{k+l+1} \right) \right) \int_{-\infty}^{\infty} dX_{\theta} w \left(X_{\theta}, \frac{m\pi}{k+l+1} \right) H_{k+l}(X_{\theta}), \quad (2.20)$$

where

$$C_{kl} = \frac{k!l!}{(k+l+1)! \sqrt{2^{k+l}}}.$$

This form is useful for computing D_q numerically. We therefore need to consider $(k+l+1)$ values of θ in order to calculate a moment of order $(k+l)$. In a single tomogram, this amounts to using $(k+l+1)$ probability distributions $w(X_{\theta})$ corresponding to these chosen values of θ , in order to compute D_q . As the system evolves in time, the extent of squeezing at various instants is determined from the instantaneous tomograms in this manner.

For the squeezed vacuum, $|\alpha\rangle$ and $|\alpha, 1\rangle$ we have verified that the variance and hence the Hong-Mandel (equivalently Hillery-type squeezing) properties inferred directly from tomograms are in excellent agreement with corresponding results obtained analytically from the state. We have also computed $\langle (\Delta x)^4 \rangle$ (equivalently the higher-order Hong-Mandel squeezing parameter) directly from the tomogram for initial states $|\alpha\rangle$ and $|\alpha, 1\rangle$ evolving under the Kerr Hamiltonian and the cubic Hamiltonian (Figs. 2.8 (a), (b)). Without loss of generality, we have set $\alpha = 1$. From these figures it is evident that independent of the precise nature of the initial field state, $\langle (\Delta x)^4 \rangle$ oscillates more rapidly in the case of the cubic Hamiltonian compared to the Kerr Hamiltonian. Earlier these squeezing properties were investigated for an initial CS and 1-PACS evolving under a Kerr Hamiltonian alone [44] by calculating $\langle (\Delta x)^4 \rangle$ explicitly for the state at different instants of time. Our results from the corresponding tomograms are in excellent agreement with these.

Figure 2.9 (a) is a plot of D_1 versus $\nu = \alpha^2$ (α real) at $T_{rev}/2$ for an initial CS evolving under both the Kerr and cubic Hamiltonians for $0 \leq \alpha < \sqrt{3}$. It is evident that the state is squeezed for a larger range of values of ν , and that the numerical value

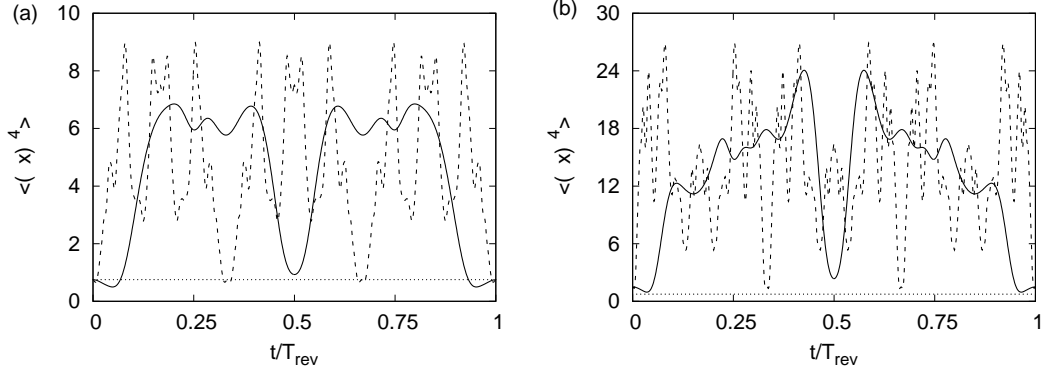


Figure 2.8: Hong-Mandel squeezing as a function of scaled time t/T_{rev} for initial states (a) $|\alpha\rangle$ and (b) $|\alpha, 1\rangle$ for $\alpha = 1$, corresponding to the Kerr (solid) and cubic (dashed) Hamiltonians. The horizontal line at 0.75 denotes the value below which the state is squeezed.

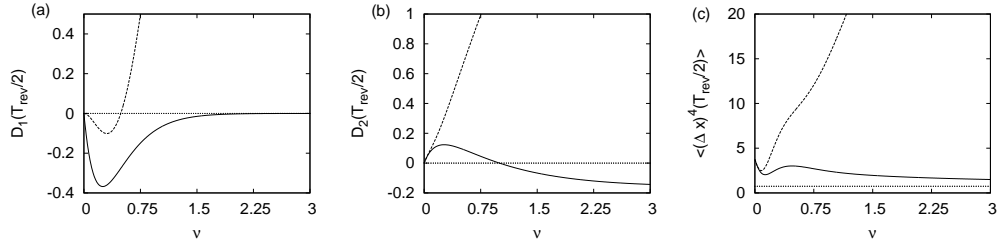


Figure 2.9: (a) D_1 for initial $|\alpha\rangle$, (b) D_2 for initial $|\alpha, 1\rangle$, and (c) $\langle (\Delta x)^4 \rangle$ for initial $|\alpha, 1\rangle$ vs. ν at instant $T_{rev}/2$, corresponding to the Kerr (solid) and cubic (dashed) Hamiltonians. The horizontal line at 0 in (a) and (b) ($3/4$ in (c)) denotes the value below which the state is squeezed.

of D_1 is larger for a given ν in the case of the Kerr Hamiltonian as compared with the cubic Hamiltonian.

For the same parameter values, we have also considered an initial state $|\alpha, 1\rangle$ and obtained D_2 from the tomogram at $T_{rev}/2$. While D_2 is not negative for any ν in this range for the cubic Hamiltonian, it becomes negative for $\nu \geq 0.8$ approximately for the Kerr Hamiltonian (Fig. 2.9 (b)). In contrast $\langle (\Delta x)^4 \rangle$ is never less than $3/4$ in both cases over this range of values of ν (Fig. 2.9 (c)).

2.4 The double-well BEC: A tomographic approach

2.4.1 The model

We now proceed to examine nonclassical effects in a BEC condensed in a double-well potential. The effective Hamiltonian of this bipartite system, setting $\hbar = 1$, is [45]

$$H_{\text{BEC}} = \omega_0 N_{\text{tot}} + \omega_1 (a^\dagger a - b^\dagger b) + U N_{\text{tot}}^2 - \lambda (a^\dagger b + ab^\dagger), \quad (2.21)$$

where ω_0 , ω_1 and λ are constants with appropriate dimensions. In this case, (a, a^\dagger) and (b, b^\dagger) are the boson annihilation and creation operators corresponding to the two subsystems A and B, which comprise the atomic species condensed in the two wells. Here, $[a, a^\dagger] = 1$, $[b, b^\dagger] = 1$ and all other commutators are equal to zero. $N_{\text{tot}} = (a^\dagger a + b^\dagger b)$ and U is the strength of the nonlinearity. It is easy to see that $[H_{\text{BEC}}, N_{\text{tot}}] = 0$.

We denote by $|\alpha_a\rangle$ (respectively $|\alpha_b\rangle$) the CS formed from the condensate corresponding to subsystem A [resp. B] and by $|\alpha_a, 1\rangle$ [$|\alpha_b, 1\rangle$] a 1-boson-added CS corresponding to subsystem A [B]. The initial states considered by us are factored product states of the form $|\alpha_a\rangle \otimes |\alpha_b\rangle$ (denoted by $|\Psi_{00}\rangle$), $|\alpha_a, 1\rangle \otimes |\alpha_b, 1\rangle$ (denoted by $|\Psi_{11}\rangle$) and $|\alpha_a, 1\rangle \otimes |\alpha_b\rangle$ (denoted by $|\Psi_{10}\rangle$).

In general, the state at a subsequent time t is entangled. It has been shown [45] that corresponding to the initial state $|\Psi_{00}\rangle$ we have

$$|\Psi_{00}(t)\rangle = \exp(-(|\alpha_a|^2 + |\alpha_b|^2)/2) \sum_{p,q=0}^{\infty} \frac{(\alpha(t))^p (\beta(t))^q}{\sqrt{p!q!}} \exp(-it(\omega_0(p+q) + U(p+q)^2)) |p, q\rangle. \quad (2.22)$$

We recall that $|p, q\rangle$ denotes $|p\rangle \otimes |q\rangle$ where $\{|p\rangle\}$, $\{|q\rangle\}$ are the boson number basis states of subsystems A and B respectively, and,

$$\alpha(t) = \alpha_a \cos(\lambda_1 t) + i \frac{\sin(\lambda_1 t)}{\lambda_1} (\lambda \alpha_b - \omega_1 \alpha_a), \quad (2.23)$$

$$\beta(t) = \alpha_b \cos(\lambda_1 t) + i \frac{\sin(\lambda_1 t)}{\lambda_1} (\lambda \alpha_a + \omega_1 \alpha_b), \quad (2.24)$$

and $\lambda_1 = \sqrt{\omega_1^2 + \lambda^2}$.

We have used a similar procedure (outlined in Appendix C) to obtain the states $|\Psi_{10}(t)\rangle, |\Psi_{11}(t)\rangle$ and the expression for the density matrix corresponding to the factored product of generic boson-added coherent states $|\alpha_a, m_1\rangle \otimes |\alpha_b, m_2\rangle$ (m_1, m_2 : positive integers). We denote this density matrix by $\rho_{m_1, m_2}(t)$. We give the final expressions below. We have

$$|\Psi_{10}(t)\rangle = \frac{1}{d_{10}} \left(a^\dagger \lambda_1 \cos(\lambda_1 t) + i(\lambda b^\dagger - \omega_1 a^\dagger) \sin(\lambda_1 t) \right) \times \exp(-iU(2N_{\text{tot}} + 1)t) |\Psi_{00}(t)\rangle, \quad (2.25)$$

and

$$|\Psi_{11}(t)\rangle = \frac{1}{d_{11}} \left(2\omega_1^2 a^\dagger b^\dagger + \omega_1 \lambda (a^{\dagger 2} - b^{\dagger 2}) + \cos(2\lambda_1 t) (2\lambda^2 a^\dagger b^\dagger - \omega_1 \lambda (a^{\dagger 2} - b^{\dagger 2})) + i \sin(2\lambda_1 t) \lambda \lambda_1 (a^{\dagger 2} + b^{\dagger 2}) \right) \times \exp(-4iU(N_{\text{tot}} + 1)t) |\Psi_{00}(t)\rangle. \quad (2.26)$$

Here $d_{10} = \lambda_1 \exp(i\omega_0 t) \sqrt{1 + |\alpha_a|^2}$ and $d_{11} = 2\lambda_1^2 \exp(2i\omega_0 t) \sqrt{1 + |\alpha_a|^2} \sqrt{1 + |\alpha_b|^2}$.

To obtain an expression for $\rho_{m_1, m_2}(t)$, we first define $p_{\text{max}} = (k + m_2 - l)$ and $q_{\text{max}} = (l + m_1 - k)$. Then,

$$M_{m_1, m_2}(t) = \frac{1}{\mu} \left[\sum_{k=0}^{m_1} \sum_{l=0}^{m_2} \sum_{p=0}^{p_{\text{max}}} \sum_{q=0}^{q_{\text{max}}} (-1)^{k-p} \binom{m_1}{k} \binom{m_2}{l} \binom{p_{\text{max}}}{p} \binom{q_{\text{max}}}{q} \exp(-i\lambda_1 t (2(k-l) + m_2 - m_1)) (\cos(\kappa/2))^{(k+l+p+q)} (\sin(\kappa/2))^{(2(m_1+m_2)-(k+l+p+q))} a^{\dagger(p+q_{\text{max}}-q)} b^{\dagger(q+p_{\text{max}}-p)} \right] \exp(-i\omega_0 t (m_1 + m_2)) \times \exp(-iUt(m_1 + m_2)(2N_{\text{tot}} + m_1 + m_2)). \quad (2.27)$$

Here $\mu = \sqrt{m_1! L_{m_1}(-|\alpha_a|^2) m_2! L_{m_2}(-|\alpha_b|^2)}$ and $\kappa = \tan^{-1}(\lambda/\omega_1)$. $L_m(-|\alpha|^2)$ are the Laguerre polynomials which appear in the normalisation of an m -boson-added CS

$|\alpha, m\rangle$. Then,

$$\rho_{m_1, m_2}(t) = M_{m_1, m_2}(t) |\Psi_{00}(t)\rangle \langle \Psi_{00}(t)| M_{m_1, m_2}^\dagger(t). \quad (2.28)$$

This expression for the general density matrix can be easily seen to reduce to the forms needed in our case where the states are $|\Psi_{00}(t)\rangle$, $|\Psi_{11}(t)\rangle$ and $|\Psi_{10}(t)\rangle$.

2.4.2 The Revival Phenomena

A straightforward calculation reveals that full and fractional revivals occur provided $\omega_0 = mU$, $\lambda_1 = m'U$, $m, m' \in \mathbb{Z}$, and $(m + m')$ is odd. Here the revival time $T_{rev} = \pi/U$. This follows from the periodicity property of $\exp(-iUN_{\text{tot}}^2)$. For instance, we can easily show that for an initial state $|\Psi_{00}\rangle$, the state at the instant $\pi/(sU)$ (s : even integer) is

$$\begin{aligned} |\Psi_{00}(\pi/sU)\rangle &= \sum_{j=0}^{s-1} f_j |\alpha(\pi/sU)e^{-i\pi(m+2j)/s}\rangle \\ &\otimes |\beta(\pi/sU)e^{-i\pi(m+2j)/s}\rangle. \end{aligned} \quad (2.29)$$

If s is an odd integer,

$$\begin{aligned} |\Psi_{00}(\pi/sU)\rangle &= \sum_{j=0}^{s-1} g_j |\alpha(\pi/sU)e^{-i\pi(m+2j+1)/s}\rangle \\ &\otimes |\beta(\pi/sU)e^{-i\pi(m+2j+1)/s}\rangle. \end{aligned} \quad (2.30)$$

We note that $\alpha(\pi/(sU))$ and $\beta(\pi/(sU))$ are obtained from Eqs. (2.23) and (2.24).

We recall that in the single-mode system the occurrence of full and fractional revivals are related to the presence of distinct strands in the tomogram. In this bipartite system however, the tomogram is a 4-dimensional hypersurface. Hence we need to consider appropriate sections to identify and examine nonclassical effects. The 2-dimensional section $(X_{\theta_B} - X_{\theta_A})$ obtained by choosing a specific value for θ_A and θ_B , is a natural choice for investigating not only the revival phenomena but also the state's squeezing properties. In contrast to the single-mode case where strands appear in the tomograms, these sections are characterised by ‘blobs’ at instants of fractional revivals.

The number of blobs gives the number of subpackets in the wave packet.

Although $|\alpha\rangle$ is expanded as an infinite superposition of boson number states, in practice numerical computations can be carried out using only a large but finite sum of these basis states. While this is the procedure that we have used, an alternative is to use truncated coherent state (TCS) [46] instead of the standard CS. The latter are defined as

$$|\alpha\rangle_{tcs} = \frac{1}{\left(\sum_{n=0}^{N_{max}} (|\alpha|^{2n}/n!)\right)^{1/2}} \sum_{p=0}^{N_{max}} \frac{\alpha^p}{\sqrt{p!}} |p\rangle. \quad (2.31)$$

where N_{max} is a sufficiently large but finite integer. We have verified that the revival phenomena and the squeezing properties as observed from appropriate tomograms in these two approaches agree remarkably well. We have set $\theta_A = \theta_B = 0$, $\omega_0 = 10$, $\omega_1 = 3$, $\lambda = 4$, $U = 1$, and $\alpha_a = \alpha_b = \sqrt{10}$ in our numerical computation pertaining to revivals and fractional revivals. We note that with this choice of values, the necessary conditions for the revival phenomena to occur are satisfied, namely, $\omega_0 = mU$, $\lambda_1 = m'U$, $m, m' \in \mathbb{Z}$, and $(m + m')$ is odd. Figures 2.10 (a)-(d) are tomograms corresponding to different fractional revivals for the initial state $|\Psi_{00}\rangle$. At instants $T_{rev}/4$, $T_{rev}/3$ and T_{rev} (Figs. 2.10 (a), (b) and (d) respectively), there are 4, 3 and a single blob respectively in the corresponding tomograms along with interference patterns. However in Fig. 2.10 (c) corresponding to the instant $T_{rev}/2$ blobs are absent and we merely see interference patterns. This is primarily due to the specific choice of *real* values of α_a and α_b as explained below. At the instant $T_{rev}/2$ it follows from Eq. (2.22) that the state of the system can be expanded in terms of superpositions of factored products of CS corresponding to A and B as

$$\begin{aligned} |\Psi_{00}(T_{rev}/2)\rangle &= \frac{(1-i)}{2} |-2i/\sqrt{10}\rangle \otimes |-14i/\sqrt{10}\rangle \\ &+ \frac{(1+i)}{2} |2i/\sqrt{10}\rangle \otimes |14i/\sqrt{10}\rangle. \end{aligned} \quad (2.32)$$

It is now straightforward to see why the interference patterns alone appear in the tomogram (Fig. 2.10 (c)), as a simple calculation gives

$$\begin{aligned} |\Psi_{00}(X_{A0}, X_{B0})|^2 &= |\langle X_{A0}, 0; X_{B0}, 0 | \Psi_{00}(T_{rev}/2) \rangle|^2 \\ &= \frac{1}{\pi} e^{-(X_{A0}^2 + X_{B0}^2)} \left(1 - \sin(4(X_{A0} + 7X_{B0})/\sqrt{5})\right). \end{aligned} \quad (2.33)$$

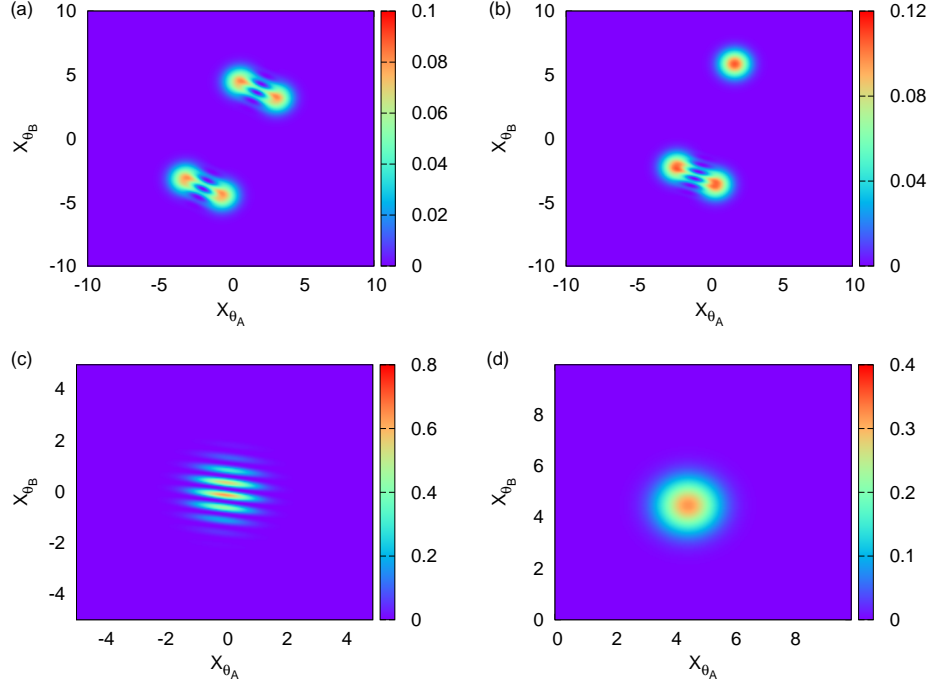


Figure 2.10: Sections of the optical tomogram for $\theta_A = \theta_B = 0$ at instants (a) $T_{rev}/4$, (b) $T_{rev}/3$, (c) $T_{rev}/2$, and (d) T_{rev} . $\alpha_a = \alpha_b = \sqrt{10}$, and initial state $|\Psi_{00}\rangle$.

Here X_{A0} denotes X_{θ_A} for $\theta_A = 0$ and X_{B0} denotes X_{θ_B} for $\theta_B = 0$. In contrast, it can be seen that if α_a and α_b are generic complex numbers, two blobs together with the interference pattern would appear at $T_{rev}/2$ also. Similar results hold for initial states $|\Psi_{11}\rangle$ and $|\Psi_{10}\rangle$.

2.4.3 Squeezing and higher-order squeezing properties of the condensate

The extent of Hong-Mandel squeezing is obtained as in the single-mode example, by calculating the central moments of the probability distribution corresponding to a given quadrature. We examine two-mode squeezing by evaluating appropriate moments of the quadrature variable $\eta = (a + a^\dagger + b + b^\dagger)/(2\sqrt{2})$. These are obtained from the $\theta_A = \theta_B = 0$ section of the tomogram as the system evolves in time. We have also obtained these moments by explicit calculation of the relevant expectation values of η in the state of the system at different instants of time. In both cases the initial state is $|\Psi_{00}\rangle$. In Figs. 2.11 (a)-(d), $2q$ -order moments for $q = 1, 2, 3$ and 4 obtained both from the states and directly from the tomogram are plotted as functions of time. It is evident that they are in excellent agreement with each other at all instants. The horizontal line

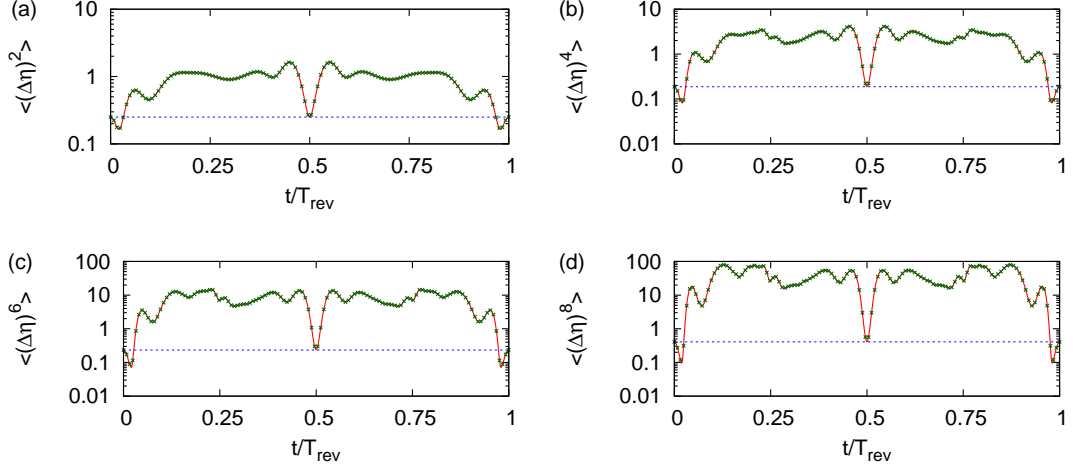


Figure 2.11: $2q$ -order moment of $\eta = (a + a^\dagger + b + b^\dagger)/2\sqrt{2}$ vs. t/T_{rev} for initial state $|\Psi_{00}\rangle$, $|\alpha_a| = |\alpha_b| = 1$, and $q =$ (a) 1, (b) 2, (c) 3, and (d) 4. Moments calculated from the tomogram (green) and moments from unitarily evolved state (red). The horizontal line denotes the value below which q -order squeezing occurs ($1/4$, $3/16$, $15/64$, and $105/256$ for $q = 1, 2, 3, 4$ respectively).

in each figure denotes the value below which the state is squeezed ($1/4$, $3/16$, $15/64$, and $105/256$ for $q = 1, 2, 3, 4$ respectively). For all values of q considered, the state is squeezed (higher-order squeezed) in the neighborhood of revivals, and the extent of squeezing at various instants is considerably sensitive to the values of q , α_a and α_b as expected.

Turning to Hillery-type higher-order squeezing, we recall that in the single-mode case we used Eq. (2.20) for this calculation. A straightforward extension to the two-mode system gives us the expression

$$\begin{aligned} \langle a^{\dagger k} a^l b^{\dagger m} b^n \rangle &= c_{klmn} \sum_{p=0}^{k+l} \sum_{q=0}^{m+n} \exp(-i(k-l)\theta_{Ap}) \\ &\quad \exp(-i(m-n)\theta_{Bq}) \int_{-\infty}^{+\infty} dX_{\theta_{Ap}} \int_{-\infty}^{+\infty} dX_{\theta_{Bq}} \\ &\quad w(X_{\theta_{Ap}}, \theta_{Ap}; X_{\theta_{Bq}}, \theta_{Bq}) H_{k+l}(X_{\theta_{Ap}}) H_{m+n}(X_{\theta_{Bq}}). \end{aligned} \quad (2.34)$$

Here

$$c_{klmn} = \frac{k!l!m!n!}{(k+l+1)!(m+n+1)!\sqrt{2^{k+l+m+n}}},$$

$\theta_{Ap} = \frac{p\pi}{k+l+1}$, and $\theta_{Bq} = \frac{q\pi}{m+n+1}$. We note that $(k+l+1)(m+n+1)$ gives the number of 2-dimensional slices of the tomogram that are required to calculate $\langle a^{\dagger k} a^l b^{\dagger m} b^n \rangle$.

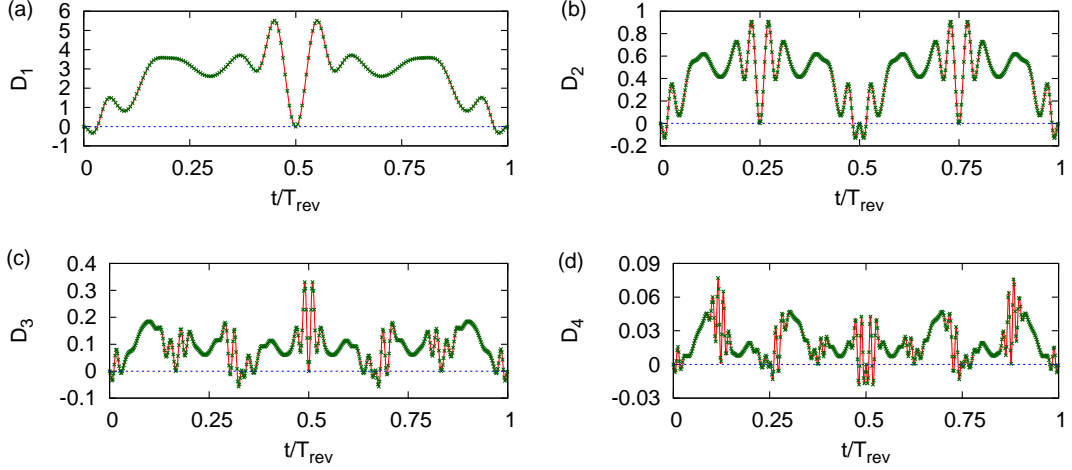


Figure 2.12: $D_q(t)$ vs. t/T_{rev} for initial state $|\Psi_{00}\rangle$, $|\alpha_a| = |\alpha_b| = 1$, and $q =$ (a) 1, (b) 2, (c) 3, and (d) 4. Squeezing parameter from the tomogram (green) and from unitarily evolved state (red). The horizontal line corresponds to $D_q(t) = 0$.

From Figs. 2.12 (a)-(d), we see that $D_q(t)$ obtained both from the states and directly from the tomogram for an initial state $|\Psi_{00}\rangle$ are in excellent agreement. (The expression in Eq. (2.19) holds in this case also, with $Z_1 = (a^q + a^{\dagger q} + b^q + b^{\dagger q})/(2\sqrt{2})$ and $Z_2 = (a^q - a^{\dagger q} + b^q - b^{\dagger q})/(2\sqrt{2}i)$). It is clear that for higher values of q there are more instants of time when higher-order squeezing occurs as expected from the fact that more cross-terms involving the creation and destruction operators arise with increase in q . We have also verified that both the Hong-Mandel and Hillery-type squeezing and higher-order squeezing parameters obtained from tomograms and from expectation values of appropriate operators for the initial states $|\Psi_{10}\rangle$ and $|\Psi_{11}\rangle$ are equal to each other at all instants between $t = 0$ and T_{rev} .

2.4.4 Subsystem entropies from tomograms

We now proceed to examine the subsystem's entropic squeezing properties by computing the subsystem information entropy $S(\theta_A)$ at various instants of time. (Here, without loss of generality we have considered subsystem A by setting $\theta_B = 0$, and integrating over the full range of X_{θ_B} to obtain $w_A(X_{\theta_A}, \theta_A)$). Expressed in terms of the subsystem tomogram,

$$S(\theta_A) = - \int_{-\infty}^{\infty} dX_{\theta_A} w_A(X_{\theta_A}, \theta_A) \ln w_A(X_{\theta_A}, \theta_A). \quad (2.35)$$

For our purpose, we set $\theta_A = 0$ (i.e., the x -quadrature). Denoting the corresponding

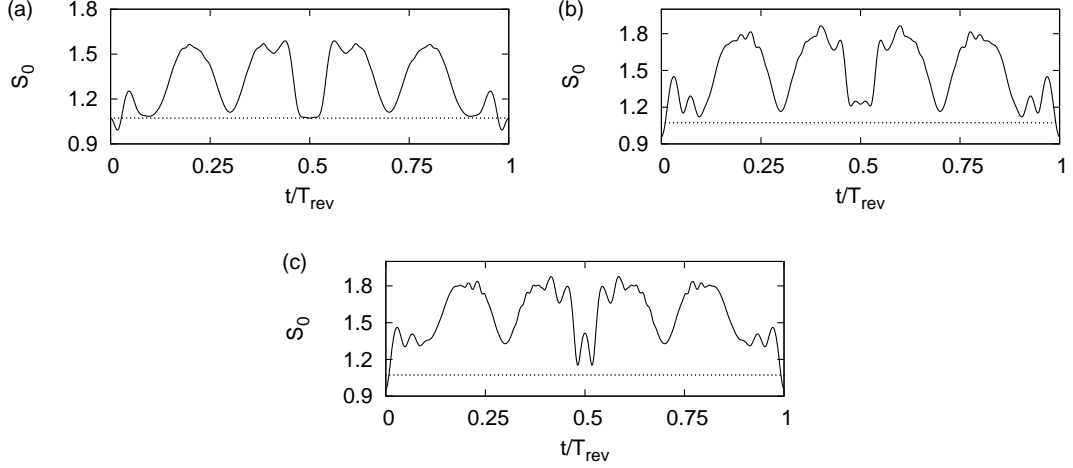


Figure 2.13: Subsystem entropy S_0 vs. t/T_{rev} for initial states (a) $|\Psi_{00}\rangle$, (b) $|\Psi_{10}\rangle$, and (c) $|\Psi_{11}\rangle$ with $\alpha_a = \alpha_b = 1$.

tomogram by $w_A(x)$, the subsystem entropy S_0 is now equal to $-\int_{-\infty}^{\infty} dx w_A(x) \ln w_A(x)$. It can be shown that for a given state, $S_0 \leq (1/2)[1 + \ln \pi + \ln(2\langle(\Delta x)^2\rangle)]$, where $\langle(\Delta x)^2\rangle$ is the variance in x [47]. The state exhibits entropic squeezing if S_0 is less than $(1/2)(1 + \ln \pi)$. Plots of S_0 versus scaled time t/T_{rev} are shown in Figs. 2.13 (a)-(c) for initial states $|\Psi_{00}\rangle$, $|\Psi_{10}\rangle$ and $|\Psi_{11}\rangle$ respectively. The horizontal line in these figures denotes the numerical value below which entropic squeezing occurs. We see that entropic squeezing occurs close to $t = 0$ and T_{rev} . At other instants the subsystem entropy is significantly higher for initial states $|\Psi_{10}\rangle$ and $|\Psi_{11}\rangle$ compared to initial ideal coherence. This feature is very prominent close to $T_{rev}/2$. Further, comparing Figs. 2.13 (b) and (c) it is clear that S_0 is larger at all instants if both subsystems depart from coherence initially, compared to the case where one of them displays initial coherence.

The variation of S_0 with $|\alpha_a|^2$ and $|\alpha_b|^2$, at $T_{rev}/2$, for initial states $|\Psi_{00}\rangle$, $|\Psi_{10}\rangle$ and $|\Psi_{11}\rangle$ are shown in Figs. 2.14 (a), (b) and (d) respectively. Figure 2.14 (c) corresponds to the entropy of subsystem B for an initial state $|\Psi_{10}\rangle$. This facilitates comparison of the features in Figs. 2.14 (b) and (c) where for the same asymmetric initial state the two subsystems examined are different. It is evident that S_0 corresponding to A is not squeezed while that corresponding to B exhibits squeezing for certain values of α_a and α_b . The role played by the asymmetry in the initial states of the two subsystems is thus clearly brought out in these figures. It is also clear that entropic squeezing is more if the initial states of the subsystems are coherent.

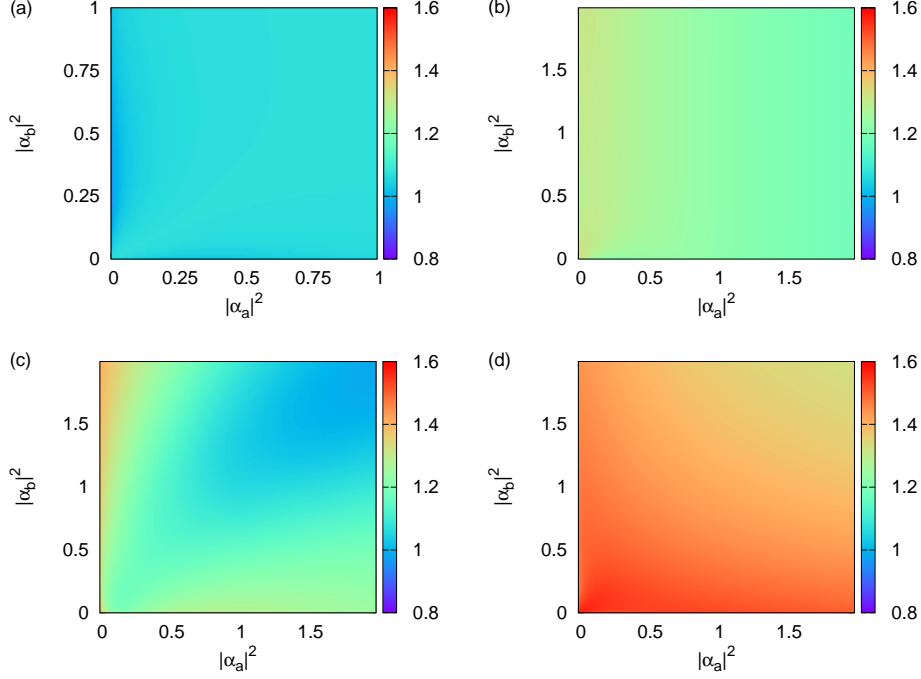


Figure 2.14: Variation of S_0 with $|\alpha_a|^2$ and $|\alpha_b|^2$ at $T_{rev}/2$ for initial states (a) $|\Psi_{00}\rangle$, (b) and (c) $|\Psi_{10}\rangle$, and (d) $|\Psi_{11}\rangle$. Figures (a), (b) and (d) correspond to subsystem A and (c) to B.

2.5 Concluding remarks

We have established how tomograms can be exploited to identify and characterise a variety of nonclassical effects such as the wave packet revival phenomena and squeezing and higher-order squeezing in both single-mode and bipartite systems. While a simple relation has been shown to exist between the number of strands in tomogram patterns and the nature of fractional revivals when a single-mode radiation field propagates in a Kerr medium [17], our investigations reveal that this no longer holds even in single-mode systems which display super-revivals during temporal evolution. The role played by decoherence due to amplitude decay and phase damping of the state has also been discussed. We have also analysed the revival phenomena in bipartite systems such as the double-well BEC evolving in time, *solely* from tomograms. We have obtained the extent of squeezing, higher-order Hong-Mandel and Hillery-type squeezing from tomograms. We have also investigated entropic squeezing from the tomograms in the case of the double-well BEC.

In the next chapter, we discuss procedures for extracting the extent of entanglement directly from quantum state tomograms in the context of both continuous-variable and

hybrid quantum systems. We propose several entanglement indicators for this purpose. We compare the extent of entanglement as captured by these indicators with ξ_{SVNE} which is a standard measure of entanglement.

CHAPTER 3

Tomographic entanglement indicators and avoided energy-level crossings

3.1 Introduction

In this chapter, we introduce various entanglement indicators that can be obtained directly from appropriate tomograms. We assess their performance as quantifiers of the extent of entanglement in both bipartite and multipartite systems. We have considered both CV and HQ systems. Our reference for comparison is set by ξ_{SVNE} . We recall that $\xi_{\text{SVNE}} = -\text{Tr}(\rho \log_2 \rho)$, where ρ is the subsystem density matrix [48].

Some of the entanglement indicators we examine are inspired by classical tomography. Indicators of correlations between different parts of a *classical* system have been used extensively in various applications such as automated image processing. While these correlators are obtained from classical tomograms, their definitions however, are not intrinsically classical in nature. It is therefore worth examining their applicability in quantum contexts. Since correlations are inherently present in entangled states of quantum systems, a natural question that arises is whether the performance of entanglement quantifiers obtained from classical correlators is comparable to that of standard indicators such as ξ_{SVNE} .

We focus on quantum systems whose eigenspectrums exhibit avoided energy-level crossings. In these systems, the spacings between energy levels change significantly with changes in the parameters, with two or more levels moving close to each other for specific values of the parameters, and then moving away as these values change. Our interest stems from the fact that extensive studies [49–51] have established that entanglement as measured by standard indicators such as ξ_{SVNE} is generically at an extremum at an avoided crossing. Typically, the energy spectrum and the spacing between the energy levels depend on the strengths of the nonlinearity and the coupling between subsystems. With changes in the values of these parameters, the spacing between adjacent levels can decrease, and even tend to zero, resulting in an energy-level crossing.

According to the von Neumann-Wigner no-crossing theorem, energy levels within a multiplet generically avoid crossing, provided only one of the parameters is varied in the Hamiltonian governing the system. In what follows, we investigate how effectively some of these entanglement indicators mimic the behaviour of ξ_{SVNE} close to avoided crossings.

Energy-level crossings display other interesting features. Since they affect the level spacings and their probability distribution [52], they are also important from the point of view of non-integrability and quantum chaos (see, for instance, [53]). In addition, avoided crossings point to phase transitions which trigger a change in the quantum correlations in the system [54, 55, 49, 50]. This aspect has been investigated extensively both theoretically and in experiments [56–61].

The bipartite CV systems that we examine here are a BEC in a double-well trap [45] introduced in Chapter 2, and a multi-level atom interacting with a radiation field [62]. We also investigate a multipartite HQ system [63, 64] comprising qubits interacting with a microwave field that is effectively described by the Tavis-Cummings model [65].

In the next section we introduce the entanglement indicators to be employed. In Section 3.3, we investigate how these indicators behave close to avoided crossings in the two bipartite CV models mentioned above. In Section 3.4, we extend our analysis to the multipartite HQ model. We conclude with brief remarks.

3.2 Entanglement indicators from tomograms

A typical example of a bipartite CV system is two coupled oscillators (equivalently, a single-mode radiation field interacting with a multi-level atom modelled as an oscillator) with (a, a^\dagger) (respectively, (b, b^\dagger)) being the oscillator annihilation and creation operators corresponding to the two subsystems A and B. We recall that Eqs. (2.7), (2.10) and (2.11) define the tomograms corresponding to the full system and the two subsystems respectively. In order to estimate the degree of correlation between the subsystems, we use the following tomographic entropies. The bipartite tomographic

entropy is given by

$$S(\theta_A, \theta_B) = - \int_{-\infty}^{\infty} dX_{\theta_A} \int_{-\infty}^{\infty} dX_{\theta_B} w(X_{\theta_A}, \theta_A; X_{\theta_B}, \theta_B) \times \log_2 w(X_{\theta_A}, \theta_A; X_{\theta_B}, \theta_B). \quad (3.1)$$

The subsystem tomographic entropy (generalizing Eq. (2.35)) is

$$S(\theta_i) = - \int_{-\infty}^{\infty} dX_{\theta_i} w_i(X_{\theta_i}, \theta_i) \log_2 [w_i(X_{\theta_i}, \theta_i)] \quad (i = A, B). \quad (3.2)$$

Some of the correlators that we examine are obtained from a section of the tomogram corresponding to specific values of θ_A and θ_B . The efficacy of such a correlator as a measure of entanglement is therefore sensitive to the choice of the tomographic section. We now define these correlators, and the corresponding entanglement indicators.

The mutual information $\varepsilon_{\text{TEI}}(\theta_A, \theta_B)$ which we get from the tomogram of a quantum system can carry signatures of entanglement. This quantity is expressed in terms of the tomographic entropies defined above as

$$\varepsilon_{\text{TEI}}(\theta_A, \theta_B) = S(\theta_A) + S(\theta_B) - S(\theta_A, \theta_B). \quad (3.3)$$

Indicators based on the inverse participation ratio (IPR) are also found to be good candidates for estimating the extent of entanglement [66, 36]. The participation ratio is a measure of delocalisation in a given basis. The IPR corresponding to a bipartite system in the basis of the rotated quadrature operators is defined as

$$\eta_{AB}(\theta_A, \theta_B) = \int_{-\infty}^{\infty} dX_{\theta_A} \int_{-\infty}^{\infty} dX_{\theta_B} [w(X_{\theta_A}, \theta_A; X_{\theta_B}, \theta_B)]^2. \quad (3.4)$$

The IPR for each subsystem is given by

$$\eta_i(\theta_i) = \int_{-\infty}^{\infty} dX_{\theta_i} [w_i(X_{\theta_i}, \theta_i)]^2 \quad (i = A, B). \quad (3.5)$$

The entanglement indicator in this case is given by

$$\varepsilon_{\text{IPR}}(\theta_A, \theta_B) = 1 + \eta_{AB}(\theta_A, \theta_B) - \eta_A(\theta_A) - \eta_B(\theta_B). \quad (3.6)$$

Apart from these, we have examined two other correlators which are familiar in the context of classical tomograms. The first of these is the Pearson correlation coefficient [67] between two random variables X and Y , given by

$$\text{PCC}(X, Y) = \frac{\text{Cov}(X, Y)}{(\Delta X)(\Delta Y)}. \quad (3.7)$$

Here ΔX , ΔY are the standard deviations of X and Y respectively, and $\text{Cov}(X, Y)$ is their covariance. Of direct relevance to us is $\text{PCC}(X_{\theta_A}, X_{\theta_B})$ calculated for fixed values of θ_A and θ_B . Since the quantifier of entanglement between two subsystems must be non-negative, a simple definition of the entanglement indicator in this case would be

$$\varepsilon_{\text{PCC}}(\theta_A, \theta_B) = |\text{PCC}(X_{\theta_A}, X_{\theta_B})|. \quad (3.8)$$

This indicator captures the effect of linear correlations. Our motivation for assessing this indicator arises from the fact that, in recent experiments on generating and testing the extent of entanglement in CV systems, the variances of suitably chosen conjugate observables and the corresponding standard quantum limit alone are used [68]. We reiterate that these merely capture the extent of linear correlations between two states.

The second indicator (to be denoted by ε_{BD}) that we introduce and use is arrived at as follows. In probability theory, the mutual information [69] between two continuous random variables X and Y can be expressed in terms of the Kullback-Leibler divergence D_{KL} [70] between their joint probability density $p_{XY}(x, y)$ and the product of the corresponding marginal densities $p_X(x) = \int p_{XY}(x, y)dy$ and $p_Y(y) = \int p_{XY}(x, y)dx$, as [71]

$$D_{\text{KL}}[p_{XY} : p_X p_Y] = \int dx \int dy p_{XY}(x, y) \log_2 \frac{p_{XY}(x, y)}{p_X(x)p_Y(y)}, \quad (3.9)$$

The quantity $\varepsilon_{\text{TEI}}(\theta_A, \theta_B)$ defined in Eq. (3.3) is precisely the mutual information in the case of optical tomograms (which are continuous probability distributions):

$$\varepsilon_{\text{TEI}}(\theta_A, \theta_B) = D_{\text{KL}}[w(X_{\theta_A}, \theta_A; X_{\theta_B}, \theta_B) : w_A(X_{\theta_A}, \theta)w_B(X_{\theta_B}, \theta)]. \quad (3.10)$$

A simpler alternative for our purposes is provided by the Bhattacharyya distance D_B [72]

between p_{XY} and $p_X p_Y$, defined as

$$D_B[p_{XY} : p_X p_Y] = -\log_2 \left\{ \int dx \int dy [p_{XY}(x, y) p_X(x) p_Y(y)]^{1/2} \right\}. \quad (3.11)$$

Using Jensen's inequality, it is easily shown that $D_B \leq \frac{1}{2} D_{KL}$. D_B thus gives us an approximate estimate (that is an underestimate) of the mutual information. Based on this quantity, we have an entanglement indicator that is the analogue of Eq. (3.10), namely,

$$\varepsilon_{BD}(\theta_A, \theta_B) = D_B[w(X_{\theta_A}, \theta_A; X_{\theta_B}, \theta_B) : w_A(X_{\theta_A}, \theta) w_B(X_{\theta_B}, \theta)]. \quad (3.12)$$

The dependence on θ_A and θ_B of each of the foregoing entanglement indicators ε is removed by averaging over a representative set of values of those variables. We denote the corresponding averaged value by ξ . In the context of bipartite CV models, we find [34, 36] that averaging $\varepsilon_{TEI}(\theta_A, \theta_B)$ over 25 different values of (θ_A, θ_B) selected at equal intervals in the range $[0, \pi)$ yields a reliable entanglement indicator ξ_{TEI} . A similar averaging of each of the quantities ε_{IPR} , ε_{PCC} and ε_{BD} yields ξ_{IPR} , ξ_{PCC} and ξ_{BD} , respectively.

Next, we turn to hybrid systems of field-atom interactions. For a two-level atom with ground state $|g\rangle$ and excited state $|e\rangle$, the quorum of observables is [73]

$$\begin{aligned} \sigma_x &= \frac{1}{2}(|e\rangle\langle g| + |g\rangle\langle e|), \quad \sigma_y = \frac{1}{2}i(|g\rangle\langle e| - |e\rangle\langle g|), \\ \sigma_z &= \frac{1}{2}(|e\rangle\langle e| - |g\rangle\langle g|). \end{aligned} \quad (3.13)$$

Let $\sigma_z |m\rangle = m |m\rangle$. Then $U(\vartheta, \varphi) |m\rangle = |\vartheta, \varphi, m\rangle$, where $U(\vartheta, \varphi)$ is a general $SU(2)$ transformation parametrised by (ϑ, φ) . Denoting (ϑ, φ) by the unit vector \mathbf{n} , the qubit tomogram is given by

$$w(\mathbf{n}, m) = \langle \mathbf{n}, m | \rho_s | \mathbf{n}, m \rangle \quad (3.14)$$

where ρ_s is the qubit density matrix. Corresponding to each value of \mathbf{n} there exists a complete basis set and hence $\sum_m w(\mathbf{n}, m) = 1$, $\forall \mathbf{n}$. The atomic tomograms are obtained from these, and the corresponding entanglement properties are quantified using appropriate adaptations of the indicators (suitably replacing the integrals by sums) described above. Extension of the foregoing to the multipartite case is straightforward

[11], and the tomograms obtained can be examined on similar lines.

3.3 Avoided energy-level crossings in bipartite CV models

3.3.1 The double-well BEC model

The effective Hamiltonian (Eq. (2.21)) for the system and its diagonalisation are as follows [45]. Setting $\hbar = 1$,

$$H_{\text{BEC}} = \omega_0 N_{\text{tot}} + \omega_1 (a^\dagger a - b^\dagger b) + U N_{\text{tot}}^2 - \lambda (a^\dagger b + ab^\dagger).$$

We recall that (a, a^\dagger) and (b, b^\dagger) are the respective boson annihilation and creation operators of the atoms in wells A and B (the two subsystems), and $N_{\text{tot}} = (a^\dagger a + b^\dagger b)$. U is the strength of nonlinear interactions between atoms within each well, and also between the two wells. $U > 0$, ensuring that the energy spectrum is bounded from below. λ is the linear interaction strength and ω_1 is the strength of the population imbalance between the two wells. The Hamiltonian is diagonalised by the unitary transformation $V = e^{\kappa(a^\dagger b - b^\dagger a)/2}$ (Eq. (C.3) of Appendix C) where $\kappa = \tan^{-1}(\lambda/\omega_1)$, to yield

$$V^\dagger H_{\text{BEC}} V = \tilde{H}_{\text{BEC}} = \omega_0 N_{\text{tot}} + \lambda_1 (a^\dagger a - b^\dagger b) + U N_{\text{tot}}^2, \quad (3.15)$$

with $\lambda_1 = (\lambda^2 + \omega_1^2)^{1/2}$. \tilde{H}_{BEC} and N_{tot} commute with each other. Their common eigenstates are the product states $|k\rangle \otimes |N - k\rangle \equiv |k, N - k\rangle$. Here $N = 0, 1, 2, \dots$ is the eigenvalue of N_{tot} , and $|k\rangle$ is a boson number state, with k running from 0 to N for a given N . The eigenstates and eigenvalues of H_{BEC} are given by

$$|\psi_{N,k}\rangle = V |k, N - k\rangle \quad (3.16)$$

and

$$E(N, k) = \omega_0 N + \lambda_1 (2k - N) + U N^2. \quad (3.17)$$

For numerical analysis we set $\omega_0 = 1, U = 1$.

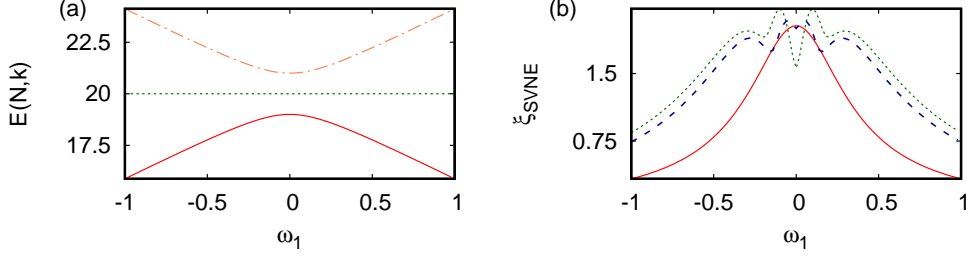


Figure 3.1: (a) $E(N, k)$ vs. ω_1 for $N = 4$ and $k = 0, 2, 4$ in the BEC model. (b) ξ_{SVNE} vs. ω_1 for $N = 4$, $k = 0, 1, 2$. The curves correspond to $k = 0$ (red), 1 (blue), 2 (green) and 4 (orange). $\lambda = 0.25$.

In Fig. 3.1(a), $E(N = 4, k)$ is plotted against ω_1 for $k = 0, 2, 4$, with $\lambda = 0.25$. $E(N, N - k)$ is the reflection of $E(N, k)$ about the value $\omega_0 N + UN^2$. Avoided energy-level crossings are seen at $\omega_1 = 0$. In order to set the reference level for the extent of entanglement between the two wells, we compute $\xi_{\text{SVNE}} = -\text{Tr}(\rho_A \log_2 \rho_A)$, where ρ_A is the reduced density matrix of the subsystem A. (ξ_{SVNE} is also equal to $-\text{Tr}(\rho_B \log_2 \rho_B)$, since $|\psi_{N,k}\rangle$ is a bipartite pure state.) Plots of ξ_{SVNE} corresponding to the state $|\psi_{4,k}\rangle$ for $k = 0, 1, 2$ are shown in Fig. 3.1(b). The states $|\psi_{4,3}\rangle$ and $|\psi_{4,1}\rangle$ have the same ξ_{SVNE} , (as do the states $|\psi_{4,4}\rangle$ and $|\psi_{4,0}\rangle$), owing to the $k \leftrightarrow N - k$ symmetry. It is evident that there is a significant extent of entanglement close to the avoided crossing, and $\omega_1 = 0$ is marked by a local maximum or minimum in ξ_{SVNE} .

Figure 3.2 depicts $\theta_A = 0, \theta_B = \frac{1}{2}\pi$ sections of the tomograms corresponding to the states $|\psi_{4,k}\rangle$ for $k = 0, 1, 2$ and $\omega_1 = 0, 0.1, 1$. It is clear that, for a given value of ω_1 , the qualitative features of the tomograms are altered considerably as k is varied. The patterns in the tomograms also reveal nonlinear correlations between the quadrature variables X_{θ_A} and X_{θ_B} (top panel). For instance, the tomogram slice on the top right shows a probability distribution that is essentially unimodal and symmetric about the origin with the annular structures diminished in magnitude. It is clear that this case is less correlated than the tomogram in the top left corner. This conforms to the observed trend in the extent of entanglement (compare ξ_{SVNE} corresponding to $k = 0$ and $k = 2$ at $\omega_1 = 0$ in Fig. 3.1 (b)). Again, in the bottom panel of the figure, the sub-structures in the patterns increase with increasing k , signifying a higher degree of nonlinear correlation. This is in consonance with the trend in the entanglement at $\omega_1 = 1$ (Fig. 3.1 (b)). We therefore expect ε_{TEI} and its averaged version ξ_{TEI} to be much better entanglement indicators than ε_{PCC} and ξ_{PCC} . We also mention here that the current experimental techniques of testing CV entanglement based on the variances and covariances of suitably

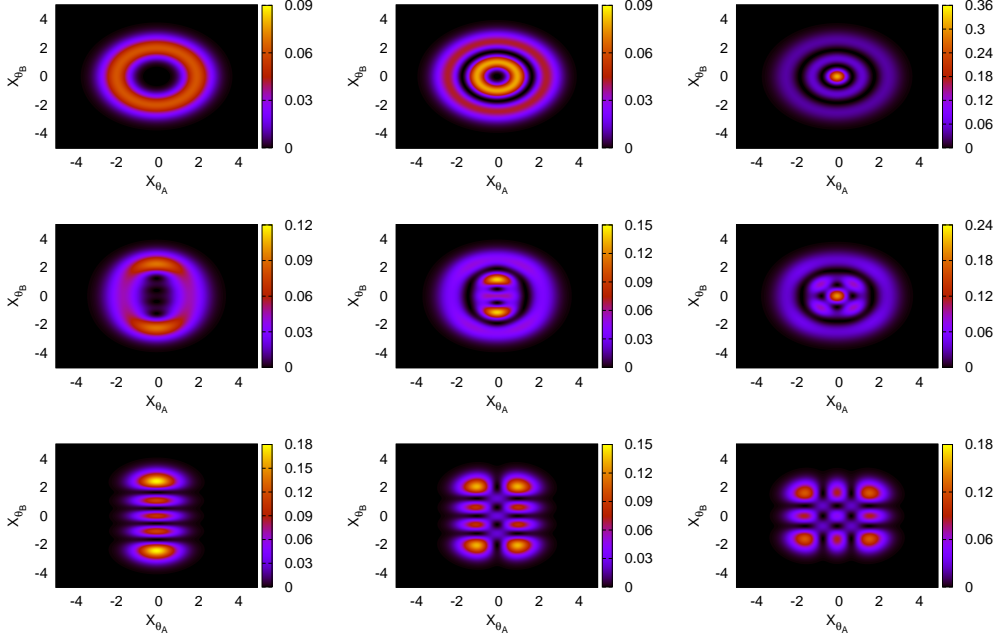


Figure 3.2: $\theta_A = 0, \theta_B = \pi/2$ slice of the tomogram for $N = 4$ in the BEC model. Left to right, $k = 0, 1$ and 2 . Top to bottom, $\omega_1 = 0, 0.1$ and 1 .

chosen observables [68] are not as effective as calculating nonlinear correlators, for the same reason.

Our detailed investigations reveal that ξ_{TEI} and ξ_{IPR} follow the trends in ξ_{SVNE} reasonably well for generic eigenstates of H_{BEC} . This is illustrated in Fig. 3.3, which shows plots of these indicators as functions of ω_1 . Apart from examining the suitability of ε_{PCC} as an entanglement indicator, we have also assessed the extent of linear correlation between any two indicators based on the corresponding PCC, as follows. We have obtained 100 values each of ξ_{TEI} and ξ_{SVNE} for different values of ω_1 in the range $(-1, 1)$ in steps of 0.02. Treating the two sets of values as two sets of random numbers, we obtain the PCC between them, as defined in Eq. (3.7). The PCC between ξ_{TEI} and ξ_{SVNE} (respectively, ξ_{IPR} and ξ_{SVNE}) estimates the extent of linear correlation between the two indicators, and is found to be 0.97 (resp., 0.99) in the case shown in Fig. 3.3 corresponding to $|\psi_{4,2}\rangle$. (In general, the PCC ranges from 1 for complete correlation, to -1 for maximal anti-correlation. Its vanishing indicates the absence of linear correlation).

Figure 3.4 shows the PCC between ξ_{SVNE} and various indicators, for the eigenstates $|\psi_{4,k}\rangle$ where $k = 0, 1, 2, 3, 4$. From Fig. 3.4(a), we see that ξ_{IPR} , ξ_{TEI} and ξ_{BD} are very good entanglement indicators. We have also found that all these indicators improve with increasing N . The performance of the ε -indicators depends, of course, on the specific

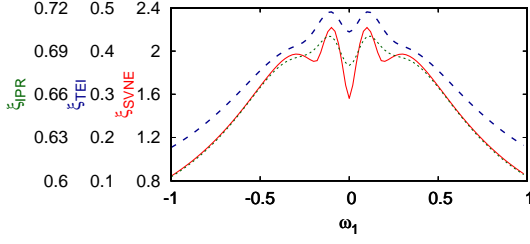


Figure 3.3: ξ_{SVNE} (red), ξ_{TEI} (blue) and ξ_{IPR} (green) vs. ω_1 , for the state $|\psi_{4,2}\rangle$ in the BEC model.

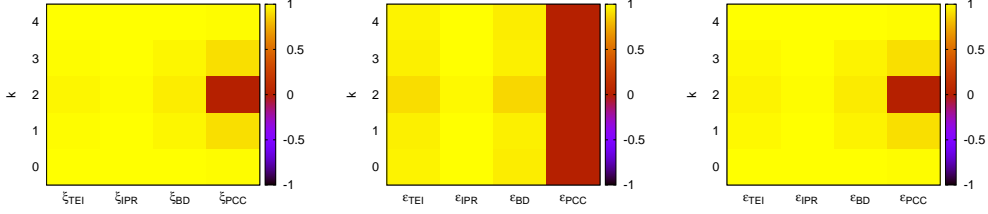


Figure 3.4: Correlation of ξ_{SVNE} with ξ -indicators (left), with ε -indicators for the slice $\theta_A = 0, \theta_B = \pi/2$ (centre), and with ε -indicators for the slice $\theta_A = 0, \theta_B = 0$ (right), for the eigenstates $|\psi_{4,k}\rangle$, $0 \leq k \leq 4$ in the BEC model.

choice of the tomographic section. For instance, ε_{TEI} and ε_{BD} perform marginally better for the slice $\theta_A = 0, \theta_B = 0$ than for the slice $\theta_A = 0, \theta_B = \frac{1}{2}\pi$. It is also evident that ξ_{PCC} does not fare as well as the other indicators. This is to be expected, since ξ_{PCC} only captures linear correlations, as already emphasised.

We have verified that the sensitivity of all the indicators decreases with an increase in λ , the strength of the coupling between the two subsystems (as in Eq. (2.21)). ξ_{IPR} , however, remains closer to ξ_{SVNE} than the other indicators. This fact is consistent with inferences [36] drawn about the relation between the Hamming distance [74] and the efficacy of ξ_{IPR} . We recall that the Hamming distance between two bipartite qudits $|u_1\rangle \otimes |u_2\rangle$ and $|v_1\rangle \otimes |v_2\rangle$ attains its maximum value of 2 when $\langle u_1|v_1\rangle = 0$ and $\langle u_2|v_2\rangle = 0$. A straightforward extension to CV systems implies that the Hamming distance between $|k_1, N - k_1\rangle$ and $|k_2, N - k_2\rangle$ is 2 (so that these states are Hamming-uncorrelated), if $k_1 \neq k_2$. Participation ratios are valid measures of entanglement for superpositions of Hamming-uncorrelated states in spin systems [66]. We will show in this and the next chapter that ξ_{IPR} effectively mimics standard measures of entanglement in CV systems as well. In the present instance, the eigenstates $|\psi_{N,k}\rangle$ are superpositions of the states $\{|j, N - j\rangle\}$ which are Hamming-uncorrelated for different values of j . This is the reason for the usefulness of ξ_{IPR} as an entanglement indicator even for larger values of λ .

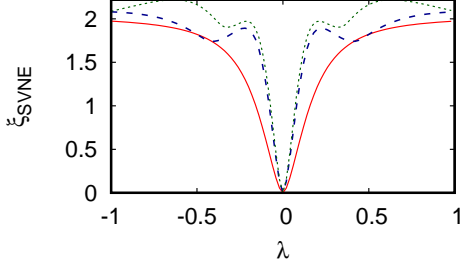


Figure 3.5: ξ_{SVNE} vs. λ for $N = 4$, $k = 0, 1, 2$, in the BEC model. The curves correspond to $k = 0$ (red), 1 (blue) and 2 (green). $\omega_1 = 0.25$.

We now proceed to examine quantitatively the efficacy of the entanglement indicators as functions of λ . For numerical computation we have set $\omega_1 = 0.25$. Consider, as an illustration, plots of the eigenvalues $E(4, k)$ ($k = 0, 2, 4$) as functions of λ . These plots are exactly the same as those in Fig. 3.1(a), with ω_1 replaced by λ on the horizontal axis, since $E(N, k)$ only depends on the parameters ω_1 and λ in the symmetric combination $\lambda_1 = (\lambda^2 + \omega_1^2)^{1/2}$. The avoided crossing of energy levels now occurs at $\lambda = 0$. But this symmetry between ω_1 and λ does not extend to the unitary transformation V , and hence to the eigenstates of H_{BEC} . (Recall that V involves the parameter $\kappa = \tan^{-1}(\lambda/\omega_1)$.) When $\lambda = 0$ there is no linear interaction between the two modes. V then reduces to the identity operator, and H_{BEC} is diagonal in the basis $\{|k, N - k\rangle\}$. We therefore expect the entanglement to vanish at the avoided crossing. This is borne out in Fig. 3.5 in which ξ_{SVNE} for the state $|\psi(4, k)\rangle$ is plotted for different values of k . As before, it suffices to depict the cases $k = 0, 1$ and 2 because of the $k \leftrightarrow N - k$ symmetry. We observe that, in the case $k = 0$, while there is a minimum in ξ_{SVNE} at $\lambda = 0$, there is a maximum in this quantity at $\omega_1 = 0$ (Fig. 3.1(b)).

We have also calculated the PCC between various indicators and ξ_{SVNE} for the set of states $|\psi_{4,k}\rangle$, $0 \leq k \leq 4$. For this purpose, we have used 100 values of each of the ξ -indicators calculated for each λ in the range $[-1, 1]$ with a step size of 0.02. The results are very similar to those already found (see Fig. 3.4) using ω_1 as the variable parameter instead of λ .

3.3.2 Atom-field interaction model

We turn next to the case of a multi-level atom (modelled by an anharmonic oscillator) that is linearly coupled with strength g to a radiation field of frequency ω_F . The effective

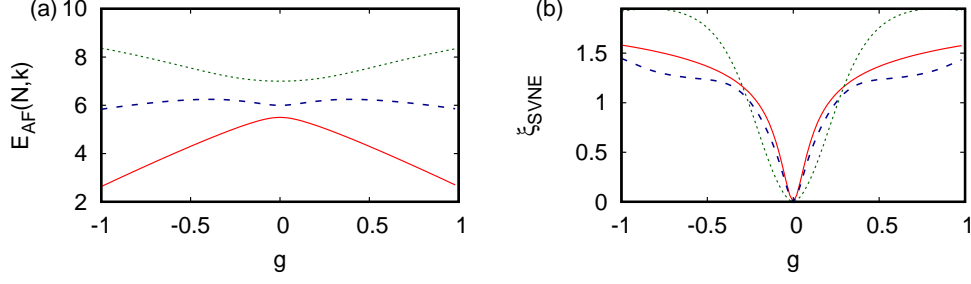


Figure 3.6: (a) $E_{\text{AF}}(N, k)$ and (b) ξ_{SVNE} vs. g for $N = 4$, $k = 0, 1, 2$ in the atom-field interaction model. The curves correspond to $k = 0$ (red), 1 (blue) and 2 (green). $\omega_{\text{F}} = 1.5$, $\omega_{\text{A}} = 1$, $\gamma = 1$.

Hamiltonian (setting $\hbar = 1$) is given by [62]

$$H_{\text{AF}} = \omega_{\text{F}} a^\dagger a + \omega_{\text{A}} b^\dagger b + \gamma b^{\dagger 2} b^2 + g(a^\dagger b + ab^\dagger). \quad (3.18)$$

ω_{A} and γ (> 0 for stability) are constants. (a, a^\dagger) and (b, b^\dagger) are the annihilation and creation operators for the field mode and the oscillator mode, respectively. As before, $N_{\text{tot}} = a^\dagger a + b^\dagger b$ and $[H_{\text{AF}}, N_{\text{tot}}] = 0$. As in the BEC model of the preceding section, the eigenvalues $E_{\text{AF}}(N, k)$ and the common eigenstates $|\phi_{N, k}\rangle$ of these two operators are labelled by $N = 0, 1, \dots$ (the eigenvalue of N_{tot}) and, within each $(N+1)$ -dimensional subspace for a given N , by the index k that runs from 0 to N .

We find $|\phi_{N, k}\rangle$ and $E_{\text{AF}}(N, k)$ numerically. Figures 3.6(a) and (b) are plots of $E_{\text{AF}}(N, k)$ and ξ_{SVNE} versus g for $N = 4$ and $k = 0, 1, 2$ in the case $\omega_{\text{F}} = 1.5$, $\omega_{\text{A}} = 1$. Avoided crossings occur at $g = 0$, with a corresponding minimum in ξ_{SVNE} that drops down to zero for each of the three states $|\phi_{4, 0}\rangle$, $|\phi_{4, 1}\rangle$ and $|\phi_{4, 2}\rangle$. These states are therefore unentangled at $g = 0$, i.e., in the absence of interaction between the two modes of the bipartite system, as one might expect.

In order to examine what happens when there *is* a crossing of energy levels, we introduce a degeneracy by setting $\omega_{\text{F}} = \omega_{\text{A}}$. Figures 3.7 (a) and (b) are plots of $E_{\text{AF}}(N, k)$ and ξ_{SVNE} versus g for $N = 4$ and $k = 0, 1, 2$, with γ , ω_{A} and ω_{F} set equal to 1. Both a level crossing and an avoided crossing are seen to occur at $g = 0$, signalled by a minimum in ξ_{SVNE} for each of the three states concerned. The crossing of $E_{\text{AF}}(4, 0)$ and $E_{\text{AF}}(4, 1)$ arises as follows. Let $|p, 4-p\rangle$ denote the product state $|p\rangle_{\text{F}} \otimes |4-p\rangle$, where $|p\rangle_{\text{F}}$ is a photon number state of the field mode and $|4-p\rangle$ is an oscillator state of the atom mode. In the rest of this chapter, we drop the subscript F in the field

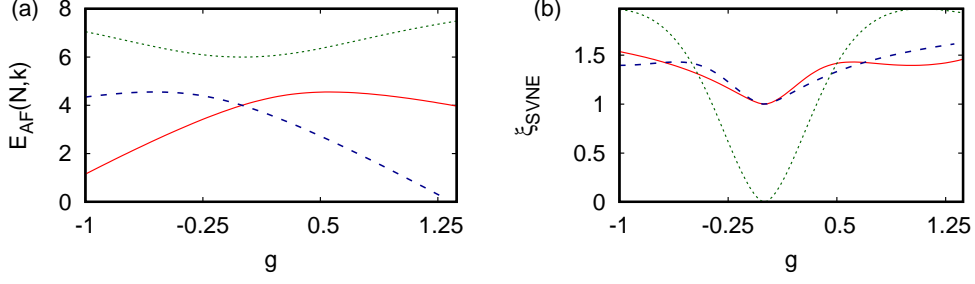


Figure 3.7: (a) $E_{AF}(N, k)$ and (b) ξ_{SVNE} vs. g for $N = 4$, $k = 0, 1, 2$ in the atom-field interaction model, in the degenerate case $\omega_F = \omega_A = 1$. The curves correspond to $k = 0$ (red), 1 (blue) and 2 (green). $\gamma = 1$.

state for ease of notation. When $\gamma = \omega_A = \omega_F = 1$ and $g = 0$, the Hamiltonian reduces to $a^\dagger a + (b^\dagger b)^2$. The energy levels $E_{AF}(4, 0)$ and $E_{AF}(4, 1)$ become degenerate at the value 4. The degeneracy occurs because the operator $|4, 0\rangle \langle 3, 1| + |3, 1\rangle \langle 4, 0|$ commutes with H_{AF} when $\omega_A = \omega_F$ and $g = 0$. Mixing of the states $|4, 0\rangle$ and $|3, 1\rangle$ occurs, and the corresponding energy eigenstates are given by the symmetric linear combination $|\phi_{4,0}\rangle = (|4, 0\rangle + |3, 1\rangle)/\sqrt{2}$ and the antisymmetric linear combination $|\phi_{4,1}\rangle = (|4, 0\rangle - |3, 1\rangle)/\sqrt{2}$. As the symmetries of the two states are different, the level crossing does not violate the von Neumann-Wigner no-crossing theorem. At the crossing, each of the states $|\phi_{4,0}\rangle$ and $|\phi_{4,1}\rangle$ remains a manifestly entangled state that is, in fact, a Bell state. This is why the corresponding ξ_{SVNE} does not vanish at that point, but merely dips to a local minimum with value 1, characteristic of a Bell state. It is interesting to note that the degeneracy that occurs when $\omega_F = \omega_A$ ensures entanglement even in the absence of any interaction between the two modes.

The level $E_{AF}(4, 2)$, on the other hand, is repelled and has the value 6 at $g = 0$. The corresponding eigenstate $|\phi_{4,2}\rangle$ becomes the unentangled product state $|2, 2\rangle$ at the avoided crossing, and ξ_{SVNE} drops to zero in this case, as expected.

In Fig. 3.8, we plot the correlation between various indicators and ξ_{SVNE} . For this purpose, 80 values of each of the ξ -indicators were calculated with g varied in the range $[-1, 1.4]$ in steps of 0.03. Treating these as sets of random numbers, we obtain the PCC between the various indicators and ξ_{SVNE} , as described in the foregoing. The performance of the entanglement indicators in this case is similar to that found in the BEC system. With increase in γ , the efficacy of all the indicators is marginally decreased.

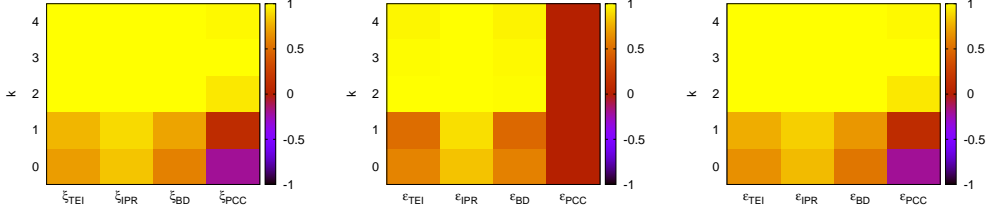


Figure 3.8: Correlation of ξ_{SVNE} with ξ -indicators (left), with ε -indicators for the slice $\theta_A = 0, \theta_B = \pi/2$ (centre), and with ε -indicators for the slice $\theta_A = 0, \theta_B = 0$ (right), for the eigenstates $|\phi_{4,k}\rangle$, $0 \leq k \leq 4$ in the atom-field interaction model. $\omega_F = \omega_A = \gamma = 1$.

3.4 Avoided crossings in multipartite HQ systems

3.4.1 The Tavis-Cummings model

As our third and final example, we consider hybrid quantum systems comprising several qubits interacting with an external field. These systems are described by the class of Tavis-Cummings models [65] in a variety of diverse physical situations which include inherent field nonlinearities and inter-qubit interactions. The model we consider below is generic, applicable to a system of several two-level atoms with nearest-neighbour couplings interacting with an external radiation field in the presence of a Kerr-like nonlinearity, or to a chain of M superconducting qubits interacting with a microwave field of frequency Ω_F . In the latter case, the model Hamiltonian (setting $\hbar = 1$) is given by [63, 64]

$$H_{\text{TC}} = \Omega_F a^\dagger a + \chi a^{\dagger 2} a^2 + \sum_{p=1}^M \Omega_p \sigma_{pz} + \Lambda (a^\dagger \sigma_p^- + a \sigma_p^+) + \sum_{p=1}^{M-1} \Lambda_s (\sigma_p^- \sigma_{(p+1)}^+ + \sigma_{(p+1)}^- \sigma_p^+). \quad (3.19)$$

Here, χ is the strength of the field nonlinearity, Λ is the coupling strength between the field and each of the M qubits, σ_p^\pm are the ladder operators of the p^{th} qubit, and Λ_s is the strength of the interaction between nearest-neighbour qubits. $\Omega_p = (\Delta_p^2 + \epsilon^2)^{1/2}$ is the energy difference between the two levels of the p^{th} qubit, where Δ_p is the inherent excitation gap and ϵ is the detuning of the external magnetic flux from the flux quantum $h/(2e)$. In our numerical computations we have used experimentally relevant parameter values [64], namely, $\Omega_F/(2\pi) = 7.78$ GHz and $\epsilon/(2\pi) = 4.62$ GHz. The level separations Δ_p of the individual qubits have been drawn from a Gaussian distribution with a

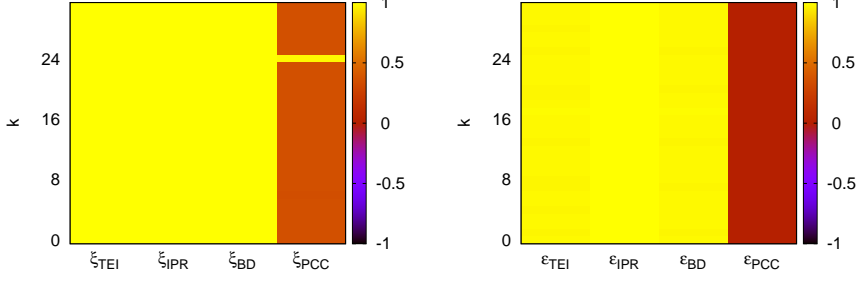


Figure 3.9: Correlation of ξ_{SVNE} with ξ -indicators (left) and with ε -indicators for the slice corresponding to $\theta = \pi/2$ for the field, and the σ_x basis for each qubit (right) for different values of Λ . The figures are for the eigenstates $|\psi_{5,6,k}\rangle$, $0 \leq k \leq 2^5 - 1$ in Case (i) in the Tavis-Cummings model.

mean given by $\langle \Delta \rangle / (2\pi) = 5.6$ GHz and a standard deviation $0.2 \langle \Delta \rangle$.

We have considered three cases, namely, (i) $\Lambda_s = \chi = 0$, (ii) $\Lambda_s / (2\pi) = 1$ MHz, $\chi = 0$ and (iii) $\Lambda_s / (2\pi) = \chi / (2\pi) = 1$ MHz. In each case, $\Lambda / (2\pi)$ is varied from -1.2 MHz to 1.3 MHz in steps of 0.025 MHz. It is easily shown that the total number operator

$$\mathcal{N}_{\text{tot}} = a^\dagger a + \sum_{p=1}^M \sigma_p^+ \sigma_p^-,$$

commutes with H_{TC} . For each value of Λ we have numerically solved for the complete set $\{|\psi_{M,N,k}\rangle\}$ of common eigenstates of \mathcal{N}_{tot} and H_{TC} , where $N = 0, 1, \dots$ is the eigenvalue of \mathcal{N}_{tot} and $k = 0, 1, \dots, 2^M - 1$. Considering the total system as a bipartite composition of the field subsystem and a subsystem comprising all the qubits, we have computed the entanglement indicators. Figure 3.9 shows the correlation between the indicators and ξ_{SVNE} in Case (i). The associated Pearson correlation coefficients are 0.97 for ε_{TEI} , 0.99 for ε_{IPR} , 0.97 for ε_{BD} , correct to two decimal places. (The accuracy of the ε -indicators depends, of course, on the basis chosen.) On averaging, we obtain the corresponding ξ -indicators with a PCC equal to 0.99 , showing that these indicators track ξ_{SVNE} very closely. We have carried out a similar exercise in Cases (ii) and (iii). The results and the inferences drawn from them are broadly similar to those found in Case (i).

Finally, with $\Lambda / (2\pi)$ set equal to 1.2 MHz, we have examined the effect of changing the strength of the disorder in Ω_p by varying the standard deviation of Δ_p from 0 to $0.2 \langle \Delta \rangle$ in steps of $2 \times 10^{-4} \langle \Delta \rangle$. Calculating the entanglement indicators for each disorder strength in Ω_p , we have found the correlations between the ξ -indicators and ξ_{SVNE} in Cases (i), (ii), and (iii). ξ_{TEI} and ξ_{BD} turn out to be significantly closer to ξ_{SVNE} ,

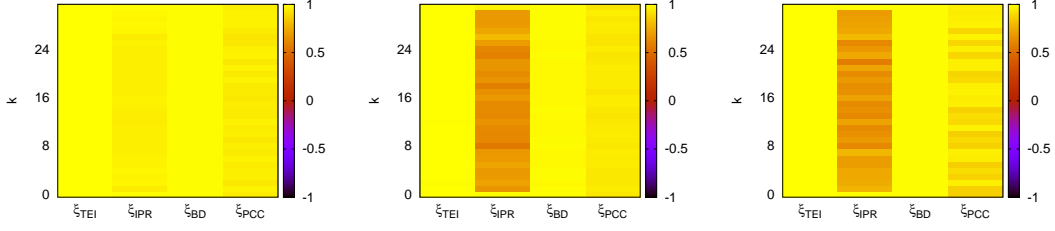


Figure 3.10: Correlation between ξ_{SVNE} and ξ -indicators for different values of disorder strength and eigenstates $|\zeta_{5,6,k}\rangle$ $0 \leq k \leq 2^5 - 1$. Left to right, Cases (i), (ii) and (iii) respectively in the Tavis-Cummings model.

and hence more accurate indicators of entanglement, than ξ_{IPR} and ξ_{PCC} (see Fig. 3.10).

3.5 Concluding remarks

In this chapter, we have considered generic bipartite continuous-variable systems and hybrid quantum systems in the presence of nonlinearities, and tested quantitatively the efficacy of various indicators in estimating entanglement directly from quantum state tomograms close to avoided energy-level crossings. We find that the nonlinear correlation between the respective quadratures of the two subsystems reflects very reliably the extent of entanglement in bipartite CV systems governed by number-conserving Hamiltonians. We have shown that if the eigenstates of the Hamiltonian are superpositions of Hamming-uncorrelated states, the inverse-participation-ratio-based quantifier ξ_{IPR} is an excellent indicator of entanglement near avoided crossings. In fact, even ε_{IPR} (the corresponding indicator for a single section of the tomogram) suffices to estimate entanglement reliably. The tomographic entanglement indicator ξ_{TEI} and the Bhattacharyya-distance-based indicator ξ_{BD} are also good indicators at avoided crossings, in contrast to the linear correlator ξ_{PCC} which is based on the Pearson correlation coefficient. Entanglement indicators seem to perform better with increasing $\langle N_{tot} \rangle$. The conclusions drawn are both significant and readily applicable in identifying optimal entanglement indicators that are easily obtained from tomograms, without employing state reconstruction procedures.

In the next chapter, we investigate the performance of some of these entanglement indicators during temporal evolution of bipartite CV systems.

CHAPTER 4

Assessment and comparison of entanglement indicators in continuous-variable systems

4.1 Introduction

In this chapter, we first examine the entanglement dynamics of bipartite CV systems. We have seen that ξ_{IPR} and ξ_{TEI} are good entanglement indicators close to avoided crossings. The entanglement indicators we consider here are ξ_{IPR} and ξ'_{TEI} . The latter is a modification of ξ_{TEI} . We will show in subsequent sections that it performs as well as ξ_{TEI} in the context of entanglement dynamics in CV systems. The performance of these two indicators are compared at specific instants with both ξ_{SVNE} and ξ_{SLE} . We recall that ξ_{SVNE} is given by $-\text{Tr}(\rho_i \log_2 \rho_i)$, and the subsystem linear entropy ξ_{SLE} is $1 - \text{Tr}(\rho_i^2)$ where ρ_i is the subsystem density matrix (i denotes subsystems A, B). These two indicators involve both off-diagonal and diagonal elements of the density matrix in any given basis. In contrast, the tomogram only provides information about the diagonal elements, although in several complete bases. It is therefore necessary to carry out a detailed comparative study between the tomographic indicators, on the one hand, and ξ_{SVNE} and ξ_{SLE} , on the other, in order to assess their efficacy and limitations.

The systems we consider for our purpose are a multi-level atom interacting with a radiation field [62], and the double-well BEC system [45], examined in Chapter 3, in a different context.

We emphasize that ξ'_{TEI} is not an entanglement *measure* in contrast to ξ_{SVNE} and ξ_{SLE} . Keeping this in mind, we have also obtained a long data set of the difference $d_1(t)$ between ξ_{SVNE} and ξ'_{TEI} at various instants of time, and carried out a detailed time-series analysis for several initial states and for different strengths of nonlinearity. The ergodicity properties of $d_1(t)$ carry information on the performance of ξ'_{TEI} .

In a recent experiment reported in the literature [28], photon coincidence counts were used to distinguish between two 2-photon states in a CV bipartite system. Here we

have demonstrated that by computing ε_{TEI} (defined in Eq. (3.3)) from the tomograms corresponding to the two states, we can easily distinguish between them. Through this calculation we have extended our study to chronocyclic tomograms, which are explained in detail in Section 4.5.

The plan of this chapter is as follows. In Section 4.2, we outline the procedure for obtaining ξ'_{TEI} from ε_{TEI} . In Section 4.3, we compare ξ_{IPR} and ξ'_{TEI} with ξ_{SVNE} and ξ_{SLE} during dynamical evolution of both the double-well BEC system and the multi-level atom interacting with the radiation field. Section 4.4 is devoted to the time-series analysis. In Section 4.5, we briefly review the salient features of chronocyclic tomograms, and demonstrate the usefulness of the tomographic indicator in distinguishing between two entangled states. We conclude with brief remarks.

4.2 ξ -indicators and averaging procedures

The generalised eigenstates of conjugate pairs of quadrature operators constitute a pair of mutually unbiased bases [75], as

$$|\langle X_\theta, \theta | X'_{\theta+\pi/2}, \theta + \pi/2 \rangle| = 1/\sqrt{2\pi\hbar} > 0. \quad (4.1)$$

We recall that the specific averaging procedure used to obtain any ξ -indicator mentioned in Section 3.2 involves calculating the corresponding ε -indicator in several sets of mutually unbiased bases. ξ'_{TEI} is obtained by averaging *only* over the dominant values of $\varepsilon_{\text{TEI}}(\theta_A, \theta_B)$. Here we have averaged over 100 values of $\varepsilon_{\text{TEI}}(\theta_A, \theta_B)$ to obtain ξ_{TEI} . ξ'_{TEI} is calculated only using those values that exceed the mean by one standard deviation. For this purpose we have numerically generated several histograms of $\varepsilon_{\text{TEI}}(\theta_A, \theta_B)$ for both the atom-field interaction and the double-well BEC models. For a given initial state, the system is unitarily evolved in time, and each histogram corresponds to a specific instant of time. A typical histogram is presented in Fig. 4.1. The average of $\varepsilon_{\text{TEI}}(\theta_A, \theta_B)$ over *all* the values in the histogram in Fig. 4.1 has been compared with that obtained by averaging only over the contribution from the shaded portion. The qualitative features were found to be essentially the same in both cases in all the histograms considered. The results in the following sections are therefore based on the latter averaging procedure, since it is clearly computationally less intensive. We denote the entanglement indicator

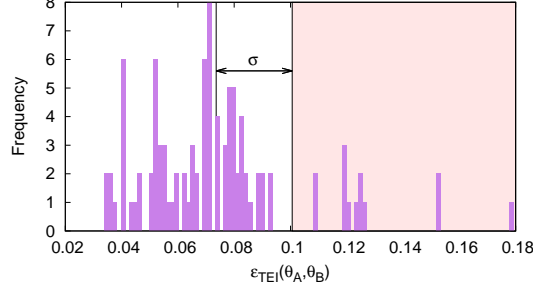


Figure 4.1: Histogram of $\varepsilon_{\text{TEI}}(\theta_A, \theta_B)$ from 100 combinations of θ_A and θ_B . The shaded area marks the values of $\varepsilon_{\text{TEI}}(\theta_A, \theta_B)$ that exceed the mean value ~ 0.07 by one standard deviation.

thus obtained by ξ'_{TEI} , and in subsequent sections compare ξ'_{TEI} with ξ_{SLE} and ξ_{IPR} .

4.3 Entanglement indicators in generic bipartite models

In this section, we examine in detail the performance of ξ'_{TEI} in the atom-field interaction model [62] and the double-well BEC model [45]. We consider initial states of the total bipartite system that are pure states governed by unitary evolution.

4.3.1 Atom-field interaction model

The effective Hamiltonian (Eq. (3.18)), setting $\hbar = 1$, is [62]

$$H_{\text{AF}} = \omega_{\text{F}} a^\dagger a + \omega_{\text{A}} b^\dagger b + \gamma b^{\dagger 2} b^2 + g(a^\dagger b + ab^\dagger).$$

We recall that (a, a^\dagger) are photon annihilation and creation operators. The multi-level atom is modelled as an oscillator with harmonic frequency ω_{A} and ladder operators (b, b^\dagger) . The anharmonicity of the oscillator is effectively described by the Kerr-like term in H_{AF} with strength γ . A variety of initial states of the total system has been judiciously selected in order to explore the range of possible nonclassical effects during time evolution. The *unentangled* initial states considered correspond to the atom in its ground state $|0\rangle$ and the field in either a CS (e.g., $|\alpha\rangle_{\text{F}}$), or an m -PACS (e.g., $|\alpha, m\rangle_{\text{F}}$). We also consider two *entangled* initial states, namely, the binomial state $|\psi_{\text{bin}}\rangle$ (Eq. (1.5)) and the two-mode squeezed state $|\zeta\rangle$ (Eq. (1.6)). We recall that the binomial state

$|\psi_{\text{bin}}\rangle$, for a non-negative integer N , is given by

$$|\psi_{\text{bin}}\rangle = 2^{-N/2} \sum_{n=0}^N \binom{N}{n}^{1/2} |N-n, n\rangle,$$

where $|N-n, n\rangle \equiv |N-n\rangle_{\text{F}} \otimes |n\rangle$, the product state corresponding to the field and the atom in the respective number states $|N-n\rangle$ and $|n\rangle$. Also, $|\zeta\rangle = e^{\zeta^* a b - \zeta a^\dagger b^\dagger} |0, 0\rangle$, ($\zeta \in \mathbb{C}$) and $|0, 0\rangle$ is the product state corresponding to $N = 0, n = 0$.

Corresponding to these initial states we have numerically generated tomograms at approximately 2000 instants, separated by a time step $0.2 \pi/g$ as the system evolves. From these, we have obtained ξ'_{TEI} and the differences

$$d_1(t) = |\xi_{\text{SVNE}} - \xi'_{\text{TEI}}|, \quad d_2(t) = |\xi_{\text{SLE}} - \xi'_{\text{TEI}}|. \quad (4.2)$$

These differences are plotted against the scaled time gt/π for an initial two-mode squeezed state (Fig. 4.2(a)), and for a factored product of a CS and atomic ground state $|0\rangle$ (Fig. 4.2(b)). From these plots it is evident that ξ'_{TEI} is in much better agreement with ξ_{SLE} than with ξ_{SVNE} over the time interval considered, independent of the parameter values and the nature of the initial state. We therefore choose ξ_{SLE} as the reference entanglement indicator. Next, we compare $d_2(t)$ with the difference

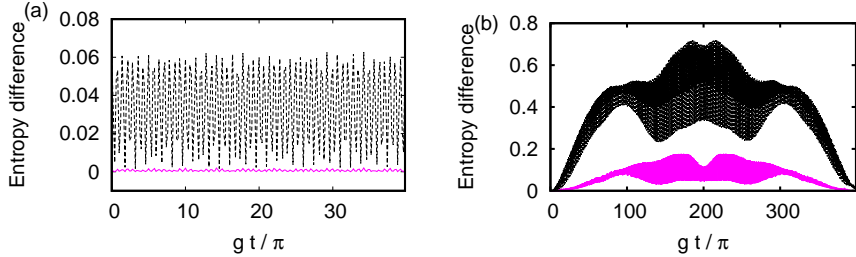


Figure 4.2: $d_1(t)$ (black) and $d_2(t)$ (pink) vs. scaled time gt/π , for $\omega_{\text{F}} = \omega_{\text{A}} = \gamma = 1$ in the atom-field interaction model. (a) $g = 0.2$, initial two-mode squeezed state $|\zeta\rangle$, $\zeta = 0.1$ (b) $g = 100$, initial state $|\alpha\rangle_{\text{F}} \otimes |0\rangle$, $|\alpha|^2 = 1$.

$$\Delta(t) = |\xi_{\text{SVNE}} - \xi_{\text{SLE}}|. \quad (4.3)$$

We have verified that in all the cases considered, $\Delta(t) > d_2(t)$ (see, for instance, Fig. 4.3). In what follows, we therefore focus only on $d_2(t)$ and the difference

$$d_3(t) = |\xi_{\text{SLE}} - \xi_{\text{IPR}}|. \quad (4.4)$$

This comparison brings out interesting features of both the indicators. When the strength of the nonlinearity is low relative to that of the coupling (e.g., $\gamma/g = 0.01$), it is known [76] that full and fractional revivals occur, and entanglement measures may be expected to display signatures of these revival phenomena. From Fig. 4.4 (a) we see that at the revival time $gT_{\text{rev}}/\pi = 400$, ξ'_{TEI} agrees with ξ_{SLE} much more closely than ξ_{IPR} does. Further, over the entire time interval $(0, T_{\text{rev}})$, $d_2(t)$ is significantly smaller than $d_3(t)$. This feature holds even for larger values of the ratio γ/g , as can be seen from Fig. 4.4 (b). ξ'_{TEI} is therefore favoured over ξ_{IPR} as an entanglement indicator. The time evolution of the difference $d_2(t)$ is drastically different from that of $d_3(t)$ for initial field states that depart from ideal coherence. In this case, over the entire time considered, ξ_{IPR} performs significantly better than ξ'_{TEI} for small values of γ/g (Fig. 4.4 (c)). As the value of γ/g is increased the two indicators have essentially the same behaviour (Fig. 4.4 (d)).

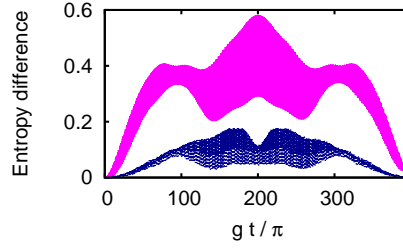


Figure 4.3: $d_2(t)$ (blue) and $\Delta(t)$ (pink) vs. scaled time gt/π , with $\omega_F = \omega_A = \gamma = 1$, $g = 100$ in the atom-field interaction model. Initial state $|\alpha\rangle_F \otimes |0\rangle$, $|\alpha|^2 = 1$.

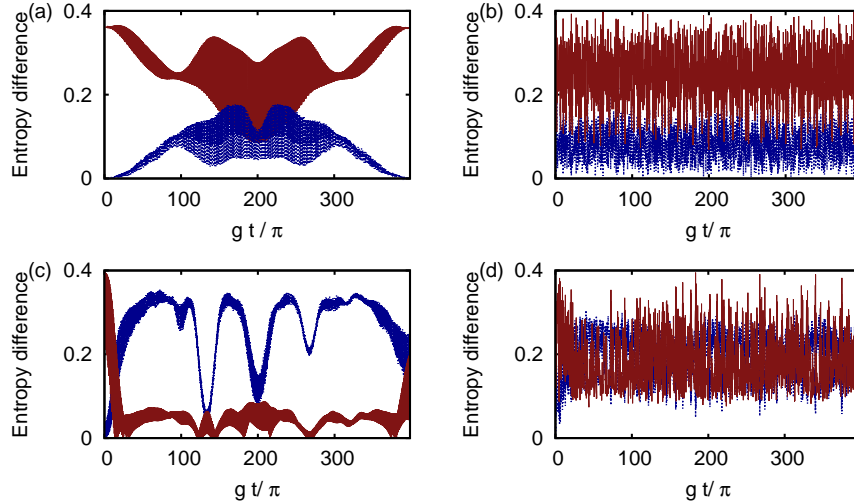


Figure 4.4: $d_2(t)$ (blue) and $d_3(t)$ (brown) vs. scaled time gt/π , for $\omega_F = \omega_A = \gamma = |\alpha|^2 = 1$ in the atom-field interaction model. (a) and (b): Initial state $|\alpha\rangle_F \otimes |0\rangle$, $g = 100$ and 0.2 respectively. (c) and (d): Initial state $|\alpha, 5\rangle_F \otimes |0\rangle$, $g = 100$ and 0.2 respectively.

We turn now to entangled initial states. In the case of the two-mode squeezed state

$|\zeta\rangle$, we see from Figs. 4.5 (a) and (b) that ξ'_{TEI} fares much better than ξ_{IPR} over the entire time interval considered, for small values of ζ . With an increase in the value of ζ , both the indicators show comparable departures from ξ_{SLE} .

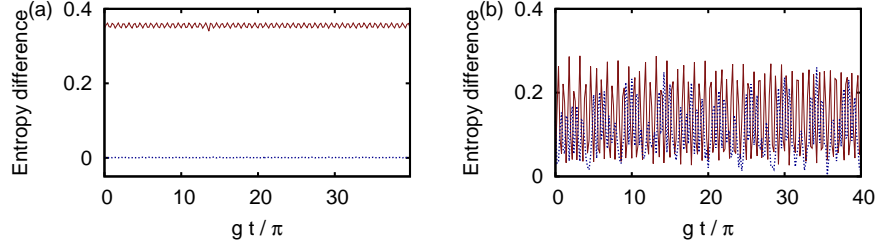


Figure 4.5: $d_2(t)$ (blue) and $d_3(t)$ (brown) vs. scaled time gt/π , for $\omega_F = \omega_A = \gamma = 1, g = 0.2$ in the atom-field interaction model. Initial two-mode squeezed state $|\zeta\rangle$, (a) $\zeta = 0.1$ and (b) $\zeta = 0.7$.

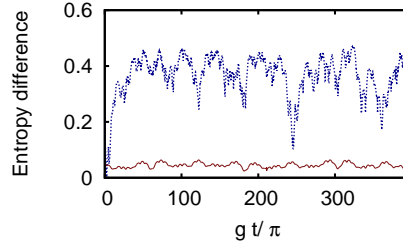


Figure 4.6: $d_2(t)$ (blue) and $d_3(t)$ (brown) vs. scaled time gt/π , for $\omega_F = \omega_A = \gamma = 1, g = 0.2$ in the atom-field interaction model. Initial state $|\psi_{\text{bin}}\rangle$ with $N = 10$.

In the case of an initial binomial state, on the other hand, ξ_{IPR} fares significantly better than ξ'_{TEI} . This can be understood by examining the Hamming distance between the basis states constituting the binomial state. We define this distance in the context of continuous variables by extrapolating the idea of Hamming distance for qudits as explained in Section 3.3. As pointed out before, the efficacy of ξ_{IPR} as an entanglement indicator increases with an increase in the Hamming distance. This indicator is therefore especially useful for superpositions of states that are Hamming-uncorrelated (i.e., separated by a Hamming distance equal to 2 in bipartite states) both in the context of spin systems [66, 77] and CV systems [36, 35].

In the atom-field interaction model considered here, both the subsystems are infinite-dimensional. We now examine whether the efficacy of ξ_{IPR} is correlated with the Hamming distance in this case as well. We note that $|\psi_{\text{bin}}\rangle$ can be expanded as a superposition of states which are Hamming-uncorrelated. From Fig. 4.6, we see that in this case also ξ_{IPR} is a significantly better entanglement indicator than ξ'_{TEI} .

4.3.2 The double-well BEC model

The effective Hamiltonian (Eq. (2.21)) for the system, setting $\hbar = 1$, is given by [45]

$$H_{\text{BEC}} = \omega_0 N_{\text{tot}} + \omega_1 (a^\dagger a - b^\dagger b) + U N_{\text{tot}}^2 - \lambda (a^\dagger b + ab^\dagger).$$

We recall that $N_{\text{tot}} = a^\dagger a + b^\dagger b$. Here (a, a^\dagger) and (b, b^\dagger) are the boson annihilation and creation operators of the atoms in wells A and B respectively. U is the strength of the nonlinearity (both in the individual modes as well as in their interaction), λ is the linear interaction strength, and ω_0, ω_1 are constants. As in the previous instance, we select a representative variety of initial states: (i) the unentangled direct product $|\alpha_a, m_1\rangle \otimes |\alpha_b, m_2\rangle$ of boson-added coherent states of atoms in the wells A and B respectively, where $\alpha_a, \alpha_b \in \mathbb{C}$; (ii) the binomial state $|\psi_{\text{bin}}\rangle$ (Eq. (1.5)), and (iii) the two-mode squeezed vacuum state $|\zeta\rangle$ (Eq. (1.6)), with the understanding that the basis states are now product states of the species in the two wells.

In each of these cases, we must first obtain the state of the system at any time $t \geq 0$ as it evolves under the Hamiltonian H_{BEC} . It turns out that, in the case of an initial state of type (i) above, the state of the system can be calculated explicitly as a function of t , as outlined in Appendix C. In Cases (ii) and (iii), the state vector at time t is computed numerically. Using these, we have generated tomograms at approximately 1000 instants, separated by a time step $0.001 \pi/U$. We have verified that, in this model also ξ'_{TEI} agrees better with ξ_{SLE} than with ξ_{SVNE} , and that the difference between ξ'_{TEI} and ξ_{SLE} is smaller than that between ξ_{SVNE} and ξ_{SLE} . In what follows, we have therefore chosen ξ_{SLE} as the reference entanglement measure and compared $d_2(t)$ with $d_3(t)$.

It is evident that the relevant ratio for characterising the dynamics is U/λ_1 where $\lambda_1 = (\omega_1^2 + \lambda^2)^{1/2}$. A representative example of the temporal behaviour of $d_2(t)$ and $d_3(t)$ is shown in Fig. 4.7. The effect of increasing U/λ_1 can be seen by comparing Figs. 4.7 (a) and (b), while that of departure from coherence of the initial state can be seen by comparing (a) and (c). We have also carried out analogous studies in the case of entangled initial states $|\psi_{\text{bin}}\rangle$ and $|\zeta\rangle$. The general trends in the behaviour of the entanglement indicators in these cases are consistent with, and corroborate, those found in the atom-field interaction model (see Fig. 4.8).

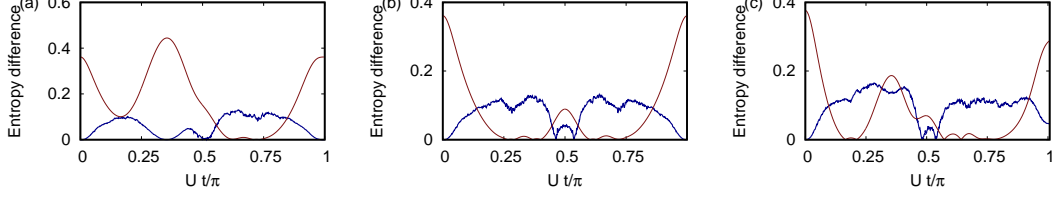


Figure 4.7: $d_2(t)$ (blue) and $d_3(t)$ (brown) vs. scaled time Ut/π , for $\omega_0 = U = |\alpha|^2 = 1$ in the BEC model. (a) $\omega_1 = \lambda = 1$, initial state $|\alpha\rangle \otimes |\alpha\rangle$; (b) $\omega_1 = \lambda = 0.1$, initial state $|\alpha\rangle \otimes |\alpha\rangle$; (c) $\omega_1 = \lambda = 1$, initial state $|\alpha, 1\rangle \otimes |\alpha\rangle$.

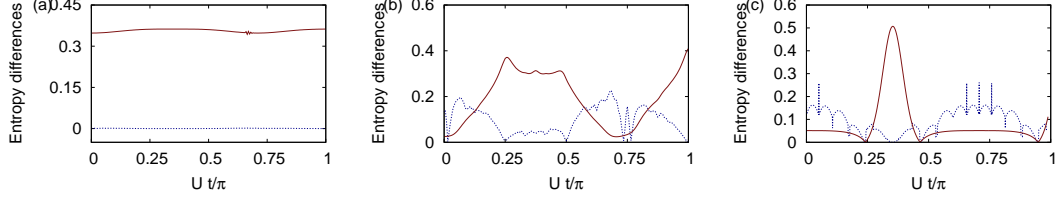


Figure 4.8: $d_2(t)$ (blue) and $d_3(t)$ (brown) vs. scaled time Ut/π , for $\omega_0 = U = \omega_1 = \lambda = 1$ in the BEC model. (a) and (b): Initial state $|\zeta\rangle$, $\zeta = 0.1$ and 0.7 respectively. (c) Initial state $|\psi_{\text{bin}}\rangle$, $N = 10$.

Decoherence effects in the double-well BEC model

Since decoherence is an important issue in experiments, we now investigate this aspect for an initial state $|\alpha_a\rangle \otimes |\alpha_b\rangle$, where $\alpha_a = \sqrt{0.001}$ and $\alpha_b = 1$: since α_a is sufficiently small in magnitude, $|\alpha_a\rangle$ can be approximated by a superposition of a zero-boson and one-boson states, whereas $|\alpha_b\rangle$ is an infinite superposition of the boson number states. The states get entangled during unitary evolution. We consider the entangled state of the system at any instant, say $Ut = \pi/2$, and apply damping to subsystem A alone for a time interval τ . This toy example suffices to examine the extent to which an efficient entanglement indicator can be extracted from tomograms, when the system decoheres. We have set U , ω_0 , ω_1 and λ equal to 1, for numerical computation. Decoherence takes place through amplitude damping and phase damping [43].

We recall from Chapter 2 that the master equation for amplitude decay (Eq. (2.14)) is given by

$$\frac{d\rho}{d\tau} = -\Gamma(a^\dagger a \rho - 2a\rho a^\dagger + \rho a^\dagger a).$$

Here, Γ is the rate of loss and τ the time parameter is reckoned from the instant $Ut = \pi/2$. The solution to this master equation is [43]

$$\rho(\tau) = \sum_{n,m,n',m'=0}^{\infty} \rho_{n,m,n',m'}(\tau) |n, m\rangle \langle n', m'|, \quad (4.5)$$

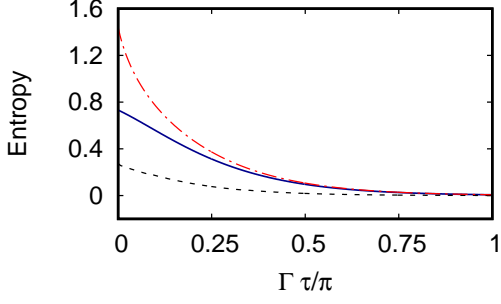


Figure 4.9: ξ'_{TEI} (black), $\xi_{\text{SVNE}}^{(\text{A})}$ (blue) and ξ_{QMI} (red) vs. $\Gamma\tau/\pi$ for amplitude decay with $\Gamma = 0.001$ in the BEC model.

where

$$\rho_{n,m,n',m'}(\tau) = e^{-\Gamma\tau(n+n')} \sum_{r=0}^{\infty} \sqrt{\binom{n+r}{r} \binom{n'+r}{r}} (1 - e^{-2\Gamma\tau})^r \rho_{n+r,m,n'+r,m'}(\tau=0).$$

Note that $\rho(\tau=0)$ is chosen to be $|\Psi_{00}(\pi/2U)\rangle \langle \Psi_{00}(\pi/2U)|$. (The expression for $|\Psi_{00}(t)\rangle$ as a function of time t is given by Eq. (2.22)).

As the bipartite state is a mixed state owing to decoherence, ξ_{SVNE} corresponding to subsystems A and B are not equal to each other and are now denoted by $\xi_{\text{SVNE}}^{(\text{A})}$ and $\xi_{\text{SVNE}}^{(\text{B})}$, respectively. The entropy of the full system is denoted by $\xi_{\text{SVNE}}^{(\text{AB})}$. The quantum mutual information

$$\xi_{\text{QMI}} = \xi_{\text{SVNE}}^{(\text{A})} + \xi_{\text{SVNE}}^{(\text{B})} - \xi_{\text{SVNE}}^{(\text{AB})}, \quad (4.6)$$

is of immediate interest. At each instant τ , ξ'_{TEI} , $\xi_{\text{SVNE}}^{(\text{A})}$ and ξ_{QMI} have been calculated numerically. Since the subsystem entropies are not equal, we expect that (if the tomogram captures decoherence effects well) ξ'_{TEI} must match ξ_{QMI} during dynamics. This is indeed borne out in Fig. 4.9, where ξ'_{TEI} , ξ_{QMI} and $\xi_{\text{SVNE}}^{(\text{A})}$ are compared. We point out that for a bipartite pure state, in the absence of decoherence $\xi_{\text{QMI}} = 2 \xi_{\text{SVNE}}^{(\text{A})} = 2 \xi_{\text{SVNE}}^{(\text{B})}$, and both $\xi_{\text{SVNE}}^{(\text{A})}$ and $\xi_{\text{SVNE}}^{(\text{B})}$ are denoted by ξ_{SVNE} .

Phase damping in A is modelled by (Eq. (2.17)) [43]

$$\frac{d\bar{\rho}}{d\tau} = -\Gamma_p((a^\dagger a)^2 \bar{\rho} - 2a^\dagger a \bar{\rho} a^\dagger a + \bar{\rho} (a^\dagger a)^2),$$

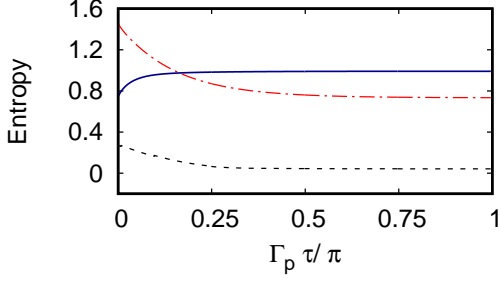


Figure 4.10: ξ'_{TEI} (black), $\xi_{\text{SVNE}}^{(\text{A})}$ (blue) and ξ_{QMI} (red) vs. $\Gamma_p \tau / \pi$ for phase damping with $\Gamma_p = 0.001$ in the BEC model.

where Γ_p is the rate of decoherence. The solution is of the form given in Eq. (4.5), with

$$\bar{\rho}_{n,m,n',m'}(\tau) = e^{-\Gamma_p \tau (n-n')^2} \bar{\rho}_{n,m,n',m'}(\tau = 0).$$

As before, ξ'_{TEI} mimics ξ_{QMI} reasonably well (Fig. 4.10).

4.4 Time-series analysis of $d_1(t)$

Finally, we turn to an assessment of the *long-time* behaviour of ξ'_{TEI} by means of a detailed time-series analysis.

As we have shown in the foregoing, the deviation of ξ'_{TEI} from ξ_{SVNE} is much more pronounced than its deviation from ξ_{SLE} . It is therefore appropriate to investigate how an initial difference between ξ'_{TEI} and ξ_{SVNE} changes with time. With this in mind, a time series of $d_1(t)$ has been obtained for both models considered in this chapter, and used to compute local Lyapunov exponents along the lines customary [78–80] in the study of dynamical systems. This involves reconstruction of the effective phase space, estimation of the minimum embedding dimension d_{emb} of this space, and calculation of the exponents themselves. The procedure used is outlined below.

The time series had 20000 data points. The effective phase space was reconstructed using the TISEAN package [81]. 100 different initial values $d_1(0)$ were randomly chosen in this phase space. The maximum local Lyapunov exponent corresponding to each $d_1(0)$ was computed over the same time interval L . (The term ‘local’ refers to the fact that L is much smaller than the time interval over which the maximum Lyapunov exponent Λ_∞ is obtained in the standard method). The average value Λ_L of these

100 maximum local Lyapunov exponents was obtained following the prescription in [80] (see Appendix D). This procedure was repeated for as many as 14 different values of L . Further, in each case it was verified that, with an increase in L , Λ_L tends to $\Lambda_\infty + (m/L^q)$, where m and q are constants [80]. We note that two neighbouring initial values of the dynamical variable of interest $d_1(t)$ diverges exponentially with Λ_L , in L steps. For completeness, we also present the power spectra corresponding to the various time series. We would expect a broadband spectrum for chaotic data. On the other hand, a ‘spiky’ power spectrum (i.e., a cluster of clearly defined sharp peaks in the power spectrum) points to a possible quasi-periodic behaviour. The results are presented below.

4.4.1 Atom-field interaction model

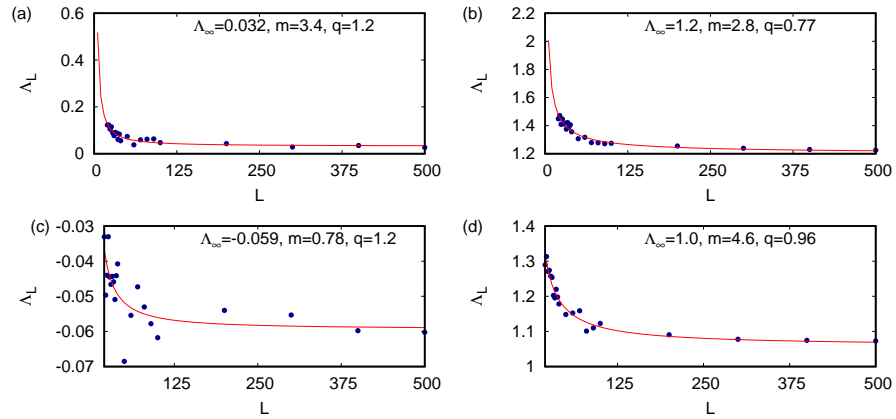


Figure 4.11: Λ_L obtained from the time series of $d_1(t)$ (blue) and the fit $\Lambda_\infty + (m/L^q)$ (red) vs. L , for $\omega_F = \omega_A = \gamma = 1$ in the atom-field interaction model. Initial state $|\alpha\rangle_F \otimes |0\rangle$: (a) $g = 100, |\alpha|^2 = 1$ (b) $g = 100, |\alpha|^2 = 5$ (c) $g = 0.2, |\alpha|^2 = 1$. (d) Initial state $|\alpha, 5\rangle_F \otimes |0\rangle, g = 100, |\alpha|^2 = 1$.

The difference $d_1(t)$ has been obtained at each instant with time step $\delta t = 0.1$ for 20000 time steps, and the effective phase space has been reconstructed. We see that for both the initial states $|\alpha\rangle_F \otimes |0\rangle$ and $|\alpha, 5\rangle_F \otimes |0\rangle$ with $|\alpha|^2 = 1$ and weak nonlinearity ($\gamma/g = 0.01$), Λ_L is positive, and both Λ_L and Λ_∞ are larger for the second initial state (compare Figs. 4.11 (a) and (d)). Λ_∞ increases with an increase in $|\alpha|^2$ for the initial state $|\alpha\rangle \otimes |0\rangle$ (compare Figs. 4.11 (a) and (b)). In contrast, for strong nonlinearity (e.g., as in Fig. 4.11 (c), $\gamma/g = 5$), Λ_L is negative.

For completeness, we present the power spectrum $PS(f)$ of the time series as a function of the frequency f in units of g , for each of the cases corresponding to Figs.

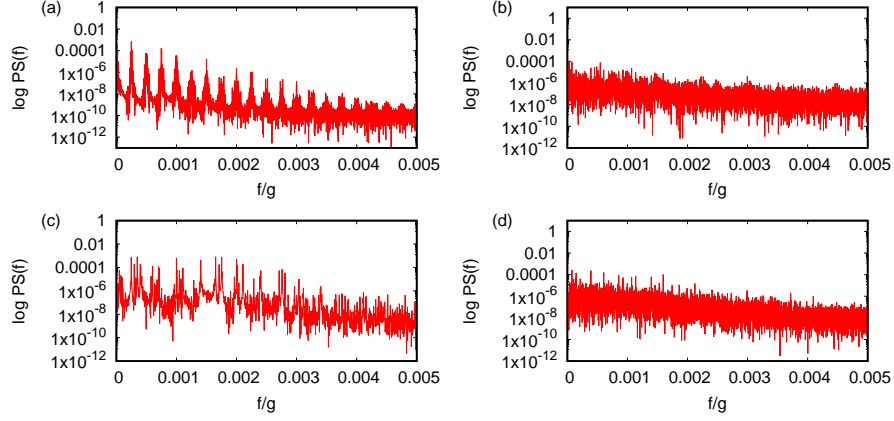


Figure 4.12: Logarithm of $PS(f)$ vs. f/g (red) in the atom-field interaction model, corresponding to the initial states and parameter values in Figs. 4.11 (a)–(d) respectively.

4.12 (a) to (d). The nearly quasi-harmonic power spectrum for weak nonlinearity (Fig. 4.12 (a)) changes into a broadband spectrum with increasing $|\alpha|^2$ (Fig. 4.12 (b)), while it loses its quasi-harmonicity without becoming a broadband spectrum with increasing nonlinearity (Fig. 4.12 (c)). The lack of coherence in the initial state makes the power spectrum broadband (Fig. 4.12 (d)). When a power spectrum exhibits regular or quasi-regular spikes at different frequencies, it signals quasiperiodicity in the processes generating the time series. A broadband spectrum, on the other hand, is an indicator of non-periodic (including chaotic) time evolution. When the power spectrum of this time series shows quasiperiodic behaviour (Figs. 4.12 (a) and (c)) in the sense above, we see that the local Lyapunov exponent is either negative, or small positive. The two entanglement indicators (namely, ξ'_{TEI} and ξ_{SVNE}) therefore do not diverge from each other in any significant way. We regard this as a broad corroboration of the validity of ξ'_{TEI} as an entanglement indicator. In contrast, when the power spectrum is markedly broadband (Figs. 4.12 (b) and (d)), the local Lyapunov exponent is distinctly positive, showing that ξ'_{TEI} diverges significantly from ξ_{SVNE} . Hence we conclude that ξ'_{TEI} is not a reliable or satisfactory indicator of entanglement for sufficiently large $|\alpha|^2$ or for initial PACS states with significant departure from coherence.

4.4.2 The double-well BEC model

As in the foregoing, we generate the time series of $d_1(t)$ by calculating this difference for 20000 time steps, in this case with $\delta t = 0.01$. As seen in Figs. 4.13 (a)–(c), in this

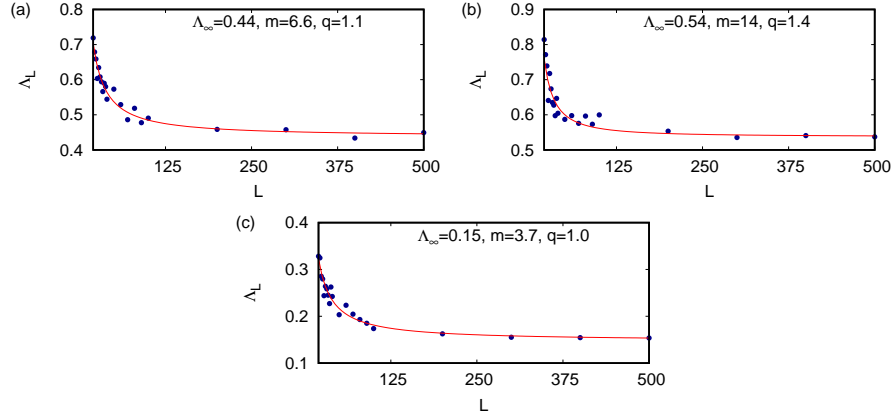


Figure 4.13: Λ_L obtained from the time series of $d_1(t)$ (blue) and the fit $\Lambda_\infty + (m/L^q)$ (red) vs. L , for $\omega_0 = \omega_1 = |\alpha| = 1$ in the BEC model. Initial state $|\alpha, 1\rangle \otimes |\alpha\rangle$ and (a) hopping frequency $\lambda = 5$, $U = 0.5$ (b) $\lambda = U = 1$. (c) Initial state $|\alpha, 5\rangle \otimes |\alpha, 5\rangle$, $\lambda = U = 1$.

instance Λ_L is positive regardless of the degree of coherence of the initial states of the subsystems, for a wide range of values of the ratio U/λ_1 ($\lambda_1 = (\lambda^2 + \omega_1^2)^{1/2}$). With an increase in U/λ_1 , Λ_∞ increases (Figs. 4.13 (a), (b)). In contrast to the atom-field interaction model, a departure of the initial state from perfect coherence causes Λ_∞ to decrease (Figs. 4.13 (a), (c)).

The power spectra corresponding to the three cases in Fig. 4.13 are shown in Fig. 4.14. When the linear part of H_{BEC} is dominant (λ_1 dominates over U , Fig. 4.14 (a)), $PS(f)$ reflects a degree of quasiperiodicity in the time series. When U becomes comparable to λ_1 , however, the nonlinearity in the Hamiltonian takes over, and $PS(f)$ is a broadband spectrum (Figs. 4.14 (b), (c)).

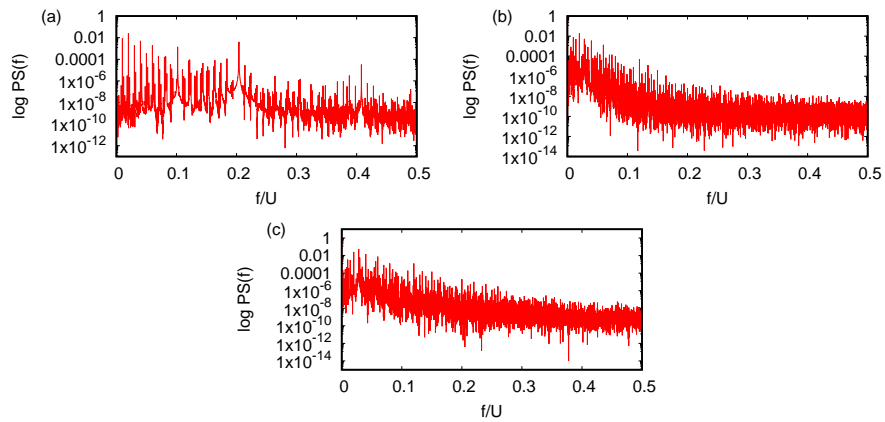


Figure 4.14: Logarithm of $PS(f)$ vs. f/U (red) in the BEC model, corresponding to the initial states and parameter values in Figs. 4.13 (a)–(c) respectively.

4.5 Tomographic signatures in a 2-photon bipartite system

As a further illustration of the use of the tomographic entanglement indicators, we now assess the performance of ε_{TEI} which we recall, is an indicator obtained from an appropriately chosen slice of the tomogram. We consider a CV bipartite system that has very recently been studied experimentally [28], and hence is of particular interest in the present context. One of the aims of the experiment was to analyse GKP-like states (Gottesman-Kitaev-Preskill-like states [82] where the ‘qubit’ is encoded in a CV basis, and on which error correction can be implemented with logic gate operations). What is of relevance to us in this context is the distinguishability of the two 2-photon states. We will show that the indicator ε_{TEI} does so unambiguously.

Some background information is in order. The analogy between an ultrashort light pulse and a quantum mechanical wave function leads [29] to a *chronocyclic* representation for the study of ultrashort pulses, where the time t and frequency ω are the conjugate observables. The state of a single photon of frequency ω is denoted in a spectral representation of infinitely narrow-band pulses by $|\omega\rangle$. The superposed state of a photon that has a frequency ω with a probability amplitude $\mathcal{S}(\omega)$ is given by $\int d\omega \mathcal{S}(\omega) |\omega\rangle$. In an equivalent temporal representation of infinitely short-duration pulses $\{|t\rangle\}$, this 1-photon state is $\int dt \tilde{\mathcal{S}}(t) |t\rangle$, where $\tilde{\mathcal{S}}(t)$ is the Fourier transform of $\mathcal{S}(\omega)$. A family of rotated observables $(\omega \cos \theta + t \sin \theta)$ can then be defined [83], where ω and t have been scaled by a natural time scale of the system to make them dimensionless. Measurements of these rotated observables form the basis of chronocyclic tomography, in which the set of histograms corresponding to these observables gives the tomogram of the state of a 1-photon system. In this chronocyclic representation, a 1-photon state can also be described in the time-frequency ‘phase space’ by a corresponding Wigner function [29]. Extension to multipartite states corresponding to two or more photons is straightforward. For instance, two photons of frequencies ω and ω' are given by the 2-photon CV bipartite state $|\omega\rangle \otimes |\omega'\rangle$.

The experiment [28] used a 2-photon CV bipartite system to generate a pair of distinguishable states that are frequency combs comprising finite-width peaks. Despite the finite width, the pair of 2-photon states concerned were shown to be clearly distin-

guishable experimentally. The measured photon coincidence counts were shown to be very different for the two states. Our objective here is to use chronocyclic tomograms to compute the indicator ε_{TEI} and to show that it can also be useful, in principle, to distinguish between these 2-photon states.

We denote by $|\Psi_\alpha\rangle$ and $|\Psi_\beta\rangle$ these two 2-photon states. In the experiment, they were generated in a setup comprising a cavity with resonant frequency $\bar{\omega}$, a photon source using parametric down conversion, and with input photons of frequency ω_p . If ω_s and ω_i denote the signal and idler frequencies, respectively, and Ω is their difference, the first of the two states is given by

$$|\Psi_\alpha\rangle = \mathcal{N}_\alpha^{-1/2} \int d\omega_s \int d\omega_i f_+(\omega_s + \omega_i) f_-(\Omega) \times f_{\text{cav}}(\omega_s) f_{\text{cav}}(\omega_i) |\omega_s\rangle \otimes |\omega_i\rangle. \quad (4.7)$$

Here,

$$f_-(\Omega) = e^{-(\Omega - \Omega_0)^2 / 4(\Delta\Omega)^2}, \quad (4.8)$$

where Ω_0 and $\Delta\Omega$ are the mean and standard deviation of Ω . f_{cav} is the Gaussian comb

$$f_{\text{cav}}(\omega) = \sum_n e^{-(\omega - n\bar{\omega})^2 / 2(\Delta\omega)^2} \quad (4.9)$$

where $\Delta\omega$ is the standard deviation of each Gaussian, \mathcal{N}_α is the normalisation constant, and $f_+(\omega_s + \omega_i) = \delta(\omega_p - \omega_s - \omega_i)$. We note that Eq. (4.7) features the product $f_{\text{cav}}(\omega_s) f_{\text{cav}}(\omega_i)$, where $f_{\text{cav}}(\omega)$ is a superposition of Gaussians corresponding to odd and even values of n such that the two are in phase with each other.

The second 2-photon state is given by

$$|\Psi_\beta\rangle = \mathcal{N}_\beta^{-1/2} \int d\omega_s \int d\omega_i f_+(\omega_s + \omega_i) f_-(\Omega) \times g_{\text{cav}}(\omega_s) f_{\text{cav}}(\omega_i) |\omega_s\rangle \otimes |\omega_i\rangle, \quad (4.10)$$

where

$$g_{\text{cav}}(\omega) = \sum_n (-1)^n e^{-(\omega - n\bar{\omega})^2 / 2(\Delta\omega)^2}. \quad (4.11)$$

Here, \mathcal{N}_β is the normalisation constant. In contrast to $|\Psi_\alpha\rangle$, Eq. (4.10) features the product $g_{\text{cav}}(\omega_s) f_{\text{cav}}(\omega_i)$, where $g_{\text{cav}}(\omega)$ is a superposition of Gaussians corresponding to odd

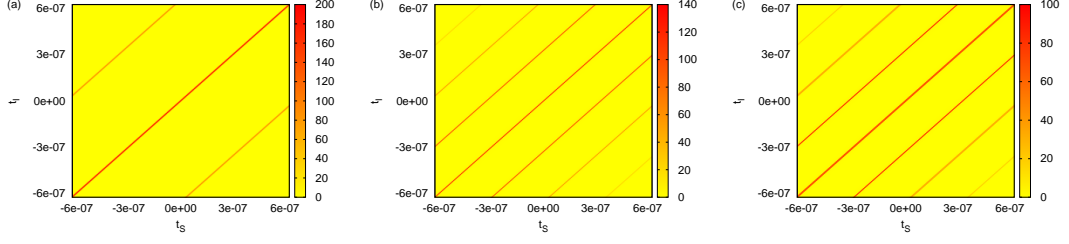


Figure 4.15: Tomographic time-time slice (a) $w^\alpha(t_s; t_l)$ and (b) $w^\beta(t_s; t_l)$ vs. t_s and t_l in seconds. (c) Difference $|w^\alpha(t_s; t_l) - w^\beta(t_s; t_l)|$ vs. t_s and t_l in seconds.

and even n such that the two are out of phase with each other. In Appendix E, we establish in a straightforward manner that the expressions above in Eqs. (4.7) and (4.10) indeed correspond to the two states of concern in the experiment. In what follows, we will use the tomographic approach to distinguish between the two 2-photon states. Since photon *coincidence* counts were used to experimentally distinguish between the two states, it is reasonable to expect that the time-time slices of the tomograms corresponding to the two 2-photon states will capture the difference.

The time-time slice of the tomogram corresponding to the state $|\Psi_x\rangle$ ($x = \alpha, \beta$) is given by

$$w^x(t_s; t_l) = \langle t_s; t_l | \Psi_x \rangle \langle \Psi_x | t_s; t_l \rangle, \quad (4.12)$$

where $|t_s; t_l\rangle$ stands for $|t_s\rangle \otimes |t_l\rangle$. We point out that this is analogous to the bipartite optical tomogram (Eq. (2.7)).

We work with the parameter values used in [28], namely, $\omega_p/(2\pi) = 391.8856$ THz, $\bar{\omega}/(2\pi) = 19.2$ GHz, $\Delta\omega/(2\pi) = 1.92$ GHz, $\Omega_0/(2\pi) = 10.9$ THz, and $\Delta\Omega/(2\pi) = 6$ THz. The time-time slices of the tomograms of $|\Psi_\alpha\rangle$ and $|\Psi_\beta\rangle$ have been obtained by substituting Eqs. (4.7) and (4.10) in turn in Eq. (4.12) and simplifying the resulting expressions (see Appendix F).

As expected, $w^\alpha(t_s; t_l)$ and $w^\beta(t_s; t_l)$ are distinctly different from each other, as seen in Figs. 4.15 (a)-(c). This difference arises because $|\Psi_\alpha\rangle$ and $|\Psi_\beta\rangle$ correspond to combs that are clearly displaced with respect to each other, when expressed in the time-time basis.

Next, we calculate the reduced tomograms $w_i^x(t_i)$ corresponding to subsystem i (where $i = \text{S, I}$ and $x = \alpha, \beta$) by integrating out the other subsystem, as has been

done in Eqs. (2.10) and (2.11) in the case of the optical tomograms. (For instance, $w_s^x(t_s) = \int dt_1 w^x(t_s; t_1)$.) Substituting these full-system and subsystem chronocyclic tomograms in place of the corresponding optical tomograms in Eqs. (3.1)–(3.3), we obtain the entanglement indicator ε_{TEI} corresponding to any chosen slice of the chronocyclic tomogram. (For ease of notation, we have dropped the explicit dependence of ε_{TEI} on the choice of both the tomogram slice and the specific state.) In the case of the time-time slice of the tomograms we get, finally, the values $\varepsilon_{\text{TEI}} = 6.50$ for the state $|\Psi_\alpha\rangle$, and $\varepsilon_{\text{TEI}} = 5.44$ for the state $|\Psi_\beta\rangle$. Thus, ε_{TEI} clearly distinguishes between these two 2-photon states. We emphasize that the methods used by us could, in principle, provide an alternative approach to the procedure adopted [28] in the experiment.

4.6 Concluding remarks

Entanglement monotones such as ξ_{SVNE} and ξ_{SLE} can be constructed only if the off-diagonal elements of the density operator are known. For a single-mode system, the optical tomogram is related to the density matrix ρ by

$$w(X_\theta, \theta) = \sum_{n,m=0}^{\infty} \langle X_\theta, \theta | n \rangle \rho_{nm} \langle m | X_\theta, \theta \rangle, \quad (4.13)$$

where $\rho_{nm} = \langle n | \rho | m \rangle$ and $\{|n\rangle\}$, $\{|m\rangle\}$ constitute the Fock basis. To get ρ_{nm} from the tomogram $w(X_\theta, \theta)$, we need to invert Eq. (4.13). But this is essentially the procedure for a full state reconstruction which could be tedious and error-prone. As has been pointed out in [1], even in linear inversion procedures to get ρ from histograms obtained experimentally, small errors in the experimental data get magnified substantially. Improved procedures for minimising errors are of great interest and possibilities for improvement have been explored both experimentally and theoretically (see, for instance, [84, 85, 2, 86]). Experimental challenges are primarily associated with gaining sufficient phase information from more than one copy of the system. Studies in this regard largely focus on reconstructing single-mode density matrices minimising the errors. Adapting and extending these ideas to entangled states which is of direct relevance to us, would be a significant step towards extracting entanglement monotones.

We have demonstrated that, even without information about the off-diagonal ele-

ments of the density matrix, substantial reproduction of the qualitative aspects of entanglement dynamics can be achieved *using the tomograms alone*. The performance of the entanglement indicator ξ'_{TEI} thus obtained, in quantifying the extent of entanglement, has been assessed in this chapter using two model bipartite systems with inherent nonlinearities. We have shown that ξ'_{TEI} fares significantly better for generic initial states of the system even during temporal evolution, compared to better-known entanglement indicators such as ξ_{IPR} . In order to quantify the reliability of the indicator over long intervals of time, the difference between ξ_{SVNE} and ξ'_{TEI} has been examined using a time-series analysis. The manner in which this difference $d_1(t)$ is sensitive to the nonlinearity of the system, the nature of the interaction, and the precise initial state is revealed by the time-series analysis. The importance and relevance of this investigation lies in the fact that detailed state reconstruction from the tomogram is completely avoided in identifying an efficient entanglement indicator for generic bipartite systems involving continuous variables.

Further, we have considered a pair of 2-photon states which were experimentally shown to be distinguishable, using the difference in their normalised photon coincidence counts [28]. Here we have unambiguously distinguished between these states using the entanglement indicator ε_{TEI} . This demonstrates an alternative procedure using the tomographic approach in an experimentally relevant CV system.

In the next chapter, we extend the investigation to multipartite HQ systems. We shall also demonstrate the utility of the indicator ξ_{TEI} with an experimentally-generated tomogram using the IBM quantum computer, and with a spin tomogram computed from experimental data from an NMR experiment [30].

CHAPTER 5

Dynamics of entanglement indicators in hybrid quantum systems and spin systems

5.1 Introduction

Interesting phenomena such as sudden death and birth of entanglement can arise during temporal evolution in certain HQ systems such as the double Jaynes-Cummings (DJC) model [25] and the double Tavis-Cummings (DTC) model [87]. These models of atom-field interactions have been investigated extensively in the literature [88–90]. We examine the performance of ξ_{TEI} and ξ'_{TEI} in these models by comparing them with the quantum mutual information ξ_{QMI} at various instants of time during temporal evolution. ξ_{QMI} is a useful measure of the quantum correlation between any two subsystems of a multipartite system and is defined as (Eq. (4.6)),

$$\xi_{\text{QMI}} = \xi_{\text{SVNE}}^{(\text{A})} + \xi_{\text{SVNE}}^{(\text{B})} - \xi_{\text{SVNE}}^{(\text{AB})}.$$

Here the superscripts (A), (B) and (AB) in the RHS refer to the subsystems A, B and the bipartite subsystem AB respectively. The terms, *quantum correlation* and *entanglement* will be used interchangeably in this chapter, as the former sets the upper bound on the latter for any two subsystems.

We have numerically generated tomograms at various instants during temporal evolution in the DJC and the DTC models. Wherever possible, we have compared these tomograms with those obtained from equivalent circuits executed in the IBM quantum computing platform (IBM Q). The tomograms from the IBM quantum computer have been obtained both through experimental runs and through simulations using the IBM open quantum assembly language (QASM) simulator [91, 92].

We have also extended our investigations to spin systems. For this purpose, we have used the reconstructed density matrices from the liquid-state NMR experiment,

provided to us by the NMR-QIP group in IISER Pune, India. This experiment has been performed using NMR spectroscopic techniques on ^{13}C , ^1H and ^{19}F atoms in dibromofluoromethane dissolved in acetone. The extent of entanglement has been quantified using negativity at various instants of time [30]. Since our aim is to assess the usefulness of ξ_{TEI} , we have numerically calculated the tomograms from these reconstructed density matrices, and compared ξ_{TEI} with ξ_{QMI} and negativity.

In Section 5.2, we describe and investigate the DJC and the DTC models. In Section 5.3, we analyse tomograms corresponding to the NMR system. We also comment on the spin, higher-order and entropic squeezing properties in this system. We conclude with brief remarks.

5.2 Hybrid multipartite models

We now proceed to assess the efficacy of ξ_{TEI} and ξ'_{TEI} in the DJC and DTC models.

5.2.1 The double Jaynes-Cummings model

The model comprises two 2-level atoms C and D which are initially in an entangled state, with each atom interacting with strength g_0 with radiation fields A and B respectively. The effective Hamiltonian (setting $\hbar = 1$) is [25]

$$H_{\text{DJC}} = \sum_{j=\text{A,B}} \chi_j a_j^\dagger a_j + \sum_{k=\text{C,D}} \chi_0 \sigma_{kz} + g_0 (a_{\text{A}}^\dagger \sigma_{\text{C}-} + a_{\text{A}} \sigma_{\text{C}+}) + g_0 (a_{\text{B}}^\dagger \sigma_{\text{D}-} + a_{\text{B}} \sigma_{\text{D}+}). \quad (5.1)$$

a_j, a_j^\dagger ($j = \text{A,B}$) are photon annihilation and creation operators, χ_j is the frequency of the fields, and χ_0 is the energy difference between the two atomic levels. In terms of the matrices σ_x , σ_y and σ_z (Eq. (3.13)), the atomic ladder operators for subsystem k are given by $\sigma_{k\pm} = (\sigma_{kx} \pm i\sigma_{ky})$. The initial atomic states considered both in the DJC model and the DTC model are of the form

$$|\psi_+\rangle = (|g\rangle_1 \otimes |g\rangle_2 + |e\rangle_1 \otimes |e\rangle_2) / \sqrt{2} \quad (5.2)$$

and

$$|\phi_+\rangle = (|g\rangle_1 \otimes |e\rangle_2 + |e\rangle_1 \otimes |g\rangle_2) / \sqrt{2}. \quad (5.3)$$

Here $|g\rangle_p$ and $|e\rangle_p$ ($p = 1, 2$) denote the respective ground and excited states of atom p . In the DJC model, 1 and 2 are to be replaced by C and D respectively. A and B are initially in the zero-photon states $|0\rangle_A$ and $|0\rangle_B$. The two initial states of the full system that we consider are $|0\rangle_A \otimes |0\rangle_B \otimes |\psi_+\rangle_{CD} \equiv |0; 0; \psi_+\rangle$ and $|0\rangle_A \otimes |0\rangle_B \otimes |\phi_+\rangle_{CD} \equiv |0; 0; \phi_+\rangle$.

We have numerically generated tomograms at approximately 300 instants of time, separated by a time step equal to 0.02 (in units of π/g_0). From these, we have obtained ξ_{TEI} at different instants as the system evolves. It was shown in Chapter 4 that for radiation fields, both ξ_{TEI} and ξ'_{TEI} were in fairly good agreement [36]. (We recall that the latter was computed by averaging over only those values of $\varepsilon_{\text{TEI}}(\theta_A, \theta_B)$ that exceed the mean by one standard deviation). We now proceed to investigate if this holds even in the case of HQ systems.

The entanglement indicators ξ_{TEI} , ξ'_{TEI} and ξ_{QMI} are plotted against the scaled time $g_0 t$ in Figs. 5.1 (a)-(c) in the case of the field subsystems. The detuning parameter, given by $(\chi_F - \chi_0)$, is 0 in Figs. 5.1 (a), (b), and 1 in Fig. 5.1 (c). The initial states considered are $|0; 0; \phi_+\rangle$ in Fig. 5.1 (a) and $|0; 0; \psi_+\rangle$ in Figs. 5.1 (b),(c). For ease of comparison, ξ_{QMI} has been scaled down by a factor of 10. It is evident that ξ'_{TEI} is a good approximation to ξ_{TEI} and that both mimic ξ_{QMI} closely in all the three cases considered. Sensitivity to the precise initial atomic state and to the extent of detuning is revealed by examining the qualitative features of the indicators in the neighbourhood of their maximum values.

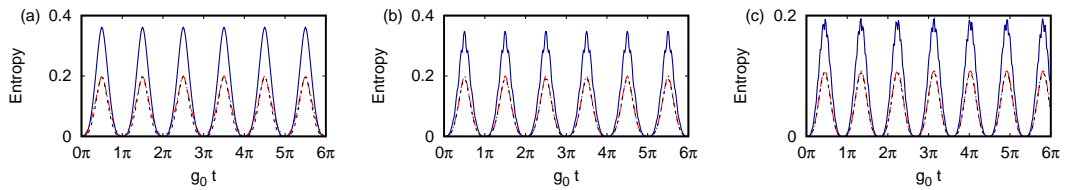


Figure 5.1: ξ_{TEI} (black), ξ'_{TEI} (blue) and $0.1 \xi_{\text{QMI}}$ (red) vs. scaled time $g_0 t$ for the field subsystem in the DJC model. Initial state (a) $|0; 0; \phi_+\rangle$; (b), (c) $|0; 0; \psi_+\rangle$. Detuning parameter (a),(b) 0 and (c) 1.

Figs. 5.2 (a)-(c) are plots of ξ_{TEI} , ξ'_{TEI} and ξ_{QMI} corresponding to the atomic subsystem for the same set of parameters and initial states as in Figs. 5.1 (a)-(c). In this case, although ξ_{TEI} is in good agreement with ξ_{QMI} over the time interval considered, ξ'_{TEI} is

not, in sharp contrast to the situation for the field subsystems. We note that when the detuning parameter is zero, ξ_{QMI} returns to its initial value of 2 at the instant $g_0 t = \pi$. We will use this feature in the sequel, when we construct an equivalent circuit for the DJC model.

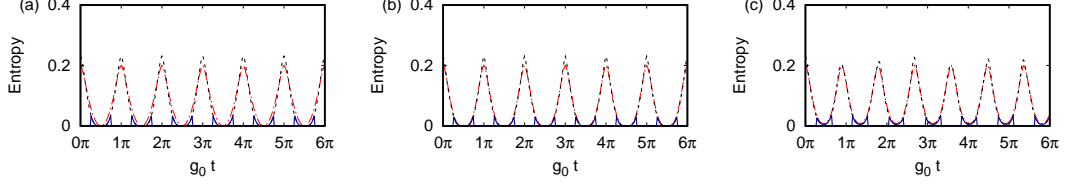


Figure 5.2: ξ_{TEI} (black), ξ'_{TEI} (blue) and $0.1 \xi_{\text{QMI}}$ (red) vs. scaled time $g_0 t$ for the atomic subsystem in the DJC model. Initial state (a) $|0; 0; \phi_+\rangle$; (b), (c) $|0; 0; \psi_+\rangle$. Detuning parameter (a),(b) 0 and (c) 1.

The equivalent circuit that was provided by us to the IBM Q from which bipartite qubit tomograms are obtained (analogous to the tomograms corresponding to the atomic subsystem of the DJC model) is shown in Fig. 5.3. We use the standard notation of the IBM platform [91]. In the circuit, $q[0]$ and $q[4]$ are the qubits that follow the dynamics of the atomic subsystem while $q[2]$ and $q[3]$ act as auxiliary qubits to aid the dynamics. Since transitions between the two energy levels of either atom in the DJC model involve absorption or emission of a single photon, each auxiliary qubit in the equivalent circuit toggles between the qubit states $|0\rangle$ and $|1\rangle$ respectively. The operator $U_3(\theta', \varphi', v)$ in the circuit is given by

$$U_3(\theta', \varphi', v) = \begin{bmatrix} \cos(\theta'/2) & -e^{iv} \sin(\theta'/2) \\ e^{i\varphi'} \sin(\theta'/2) & e^{i(v+\varphi')} \cos(\theta'/2) \end{bmatrix}, \quad (5.4)$$

where $0 \leq \theta' < \pi$, $0 \leq \varphi' < 2\pi$ and $0 \leq v < 2\pi$. Each of the four qubits is initially in the qubit state $|0\rangle$. The initial entangled state between $q[0]$ and $q[4]$ (analogous to the initial state $|\psi_+\rangle$ of the atomic subsystem) is prepared in the circuit using an Hadamard and a controlled-NOT gate between $q[4]$ and $q[2]$ and a SWAP gate between $q[2]$ and $q[0]$. Here, θ' is analogous to $g_0 t$ in the DJC model. We choose $\theta' = \pi$ so that the extent of entanglement is equal to its initial value ($= 2$), $\varphi' = 0$ and $v = \pi/2$. The matrix $U_3(\pi, \pi/2, \pi)$ which appears in the equivalent circuit is equal to $U_3^\dagger(\pi, 0, \pi/2)$. Measurements are carried out in the x , y and z bases corresponding to the matrices defined in Eq. (3.13). A measurement in the z -basis is automatically provided by the IBM platform. A measurement in the x -basis is achieved by applying an Hadamard

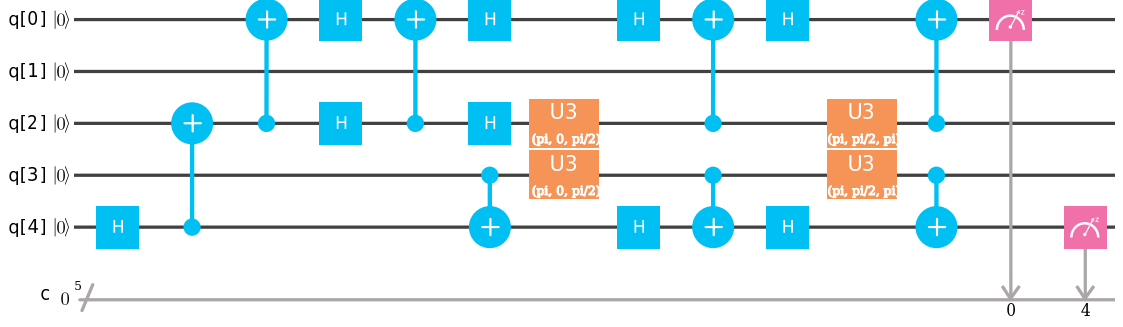


Figure 5.3: Equivalent circuit for the DJC model (created using IBM Q).

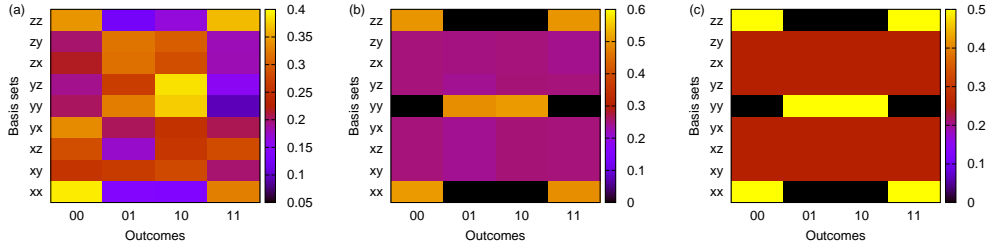


Figure 5.4: Tomograms from (a) IBM Q experiment (b) QASM simulation (c) numerical computations of the DJC model.

gate followed by a z -basis measurement. Defining the operator

$$S^\dagger = \begin{bmatrix} 1 & 0 \\ 0 & -i \end{bmatrix}, \quad (5.5)$$

measurement in the y -basis is achieved by applying S^\dagger , then an Hadamard gate, and finally a measurement in the z -basis. Measurements in the x , y and z bases are needed for obtaining the spin tomogram, Fig. 5.4 (a). (This is equivalent to the bipartite atomic tomogram in the DJC model, in the basis sets of σ_x , σ_y and σ_z).

These spin tomograms have also been obtained experimentally using the IBM superconducting circuit with appropriate Josephson junctions (Fig. 5.4 (a)), and the QASM simulator provided by IBM. The latter does not take into account losses at various stages of the circuit (Fig. 5.4 (b)). These tomograms are compared with the atomic tomograms (Fig. 5.4 (c)) of the DJC model with decoherence effects neglected. The qualitative features are very similar in Figs. 5.4 (b) and (c) as the circuit follows the dynamics of the atomic subsystem of the DJC model. As expected, Fig. 5.4 (a) is distinctly different due to experimental losses.

From these tomograms, ξ_{TEI} has been calculated. The values obtained from the ex-

periment, simulation and numerical analysis are 0.0410 ± 0.0016 , 0.2311 and 0.2310 , respectively. Six tomograms were obtained from six executions of the experiment. Each execution comprised 8192 runs over each of the 9 basis sets. The error bar was calculated from the standard deviation of ξ_{TEI} .

It is instructive to estimate the extent of loss in state preparation *alone*. For this purpose, an entangled state of two qubits was prepared using an Hadamard and a controlled-NOT gate, to effectively mimic $|\psi_+\rangle$. For the initial state $|\psi_+\rangle$, the values for ξ_{TEI} obtained from the experiment, simulation and the DJC model are 0.0973 ± 0.0240 , 0.2310 and 0.2310 respectively. This demonstrates that substantial losses arise even in state preparation. In order to examine the extent to which an increase in the number of atoms in the system increases these losses, we turn to the DTC model.

5.2.2 The double Tavis-Cummings model

The model comprises four two-level atoms, C_1 , C_2 , D_1 and D_2 , with C_1 and C_2 (respectively, D_1 and D_2) coupled with strength g_0 to a radiation field A (resp., B) of frequency χ_F . The notation used is similar to that in H_{DJC} (Eq. (5.1)), since the Hamiltonian H_{DTC} can be obtained from the former by appropriate changes. Setting $\hbar = 1$, we have [87],

$$H_{\text{DTC}} = \sum_{j=A,B} \chi_F a_j^\dagger a_j + \sum_{k=1}^2 \left\{ \chi_0 \sigma_{C_k z} + \chi_0 \sigma_{D_k z} + g_0 (a_A^\dagger \sigma_{C_k -} + a_A \sigma_{C_k +}) + g_0 (a_B^\dagger \sigma_{D_k -} + a_B \sigma_{D_k +}) \right\}, \quad (5.6)$$

C_1 and D_1 (respectively, C_2 and D_2) are in the initial state $|\psi_+\rangle$ (Eq. (5.2)) or $|\phi_+\rangle$ (Eq. (5.3)). Each field is initially in $|0\rangle$. We therefore consider the initial states $|0; 0; \psi_+; \psi_+\rangle$, $|0; 0; \phi_+; \phi_+\rangle$ and $|0; 0; \psi_+; \phi_+\rangle$. The notation $|0; 0; \psi_+; \phi_+\rangle$ indicates, for instance, that A and B are in the state $|0\rangle$, the subsystem (C_1, D_1) is in the state $|\psi_+\rangle$, and the subsystem (C_2, D_2) is in the state $|\phi_+\rangle$. (We do not consider the initial state $|0; 0; \phi_+; \psi_+\rangle$ separately because the results corresponding to that case can be obtained using symmetry arguments from the results for the initial state $|0; 0; \psi_+; \phi_+\rangle$). We shall denote (C_1, C_2) by C and (D_1, D_2) by D.

An equivalent circuit for the DTC model requires 4 qubits to mimic the four two-level atoms, and a minimum of 4 auxiliary qubits to aid the dynamics. In what follows,

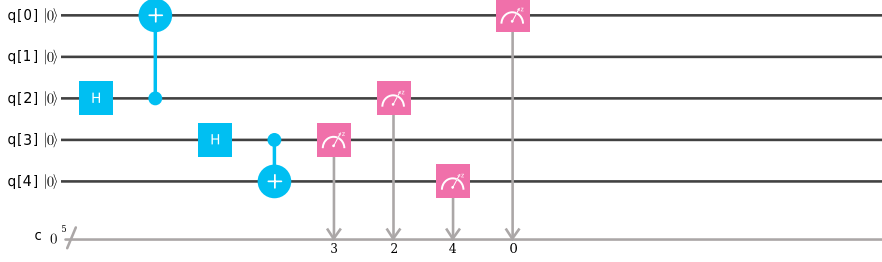


Figure 5.5: Equivalent circuit of the entangled state $|\psi_+; \psi_+\rangle$ in the DTC model (created using IBM Q).

we assess the extent of losses in state preparation *alone*. For this purpose, 4 qubits are prepared in a pairwise entangled state (analogous to the initial state $|\psi_+; \psi_+\rangle$ of the atomic subsystem (C,D)) using 2 Hadamard and 2 controlled-NOT gates (Fig. 5.5). Here qubits $q[2]$ and $q[3]$ are entangled with qubits $q[0]$ and $q[4]$ respectively. We note that the pair $(q[2], q[3])$ is analogous to subsystem C, and $(q[0], q[4])$ is analogous to D. The extent of entanglement between C and D is quantified using ξ_{TEI} . The numerical values obtained from experiment, simulation and the DTC model are 0.2528, 0.4761 and 0.4621, respectively. In this case, the experiment was executed just once. This comprised 8192 runs [91] over each of the 81 basis sets. Thus the outcome of the experiment, namely 0.2528, is not prescribed with an error bar. As 4 qubits are involved in this circuit, the number of possible outcomes is 16, in contrast to the earlier case which had only 4 outcomes. Hence, the experimental losses, as well as the difference between the simulated and the numerically obtained values, are higher than those obtained for the DJC model. We therefore proceed to investigate the entanglement dynamics in the DTC model numerically in the absence of losses.

We now investigate the extent of entanglement between the field subsystems A and B, and between the atomic subsystems C and D, as the system evolves in time. For this purpose, we have generated tomograms at 300 instants separated by a time step 0.02 in units of π/g_0 setting the detuning parameter to zero without loss of generality. From these, ξ_{TEI} and ξ'_{TEI} have been obtained. Plots of ξ_{TEI} , ξ'_{TEI} and ξ_{QMI} for the field subsystem is shown in Figs. 5.6 (a)-(c) and for the atomic subsystem in Figs. 5.7 (a)-(c).

As in the DJC model, we see that both ξ_{TEI} and ξ'_{TEI} mimic ξ_{QMI} effectively for the field subsystem, while ξ'_{TEI} does not reflect ξ_{QMI} for the atomic subsystem. We therefore do not expect ξ'_{TEI} to quantify entanglement reasonably in spin systems also. Hence we now proceed to assess the extent of entanglement using ξ_{TEI} as the entanglement

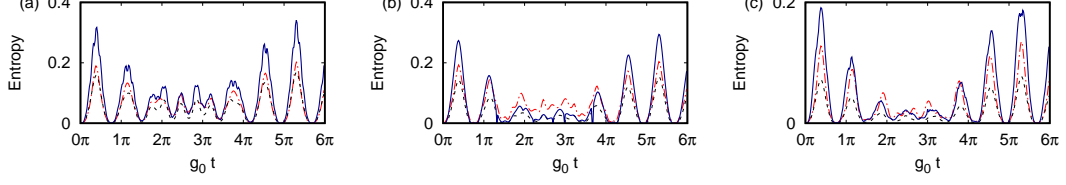


Figure 5.6: ξ_{TEI} (black), ξ'_{TEI} (blue) and $0.1 \xi_{\text{QMI}}$ (red) vs. scaled time $g_0 t$ for the field subsystem in the DTC model with zero detuning. Initial field state $|0; 0\rangle$, initial atomic state (a) $|\psi_+; \psi_+\rangle$ (b) $|\phi_+; \phi_+\rangle$ (c) $|\psi_+; \phi_+\rangle$.

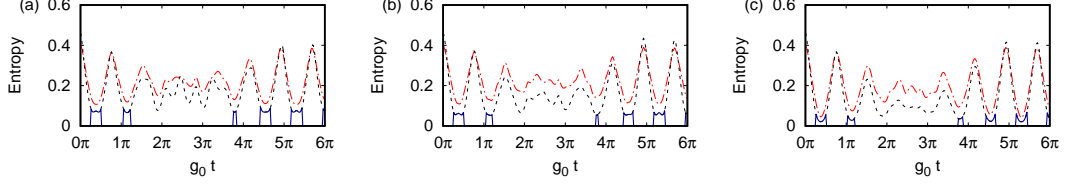


Figure 5.7: ξ_{TEI} (black), ξ'_{TEI} (blue) and $0.1 \xi_{\text{QMI}}$ (red) vs. scaled time $g_0 t$ for the bipartite atomic subsystem CD in the DTC model with zero detuning. Initial field state $|0; 0\rangle$, initial atomic state (a) $|\psi_+; \psi_+\rangle$ (b) $|\phi_+; \phi_+\rangle$ (c) $|\psi_+; \phi_+\rangle$.

indicator in a specific spin system.

5.3 The spin system

We now proceed to examine, by means of tomograms, an entangled system of spins on which an NMR experiment has been performed and reported in the literature [30]. Whereas our investigations on the multipartite HQ systems using the IBM Q platform highlighted the role played by experimental losses which were not taken into account in numerically generated tomograms, our present aim is somewhat different. Here we wish to examine quantitatively the limitations that arise in the tomographic approach from neglecting the off-diagonal contributions in the density matrix.

There is also another aspect of interest to us here. In generic multipartite spin systems where the subsystem states are entangled, spin squeezing and entanglement are related to each other [93]. With this in mind, we will first assess the squeezing properties of the spin system, quantify entanglement with ξ_{TEI} , and comment on the similarities in the dynamics of spin squeezing and entanglement. As mentioned in Section 5.1, our starting point is the set of reconstructed density matrices at different instants of time obtained from the experiment. The system of interest comprises ^{13}C atoms (subsystem M), ^1H atoms (subsystem A) and ^{19}F atoms (subsystem B) in dibromofluoromethane,

evolving in time. Each subsystem is a qubit, and the effective Hamiltonian [30] is

$$H_S = 4\chi_s(\sigma_{Ax} + \sigma_{Bx})\sigma_{Mx}, \quad (5.7)$$

where χ_s is a constant, σ_x is the usual spin matrix, and the subscripts A, B and M refer to the corresponding subsystems. The eigenstates of σ_x are denoted by $|+\rangle$ and $|-\rangle$.

The density matrix at time $t = 0$ is

$$\rho_{MAB}(0) = \frac{1}{2} |\phi_+\rangle_{AB} \langle\phi_+| \otimes \rho_{M+} + \frac{1}{2} |\psi_+\rangle_{AB} \langle\psi_+| \otimes \rho_{M-}, \quad (5.8)$$

where $|\psi_+\rangle_{AB}$ and $|\phi_+\rangle_{AB}$ are defined as in Eqs. (5.2) and (5.3) respectively, with the replacement of $|e\rangle$ by $|\uparrow\rangle$ and $|g\rangle$ by $|\downarrow\rangle$. Here, $|\uparrow\rangle$ and $|\downarrow\rangle$ refer to the up and down eigenstates of σ_z and $\rho_{M+} = |+\rangle_M \langle+|$, $\rho_{M-} = |-\rangle_M \langle-|$. It is straightforward to show that, at any $t > 0$,

$$\begin{aligned} \rho_{MAB}(t) = & \frac{1}{2} \cos^2(2\chi_s t) \{ |\phi_+\rangle_{AB} \langle\phi_+| \otimes \rho_{M+} + |\psi_+\rangle_{AB} \langle\psi_+| \otimes \rho_{M-} \} \\ & + \frac{1}{2} \sin^2(2\chi_s t) \{ |\psi_+\rangle_{AB} \langle\psi_+| \otimes \rho_{M+} + |\phi_+\rangle_{AB} \langle\phi_+| \otimes \rho_{M-} \} \\ & + \frac{1}{4} i \sin(4\chi_s t) \{ |\phi_+\rangle_{AB} \langle\psi_+| \otimes \mathbb{I}_M - |\psi_+\rangle_{AB} \langle\phi_+| \otimes \mathbb{I}_M \}, \end{aligned} \quad (5.9)$$

where \mathbb{I}_M denotes the identity matrix corresponding to subsystem M. The experimentally reconstructed density matrices at different instants have been provided to us by the NMR-QIP group in IISER Pune, India. We are concerned with the reduced density matrix

$$\rho_{AB}(t) = \text{Tr}_M(\rho_{MAB}(t)), \quad (5.10)$$

corresponding to the subsystem AB.

In order to examine its squeezing properties, we use the spin squeezing condition proposed by Kitagawa and Ueda [94]. A bipartite system consisting of two spin- $\frac{1}{2}$ subsystems is squeezed, if one of the components normal to the mean spin vector of the bipartite system has a variance less than 0.5 (the latter being the variance of the corresponding spin coherent state). Here, the spin coherent state for the bipartite system AB is defined in terms of the polar and azimuthal angles (ϑ, φ) as $(\cos \vartheta |\downarrow\rangle_A + e^{i\varphi} \sin \vartheta |\uparrow\rangle_A) \otimes (\cos \vartheta |\downarrow\rangle_B + e^{i\varphi} \sin \vartheta |\uparrow\rangle_B)$. For completeness, the tomograms corresponding to spin coherent states for four different (ϑ, φ) values are shown

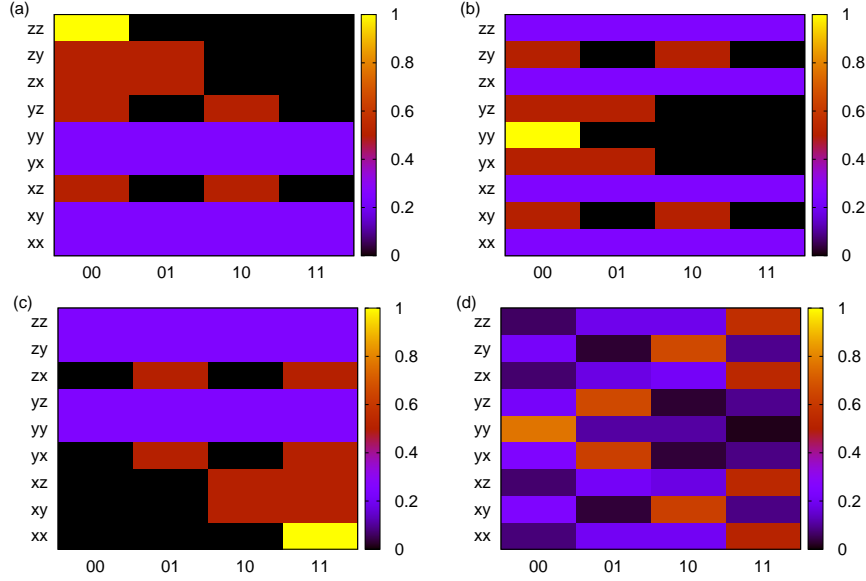


Figure 5.8: Tomograms of spin coherent states with (ϑ, φ) equal to (a) $(0, 0)$, (b) $(\pi/4, \pi/2)$, (c) $(\pi/4, 0)$, and (d) $(2\pi/3, 4\pi/3)$. The bases are denoted by x, y and z and the outcomes by 0 and 1.

in Figs. 5.8 (a)-(d). Each of the figures (a), (b), and (c) corresponds to one of the eigenstates of $\sigma_{Az} \sigma_{Bz}$, $\sigma_{Ay} \sigma_{By}$ and $\sigma_{Ax} \sigma_{Bx}$, respectively. The tomogram corresponding to a spin coherent state for $\vartheta = 2\pi/3, \varphi = 4\pi/3$ is plotted in Fig. 5.8 (d).

The mean spin direction is given by $\mathbf{v}_s(t) = \langle \mathbf{J}(t) \rangle / |\langle \mathbf{J}(t) \rangle|$ where

$$\mathbf{J} = (\sigma_{Ax} + \sigma_{Bx})\mathbf{e}_x + (\sigma_{Ay} + \sigma_{By})\mathbf{e}_y + (\sigma_{Az} + \sigma_{Bz})\mathbf{e}_z, \quad (5.11)$$

and $\langle \mathcal{O}(t) \rangle = \text{Tr}_{AB}(\rho_{AB}(t)\mathcal{O})$ for any operator \mathcal{O} . Since $\langle \sigma_{ix}(t) \rangle$, $\langle \sigma_{iy}(t) \rangle$ and $\langle \sigma_{iz}(t) \rangle$ ($i = A, B$) are equal to zero, it follows that $\mathbf{v}_s(t)$ is a null vector. Hence, any unit vector \mathbf{v}_\perp can be chosen to obtain the required variance. We have calculated the variance $(\Delta \mathbf{J} \cdot \mathbf{v}_\perp)^2 = \langle (\mathbf{J} \cdot \mathbf{v}_\perp)^2 \rangle$ as a function of time for 800 different vectors \mathbf{v}_\perp at each instant. From this, we have identified the minimum variance $(\Delta J_{\min})^2$ and plotted it as a function of time (Fig. 5.9(a)). From the figure, it is evident that the variance obtained numerically using Eq. (5.10) and that obtained from the experimentally reconstructed density matrices are in good agreement. We also point out that the extent of squeezing, $[1 - 2(\Delta J_{\min})^2]$, increases with time.

We adapt the Kitagawa-Ueda squeezing condition in the following manner in order to estimate second-order squeezing. By an extension of the preceding argument, we consider the expectation value of the dyad (or tensor product) $\mathbf{J}\mathbf{J}$ instead of $\langle \mathbf{J} \rangle$. In

general, $\langle \mathbf{J}\mathbf{J} \rangle$ is not a null tensor. We may therefore impose the orthogonality condition $\langle \mathcal{J} \rangle = 0$, where

$$\mathcal{J} = \frac{1}{2} (\mathbf{v}_1 \cdot \mathbf{J}\mathbf{J} \cdot \mathbf{v}_2 + \mathbf{v}_2 \cdot \mathbf{J}\mathbf{J} \cdot \mathbf{v}_1). \quad (5.12)$$

\mathbf{v}_1 and \mathbf{v}_2 are analogous to the vector \mathbf{v}_\perp of the earlier case. The symmetrization with respect to \mathbf{v}_1 and \mathbf{v}_2 in Eq. (5.12) ensures that \mathcal{J} is real. Using Eq. (5.10), we get

$$\begin{aligned} \langle \mathcal{J}(t) \rangle &= \text{Tr}(\rho_{AB}(t)\mathcal{J}) \\ &= \mathbf{v}_{1x}\mathbf{v}_{2x} + \frac{1}{2} \{ \mathbf{v}_{1y}\mathbf{v}_{2y} + \mathbf{v}_{1z}\mathbf{v}_{2z} + \sin(4\chi_s t) (\mathbf{v}_{1y}\mathbf{v}_{2z} + \mathbf{v}_{2y}\mathbf{v}_{1z}) \}, \end{aligned} \quad (5.13)$$

where the subscripts x , y and z denote the respective components of \mathbf{v}_1 and \mathbf{v}_2 . (The symmetry between the y and z components in Eq. (5.13) follows from the fact that $[\sigma_{Ax}\sigma_{Bx}, \rho_{AB}(t)] = 0$). We have considered a set of 320 different pairs $(\mathbf{v}_1, \mathbf{v}_2)$ for which $\langle \mathcal{J}(t) \rangle = 0$. For each such pair, the variance $(\Delta\mathcal{J})^2$ has been computed, and from this the minimum variance $(\Delta\mathcal{J}_{\min})^2$ has been obtained. The reference value (0.125) below which the state is second-order squeezed is obtained by minimizing the corresponding variance for the spin coherent state with respect to ϑ and φ . Plots of $(\Delta\mathcal{J}_{\min})^2$ versus time obtained both from the experimentally reconstructed density matrices and from Eq. (5.10) are shown in Fig. 5.9(b). The two curves are in reasonable agreement with each other. As in the earlier case, the measure of second-order squeezing, $[1 - 8(\Delta\mathcal{J}_{\min})^2]$, increases with time. We have verified that neither the state of subsystem A nor that of B displays entropic squeezing [95] at any time.

We now turn to the entanglement dynamics in the NMR experiment [30]. We have computed ξ_{TEI} from tomograms obtained both from Eq. (5.10) and from the experimentally reconstructed density matrices at different instants of time. This is compared with two indicators, ξ_{QMI} and the negativity $N(\rho_{AB})$. The latter has been reported in the experiment, and is defined as $N(\rho_{AB}) = \frac{1}{2} \sum_i (|\mathcal{L}_i| - \mathcal{L}_i)$. Here $\{\mathcal{L}_i\}$ is the set of eigenvalues of $\rho_{AB}^{T_A}$, the partial transpose of ρ_{AB} with respect to the subsystem A. (Equivalently, the partial transpose $\rho_{AB}^{T_B}$ may be used.) Although all three entanglement indicators are in agreement in their gross features (Fig. 5.9 (c)), ξ_{TEI} is closer to ξ_{QMI} owing to the similarity in their definitions. The difference between ξ_{TEI} and negativity is clearly due to the limitations that arise in the tomographic approach because the off-diagonal contributions of the density matrix have been neglected. We emphasise, however, that ξ_{TEI} is still a good entanglement indicator which compares favourably with ξ_{QMI} . Figures 5.10

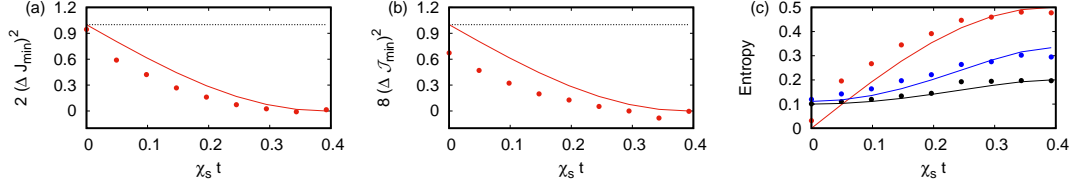


Figure 5.9: (a) $2(\Delta J_{\min})^2$ (b) $8(\Delta J_{\min})^2$ (c) $N(\rho_{AB})$ (red), ξ_{TEI} (blue), $0.1 \xi_{QMI}$ (black) vs. scaled time $\chi_s t$. The solid curves are computed using Eq. (5.10) and the dotted curves from experimental data. The black horizontal line in (a) and (b) sets the limit below which the state is squeezed.

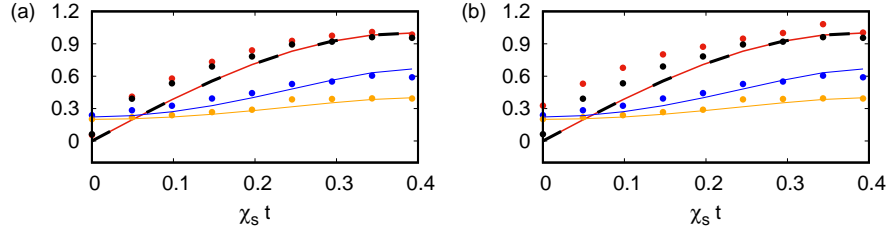


Figure 5.10: $2 N(\rho_{AB})$ (black), $2 \xi_{TEI}$ (blue), $0.2 \xi_{QMI}$ (orange), and (a) $[1 - 2(\Delta J_{\min})^2]$ (red) (b) $[1 - 8(\Delta J_{\min})^2]$ (red) vs. scaled time $\chi_s t$. The solid curves are computed using Eq. (5.10) and the dotted curves from experimental data.

(a) and (b) facilitate comparison between $[1 - 2(\Delta J_{\min})^2]$, $[1 - 8(\Delta J_{\min})^2]$, $N(\rho_{AB})$, ξ_{TEI} , and ξ_{QMI} . It is clear that $N(\rho_{AB})$ characterises the degree of squeezing and higher-order squeezing extremely well, and that ξ_{TEI} and ξ_{QMI} are reasonable quantifiers of squeezing properties.

5.4 Concluding remarks

In this chapter, we have compared the performance of ξ_{TEI} and ξ'_{TEI} with standard entanglement indicators in multipartite HQ models (DJC and DTC), and we have calculated ξ_{TEI} in the context of an NMR experiment. In the former, entanglement within the field subsystem and within the atomic subsystem have been examined. While ξ'_{TEI} satisfactorily mimics ξ_{QMI} for the field subsystem, it does not fare well in the atomic subsystem. In contrast, ξ_{TEI} performs well for both subsystems. An equivalent circuit for the DJC model was both experimentally run and numerically simulated to obtain ξ_{TEI} . This facilitates estimation of experimental losses. Our results show that the IBM simulation agrees well with numerical simulation of the DJC model. Further, we have established that in multipartite HQ models, the difference between ξ_{TEI} obtained experimentally and numerically increases significantly with an increase in the number of atoms. Corre-

sponding to the NMR experiment, we have shown that ξ_{TEI} is in fair agreement with both the negativity $N(\rho_{\text{AB}})$ and ξ_{QMI} . Further, it gives a reasonable estimate of squeezing and second-order squeezing. We therefore conclude that the entanglement indicator ξ_{TEI} obtained *directly* from tomograms is a convenient and practical quantifier of entanglement both in multipartite HQ systems and in spin systems.

CHAPTER 6

Conclusion

In this thesis, we have carried out a detailed investigation of the manner in which nonclassical effects such as wave packet revival phenomena, squeezing properties of different states, and quantum entanglement in bipartite systems, can be identified and quantitatively estimated directly from tomograms, without detailed state reconstruction. We have examined both single-mode and bipartite CV systems with more than one time scale, and investigated full and fractional revivals of quantum wave packets governed by nonlinear Hamiltonians. A range of squeezing phenomena such as quadrature squeezing, higher-order Hong-Mandel and Hillery-type squeezing, and entropic squeezing, have been examined in various quantum systems evolving in time. Several entanglement indicators that can be obtained from appropriate tomograms have been proposed, and their performance assessed through detailed comparison with standard measures of entanglement. We have examined CV, multipartite HQ, and spin systems in this thesis. In each of these cases, we have studied the nonclassical properties captured through numerically generated tomograms of quantum states obtained from known initial states evolving under nonlinear Hamiltonians. We have also worked with experimental data generated elsewhere (and in the IBM quantum computing platform). Thus comparison between experimentally obtained tomograms and numerically generated tomograms was feasible in certain cases. We have examined optical tomograms, qubit (spin) tomograms and chronocyclic tomograms in different contexts. We have used a range of initial states in our numerical computations. This includes the standard CS, PACS (equivalently, boson-added CS), direct products of these states, binomial states, and two-mode squeezed states.

Several bipartite entanglement indicators have been analysed both at avoided energy-level crossings of specific systems, and during temporal evolution of certain Hamiltonian systems. We have commented on decoherence effects wherever possible. Some of these indicators are inherently quantum mechanical in nature (such as ξ_{TEI} , ξ'_{TEI} and ξ_{IPR}) while others (ξ_{BD} and ξ_{PCC}) are inspired by classical tomography. The extent to which

nonlinear correlations are captured by these indicators has been assessed in detail. Our main results are the following.

- (1) We have established that, as an entanglement indicator and quantifier, ξ_{BD} performs as well as ξ_{TEI} close to avoided energy-level crossings in both CV and HQ systems.
- (2) If a bipartite state is a superposition of states that are Hamming-uncorrelated, ξ_{IPR} is a better entanglement indicator than ξ_{TEI} . In fact, we find that even ε_{IPR} (the corresponding indicator from a single section of the tomogram) suffices to estimate entanglement reliably near avoided energy-level crossings for superpositions of Hamming-uncorrelated states such as the eigenstates of certain number-conserving Hamiltonians.
- (3) In the context of bipartite CV systems ξ'_{TEI} (obtained by averaging only over the dominant ε_{TEI}) is found to be a reasonably good entanglement indicator. However, the extent to which it agrees with ξ_{SVNE} is very sensitive to the precise initial state, the nature of the interaction, and the inherent nonlinearities in the system.
- (4) In contrast to the foregoing inference, ξ'_{TEI} is a poor entanglement indicator for qubit systems, and ξ_{TEI} has to be used for such systems.

The tomographic approach to deriving entanglement indicators and distinguishing between states acquires further validation by its application to experiments on both CV and spin systems reported in the literature. In the former case, two 2-photon states generated experimentally were distinguished from each other using interferometric methods [28]. We have shown, by examining the entanglement indicator ε_{TEI} corresponding to a judiciously selected slice of the bipartite chronocyclic tomograms concerned, that these states can be distinguished clearly from each other. In the latter case, by analysing the experimental data [30] pertaining to the spin system of interest and constructing the corresponding qubit tomograms, we have established that ξ_{TEI} is a reasonably good bipartite entanglement indicator in this context. The limitations that arise from neglecting the contributions of off-diagonal elements of the density matrix (in computing the tomographic entanglement indicators) are clearly seen in this context. Further, using the IBM quantum computing platform we have shown that, even in multipartite HQ systems comprising radiation fields interacting with atomic subsystems, ξ_{TEI} extracted from appropriate qubit tomograms is a reasonably good bipartite entanglement indicator. Here, we have compared indicators computed from experimentally obtained tomograms, on

the one hand, and those computed from numerically generated tomograms which do not account for such losses, on the other. This facilitates understanding the role of experimental losses. The thesis also highlights how entanglement indicators which are not monotones (and hence not *bona fide* entanglement *measures*) can still mirror the qualitative features of bipartite entanglement quite well, with the added advantage that they can be computed from tomograms in a straightforward manner.

Finally, we mention some avenues for future research. The extension of our studies on nonclassical effects to multipartite systems, including the computation of multipartite entanglement indicators from tomograms, is an open question. In this context, a detailed assessment of the advantages, if any, of the tomographic approach over state reconstruction programmes needs to be carried out. Further, comparison with other quantifiers of entanglement in multipartite systems would facilitate a deeper understanding of the tomographic approach. The manner in which the nonclassicality of a state is mirrored in the tomogram (similar to negative values of the Wigner function) also merits examination in greater detail.

APPENDIX A

Eigenvectors of rotated quadrature operators

We first obtain a useful expression [38] for the single-mode tomogram in terms of the Hermite polynomials. We also indicate the procedure to obtain eigenvectors of rotated quadrature operators [96].

The overlap between a photon number state $|n\rangle$ and the field quadrature state $|X\rangle$ can be expressed in terms of the Hermite polynomials $H_n(X)$ as,

$$\langle X|n\rangle = (e^{-X^2/2} H_n(X)) / (\pi^{1/4} \sqrt{n! 2^n}).$$

Using this, and Eq. (2.4), we see that

$$\langle X_\theta, \theta|n\rangle = e^{-X_\theta^2/2} \frac{e^{-in\theta} H_n(X_\theta)}{\pi^{1/4} \sqrt{n! 2^{n/2}}}. \quad (\text{A.1})$$

For a pure state $|\psi\rangle$, $w(X_\theta, \theta) = |\langle X_\theta, \theta|\psi\rangle|^2$. Expanding $|\psi\rangle$ in the photon number basis $\{|p\rangle\}$ as $\sum_{p=0}^{\infty} c_p |p\rangle$, the corresponding tomogram is given by [38]

$$w(X_\theta, \theta) = \frac{e^{-X_\theta^2}}{\sqrt{\pi}} \left| \sum_{n=0}^{\infty} \frac{c_n e^{-in\theta}}{\sqrt{n! 2^{n/2}}} H_n(X_\theta) \right|^2.$$

The above expression can be extended in a straightforward manner to mixed states.

Using Eq. (A.1) and $|X_\theta, \theta\rangle = \sum_{p=0}^{\infty} |p\rangle \langle p|X_\theta, \theta\rangle$, we get

$$\begin{aligned} |X_\theta, \theta\rangle &= \sum_{n=0}^{\infty} \frac{e^{-X_\theta^2/2}}{\pi^{1/4}} H_n(X_\theta) \frac{e^{in\theta}}{\sqrt{n! 2^{n/2}}} |n\rangle \\ &= \frac{e^{-X_\theta^2/2}}{\pi^{1/4}} \sum_{n=0}^{\infty} \frac{H_n(X_\theta)}{n!} \left(\frac{e^{i\theta} a^\dagger}{\sqrt{2}} \right)^n |0\rangle, \end{aligned} \quad (\text{A.2})$$

where $|0\rangle$ is the zero-photon state. The generating function for the Hermite polynomials is

$$\sum_{p=0}^{\infty} H_p(x) \frac{t^p}{p!} = e^{2xt - t^2}. \quad (\text{A.3})$$

Substituting Eq. (A.3) in Eq. (A.2), we get [96]

$$|X_\theta, \theta\rangle = \frac{1}{\pi^{1/4}} \exp \left(-\frac{X_\theta^2}{2} + 2 X_\theta \frac{a^\dagger e^{i\theta}}{\sqrt{2}} - \left(\frac{a^\dagger e^{i\theta}}{\sqrt{2}} \right)^2 \right) |0\rangle. \quad (\text{A.4})$$

The procedure outlined above can be extended to obtain the corresponding expressions for multimode tomograms.

APPENDIX B

Normal-ordered moments from optical tomograms

We outline the procedure [23] for obtaining normal-ordered moments for infinite-dimensional single-mode systems from optical tomograms. We expand any normal-ordered operator F in the form

$$F = \sum_{k,l=0}^{\infty} F_{k,l} a^{\dagger k} a^l. \quad (\text{B.1})$$

Here the coefficients

$$F_{k,l} = \sum_{s=0}^{\{k,l\}} \frac{(-1)^s}{s! \sqrt{(k-s)!(l-s)!}} \langle k-s | F | l-s \rangle, \quad (\text{B.2})$$

and $\{k,l\}$ is used to denote $\min(k,l)$. (Equation (B.2) can be verified as follows. We first obtain $\langle p | F | q \rangle$ using Eq. (B.1). Substituting this in Eq. (B.2), we get

$$F_{k,l} = \sum_{s=0}^{\{k,l\}} \sum_{u=0}^{\{k-s,l-s\}} \frac{(-1)^s}{s! u!} F_{k-s-u, l-s-u}. \quad (\text{B.3})$$

Now replacing u with $u' = s + u$, changing the order of the sums, and using

$$\sum_{s=0}^k \frac{(-1)^s}{s! (k-s)!} = \delta_{k,0}, \quad (\text{B.4})$$

it follows that the expansion of F above is valid.)

We write the projection operator

$$|k\rangle \langle l| = (k!l!)^{-1/2} \sum_{u=0}^{\infty} \frac{(-1)^u}{u!} a^{\dagger k+u} a^{l+u}. \quad (\text{B.5})$$

Using $F = \sum_{k,l=0}^{\infty} |l\rangle \langle k| \text{Tr}(|k\rangle \langle l| F)$ and Eq. (B.5), we see that

$$F = \sum_{k,l=0}^{\infty} A_{k,l} \text{Tr}(a^{\dagger k} a^l F). \quad (\text{B.6})$$

Here

$$A_{k,l} = \sum_{s=0}^{\{k,l\}} \frac{(-1)^s}{s! \sqrt{(k-s)!(l-s)!}} |l-s\rangle \langle k-s|. \quad (\text{B.7})$$

We now consider the special case when F is the density operator ρ . Using Eqs. (B.6), (B.7),

$$\langle X_\theta, \theta | m \rangle \langle n | X_\theta, \theta \rangle = \frac{e^{-X_\theta^2}}{\sqrt{\pi}} \frac{e^{-i(m-n)\theta}}{\sqrt{m!n!}\sqrt{2^{m+n}}} H_m(X_\theta) H_n(X_\theta), \quad (\text{B.8})$$

and the following property of the Hermite polynomials

$$H_{k+l}(X_\theta) = \sum_{s=0}^{\{k,l\}} \frac{(-2)^s k!l! H_{k-s}(X_\theta) H_{l-s}(X_\theta)}{s!(k-s)!(l-s)!}, \quad (\text{B.9})$$

we can show that

$$\begin{aligned} w(X_\theta, \theta) &= \langle X_\theta, \theta | \rho | X_\theta, \theta \rangle \\ &= \frac{e^{-X_\theta^2}}{\sqrt{\pi}} \sum_{k,l=0}^{\infty} \frac{e^{i(k-l)\theta}}{\sqrt{2^{k+l}} k!l!} H_{k+l}(X_\theta) \text{Tr}(a^{\dagger k} a^l \rho). \end{aligned} \quad (\text{B.10})$$

Using the orthonormality property of the Hermite polynomials together with the expression

$$\sum_{u=0}^n \exp(2\pi i u s / (n+1)) = (n+1) \delta_{s,0}, \quad (\text{B.11})$$

in Eq. (B.10) gives

$$\begin{aligned} \langle a^{\dagger k} a^l \rangle &= \text{Tr}(a^{\dagger k} a^l \rho) \\ &= C_{kl} \sum_{m=0}^{k+l} \exp\left(-i(k-l) \left(\frac{m\pi}{k+l+1}\right)\right) \\ &\quad \int_{-\infty}^{\infty} dX_\theta w\left(X_\theta, \frac{m\pi}{k+l+1}\right) H_{k+l}(X_\theta), \end{aligned} \quad (\text{B.12})$$

where

$$C_{kl} = \frac{k!l!}{(k+l+1)! \sqrt{2^{k+l}}}.$$

This procedure can be extended in a straightforward manner to multimode systems.

APPENDIX C

Numerical computation of the time-evolved density matrix of the bipartite BEC system

We outline the essential steps in computing the time-evolved density matrix of the double-well BEC system, for initial states $|\Psi_{m_1 m_2}\rangle = |\alpha_a, m_1\rangle \otimes |\alpha_b, m_2\rangle$ with Hamiltonian H_{BEC} (Eq. (2.21)). We denote the time-evolved density matrix by $\rho_{m_1, m_2}(t)$.

The procedure for obtaining $\rho_{0,0}(t)$ corresponding to the initial state $|\alpha_a\rangle \otimes |\alpha_b\rangle$ is outlined in [45]. We obtain [34] $\rho_{m_1, m_2}(t) = |\Psi_{m_1 m_2}(t)\rangle \langle \Psi_{m_1 m_2}(t)|$ from $\rho_{0,0}(t)$ through appropriate transformations. We first write

$$|\Psi_{m_1 m_2}(t)\rangle = M_{m_1, m_2}(t) |\Psi_{00}(t)\rangle, \quad (\text{C.1})$$

where

$$M_{m_1, m_2}(t) = \frac{1}{\mu} \exp(-iH_{\text{BEC}}t) a^{\dagger m_1} b^{\dagger m_2} \exp(iH_{\text{BEC}}t), \quad (\text{C.2})$$

and μ is given in terms of the Laguerre polynomials as $\sqrt{m_1! L_{m_1}(-|\alpha_a|^2) m_2! L_{m_2}(-|\alpha_b|^2)}$.

In order to recast $M_{m_1, m_2}(t)$ in a simpler form we introduce the operator $V = \exp(\kappa(a^\dagger b - b^\dagger a)/2)$, where $\kappa = \tan^{-1}(\lambda/\omega_1)$ [45]. Consequently, H_{BEC} can be written as $V \tilde{H}_{\text{BEC}} V^\dagger$, where

$$\tilde{H}_{\text{BEC}} = \omega_0 N_{\text{tot}} + \lambda_1 (a^\dagger a - b^\dagger b) + U N_{\text{tot}}^2, \quad (\text{C.3})$$

and $\lambda_1 = (\lambda^2 + \omega_1^2)^{1/2}$. Hence,

$$M_{m_1, m_2}(t) = \frac{1}{\mu} V \exp(-i\tilde{H}_{\text{BEC}}t) V^\dagger a^{\dagger m_1} b^{\dagger m_2} V \exp(i\tilde{H}_{\text{BEC}}t) V^\dagger. \quad (\text{C.4})$$

This expression can now be simplified using the following identities which can be ob-

tained in a straightforward manner by using the Baker-Hausdorff lemma.

$$V^\dagger a^\dagger V = a^\dagger \cos(\kappa/2) + b^\dagger \sin(\kappa/2), \quad (\text{C.5})$$

$$V^\dagger b^\dagger V = b^\dagger \cos(\kappa/2) - a^\dagger \sin(\kappa/2), \quad (\text{C.6})$$

$$V a^\dagger V^\dagger = a^\dagger \cos(\kappa/2) - b^\dagger \sin(\kappa/2), \quad (\text{C.7})$$

$$V b^\dagger V^\dagger = b^\dagger \cos(\kappa/2) + a^\dagger \sin(\kappa/2), \quad (\text{C.8})$$

$$\begin{aligned} \exp(-i\lambda_1(a^\dagger a - b^\dagger b)t) a^{\dagger p} b^{\dagger q} \exp(i\lambda_1(a^\dagger a - b^\dagger b)t) \\ = a^{\dagger p} b^{\dagger q} \exp(-i(p-q)\lambda_1 t), \end{aligned} \quad (\text{C.9})$$

$$\begin{aligned} \exp(-i\omega_0 N_{\text{tot}} t) a^{\dagger p} b^{\dagger q} \exp(i\omega_0 N_{\text{tot}} t) \\ = a^{\dagger p} b^{\dagger q} \exp(-i(p+q)\omega_0 t), \end{aligned} \quad (\text{C.10})$$

$$\begin{aligned} \exp(-iU N_{\text{tot}}^2 t) a^{\dagger p} b^{\dagger q} \exp(iU N_{\text{tot}}^2 t) \\ = a^{\dagger p} b^{\dagger q} \exp(-iUt(p+q)(2N_{\text{tot}} + p + q)). \end{aligned} \quad (\text{C.11})$$

Further, using binomial expansions for the two commuting operators a^\dagger and b^\dagger and defining $p_{\text{max}} = (k + m_2 - l)$ and $q_{\text{max}} = (l + m_1 - k)$, we arrive at the following simplified expression for $M_{m_1, m_2}(t)$.

$$\begin{aligned} M_{m_1, m_2}(t) = \frac{1}{\mu} \left[\sum_{k=0}^{m_1} \sum_{l=0}^{m_2} \sum_{p=0}^{p_{\text{max}}} \sum_{q=0}^{q_{\text{max}}} (-1)^{k-p} \binom{m_1}{k} \binom{m_2}{l} \right. \\ \left. \binom{p_{\text{max}}}{p} \binom{q_{\text{max}}}{q} \exp(-i\lambda_1 t(2(k-l) + m_2 - m_1)) \right. \\ \left. (\cos(\kappa/2))^{(k+l+p+q)} (\sin(\kappa/2))^{(2(m_1+m_2)-(k+l+p+q))} \right. \\ \left. a^{\dagger(p+q_{\text{max}}-q)} b^{\dagger(q+p_{\text{max}}-p)} \right] \exp(-i\omega_0 t(m_1 + m_2)) \\ \times \exp(-iUt(m_1 + m_2)(2N_{\text{tot}} + m_1 + m_2)). \end{aligned} \quad (\text{C.12})$$

The density matrix can now be expressed in terms of $M_{m_1, m_2}(t)$ and $\rho_{0,0}(t)$ as

$$\rho_{m_1, m_2}(t) = M_{m_1, m_2}(t) \rho_{0,0}(t) M_{m_1, m_2}^\dagger(t). \quad (\text{C.13})$$

APPENDIX D

Estimation of the maximal local Lyapunov exponent Λ_L

We outline the procedure to obtain the maximal local Lyapunov exponent Λ_L from a time series $\{y(t_n)\}$ ($n = 1, 2, \dots, N_0$). The underlying dynamical process is inherently nonlinear. The basic premise is that the ergodicity properties pertaining to the dynamics can be captured through a detailed time-series analysis. The first step is to reconstruct an effective phase space of dimension d_{emb} (the embedding dimension), in which the dynamics will be examined. For this purpose, a time delay τ_d is obtained such that data points separated by a time interval $\geq \tau_d$ can be treated as independent dynamical variables. This is done as follows. We note that for two data points $y(t_n)$ and $y(t_n + T)$ (T is any time duration such that $t_n + T \leq t_{N_0}$), the information about $y(t_n)$ that can be deduced from the measured value of $y(t_n + T)$ should tend to zero for sufficiently large T . Hence, if $p(y(t_n))$ and $p(y(t_n + T))$ are the individual probability densities for obtaining the values $y(t_n)$ and $y(t_n + T)$ respectively, and $p(y(t_n), y(t_n + T))$ is the corresponding joint probability density, the mutual information

$$I(T) = \sum_{y(t_n), y(t_n+T)} p(y(t_n), y(t_n + T)) \log_2 \left\{ \frac{p(y(t_n), y(t_n + T))}{p(y(t_n)) p(y(t_n + T))} \right\} \quad (\text{D.1})$$

should tend to zero, for sufficiently large T . A frequently used prescription is to choose τ_d to be the first minimum of $I(T)$ [97].

Using τ_d , d_{emb} is determined as follows. The next step is to examine the correlation integral

$$C(r) = \lim_{M_0 \rightarrow \infty} \frac{1}{M_0^2} \sum_{\substack{i,j=0 \\ i \neq j}}^{M_0} \Theta(r - \mu_{ij}) = \int_0^r d^d r' c(\mathbf{r}'), \quad (\text{D.2})$$

where,

$$\mu_{ij} = \left(\sum_{p=0}^{d-1} (y(t_i + p\tau_d) - y(t_j + p\tau_d))^2 \right)^{1/2},$$

and $\Theta(r - \mu_{ij})$ is the Heaviside function. $C(r)$ gives an estimate of the average correlation between M_0 points in a d -dimensional phase space and the integrand $c(\mathbf{r}')$ is the standard correlation function. Here M_0 is fixed such that $t_{M_0} + (d - 1)\tau_d \leq t_{N_0}$. If r

is sufficiently small, $C(r) \sim r^\ell$ [98]. $C(r)$ is calculated for various values of d . The embedding dimension d_{emb} is determined by the requirement that for any $d \geq d_{emb}$, ℓ remains constant.

Vectors in the reconstructed phase space are denoted by

$$\mathbf{y}(n) = [y(t_n), y(t_n + \tau_d), \dots, y(t_n + (d_{emb} - 1)\tau_d)]. \quad (\text{D.3})$$

The basic assumption is that the dynamics is guided by a map \mathbf{F} such that

$$\mathbf{y}(n+1) = \mathbf{F}(\mathbf{y}(n)). \quad (\text{D.4})$$

Of immediate relevance to us is the Jacobian

$$\mathbf{DF}_{ij}(\mathbf{y}(n)) = \frac{\partial \mathbf{F}_i(\mathbf{y}(n))}{\partial y_j(n)}, \quad (\text{D.5})$$

where $i, j = 0, 1, \dots, d_{emb} - 1$. Since the expression for \mathbf{F} is not a priori known explicitly, the Jacobian is obtained from the time series as follows [80]. For a given $\mathbf{y}(n)$, we find k nearest neighbours in the reconstructed phase space. They are denoted by $\{\mathbf{y}^{(1)}(n), \mathbf{y}^{(2)}(n), \dots, \mathbf{y}^{(k)}(n)\}$. Defining $\mathbf{D}\mathbf{y}^{(p)}(n) = \mathbf{y}^{(p)}(n) - \mathbf{y}(n)$ ($p = 1, 2, \dots, k$), it can be shown that,

$$\begin{aligned} \mathbf{F}_i(\mathbf{y}^{(p)}(n)) - \mathbf{F}_i(\mathbf{y}(n)) &= \mathbf{DF}_{ij}(\mathbf{y}(n))\mathbf{D}\mathbf{y}_j^{(p)}(n) \\ &+ \mathbf{Q}_{ilm}(\mathbf{y}(n))\mathbf{D}\mathbf{y}_l^{(p)}(n)\mathbf{D}\mathbf{y}_m^{(p)}(n) + \dots \end{aligned} \quad (\text{D.6})$$

where to second-order, $\mathbf{DF}_{ij}(\mathbf{y}(n))$ and $\mathbf{Q}_{ilm}(\mathbf{y}(n))$ need to be determined. We can numerically find them by solving the set of simultaneous linear equations (D.6). We note that the LHS of Eq. (D.6) can be determined using Eq. (D.4). We point out that k is fixed such that this set of equations is uniquely solved.

We now define,

$$\mathbf{DF}^L(n) = \mathbf{DF}(\mathbf{y}(n+L-1)) \cdot \mathbf{DF}(\mathbf{y}(n+L-2)) \cdots \mathbf{DF}(\mathbf{y}(n)). \quad (\text{D.7})$$

The Oseledec matrix \mathbf{M}_{os} can be expressed in terms of $\mathbf{DF}^L(n)$ as

$$\mathbf{M}_{\text{os}}(n, L) = \left((\mathbf{DF}^L(n))^T \cdot \mathbf{DF}^L(n) \right)^{1/(2L)}. \quad (\text{D.8})$$

The spectrum of local Lyapunov exponents corresponding to L steps of time are the eigenvalues of \mathbf{M}_{os} . Of direct relevance to us are the ergodicity properties of $d_1(t)$ (Eq. 4.2) that can be obtained from the corresponding time series. Hence, replacing $y(t_n)$ by $d_1(t_n)$ and setting $N_0 = 20000$, we have obtained τ_d and d_{emb} from the time series using the TISEAN package [81]. Using the procedure outlined above, the local Lyapunov exponents have been calculated. This procedure has been repeated for 100 randomly chosen values of n in the time series and the average Λ_L of the corresponding maximal local Lyapunov exponents has been calculated.

The global Lyapunov exponents are the eigenvalues of $\lim_{L \rightarrow \infty} \mathbf{M}_{\text{os}}(n, L)$. We denote the maximal global Lyapunov exponent by Λ_∞ . Then, for generic dynamical systems, it has been shown [99, 80] that Λ_L tends to $\Lambda_\infty + (m/L^q)$ (m, q : constants), for sufficiently large L .

APPENDIX E

The 2-photon frequency combs

In Section 4.5, the expressions for the two 2-photon states $|\Psi_\alpha\rangle$ and $|\Psi_\beta\rangle$ which are distinguished from each other using tomograms are given in Eqs. (4.7) and (4.10) respectively. For convenience, we give the expressions below.

$$|\Psi_\alpha\rangle = \mathcal{N}_\alpha^{-1/2} \int d\omega_s \int d\omega_i f_+(\omega_s + \omega_i) f_-(\Omega) f_{\text{cav}}(\omega_s) f_{\text{cav}}(\omega_i) |\omega_s\rangle \otimes |\omega_i\rangle ,$$

where \mathcal{N}_α is the normalisation constant. Here, $f_-(\Omega)$ and $f_{\text{cav}}(\omega)$ are defined in Eqs. (4.8) and (4.9) respectively. The other 2-photon state

$$|\Psi_\beta\rangle = \mathcal{N}_\beta^{-1/2} \int d\omega_s \int d\omega_i f_+(\omega_s + \omega_i) f_-(\Omega) g_{\text{cav}}(\omega_s) f_{\text{cav}}(\omega_i) |\omega_s\rangle \otimes |\omega_i\rangle ,$$

where $g_{\text{cav}}(\omega)$ is defined in Eq. (4.11), and \mathcal{N}_β is the normalisation constant.

In what follows, we outline the procedure to show that these two states are indeed the two states which were shown to be distinguishable using photon coincidence counts, in the experiment reported in [28].

In the experimental setup, the sum of the frequencies of the signal and the idler photons matches the pump frequency, i.e., $(\omega_s + \omega_i = \omega_p)$. Hence, as stated in the supplementary material of [28], $f_+(\omega_s + \omega_i)$ can be replaced by $\delta(\omega_s + \omega_i - \omega_p)$. Integrating over the variable $\Omega_+ (= \omega_s + \omega_i)$, appropriately changing the integration variables, noting that $\Omega = \omega_s - \omega_i$, and dropping the normalisation constant, we get

$$|\Psi_\alpha\rangle = \int d\Omega f_-(\Omega) f_{\text{cav}}(\omega_s) f_{\text{cav}}(\omega_i) |\omega_s\rangle \otimes |\omega_i\rangle . \quad (\text{E.1})$$

This can be identified as one of the states considered in the experiment, namely, Eq. (B19) in [28], on changing the notation from $\Omega, \omega_s, \omega_i$ in Eq. (E.1) to $\omega_-, \omega_s, \omega_i$ respectively.

We now proceed to establish that the other 2-photon state $|\Psi_\beta\rangle$ considered by us, is the same as the state $|\psi'\rangle$ ($= C' Z_{t_s} |\tilde{+}\rangle_{\omega_s} \otimes |\tilde{+}\rangle_{\omega_i}$) defined in [28]. Here, $C' |t_s; t_i\rangle = |t_s + t_i; t_s - t_i\rangle$ where, for instance, $|t_s\rangle \otimes |t_i\rangle$ is denoted by $|t_s; t_i\rangle$ with t_s and t_i being

the time variables associated with the signal and the idler photons respectively, and $Z_{t_s} |\tilde{+}\rangle_{\omega_s} = |\tilde{-}\rangle_{\omega_s}$. It is convenient to express $|\tilde{+}\rangle_{\omega_x}$ and $|\tilde{-}\rangle_{\omega_x}$ ($x = s, i$) as

$$|\tilde{+}\rangle_{\omega_x} = \int d\omega_x \int dt_x \exp\left(-\frac{t_x^2}{2\kappa_x^2} - \frac{\omega_x^2}{2(\Delta\omega)^2}\right) \sum_n e^{i(\omega_x + n\bar{\omega})t_x} |\omega_x + n\bar{\omega}\rangle, \quad (\text{E.2})$$

and,

$$|\tilde{-}\rangle_{\omega_x} = \int d\omega_x \int dt_x \exp\left(-\frac{t_x^2}{2\kappa_x^2} - \frac{\omega_x^2}{2(\Delta\omega)^2}\right) \sum_n (-1)^n e^{i(\omega_x + n\bar{\omega})t_x} |\omega_x + n\bar{\omega}\rangle. \quad (\text{E.3})$$

These expressions follow from the properties of the displacement operator, and Eqs. (B1), (B2), (B7) given in [28]. Here, κ_x ($x = s, i$) is the standard deviation in t_x . It follows from Eqs. (E.2) and (E.3) that

$$|\psi'\rangle = \int dt \int dt' \int d\omega \int d\omega' \exp\left(-\frac{t^2(\Delta\omega_p)^2 + t'^2(\Delta\Omega)^2}{2} - \frac{\omega^2 + \omega'^2}{2(\Delta\omega)^2}\right) \sum_{n,m} (-1)^n e^{i(n\bar{\omega} + \omega)(t+t')} e^{i(m\bar{\omega} + \omega')(t-t')} |n\bar{\omega} + \omega\rangle \otimes |m\bar{\omega} + \omega'\rangle, \quad (\text{E.4})$$

where $\Delta\omega_p$ is the standard deviation in ω_p . Integrating over the time variables t and t' , writing $(\omega_s = n\bar{\omega} + \omega)$, $(\omega_i = m\bar{\omega} + \omega')$ where n, m are integers, and using the fact that f_+ is a Gaussian function with a standard deviation $\Delta\omega_p$ ($\Delta\omega_p \ll \Delta\Omega$), it is straightforward to see that Eq. (E.4) can be expressed as $|\Psi_\beta\rangle$ (Eq. (4.10)) unnormalised.

APPENDIX F

Expressions for the chronocyclic tomograms

We are interested in the time-time slice of the tomograms corresponding to $|\Psi_\alpha\rangle$ (Eq. (4.7)) and $|\Psi_\beta\rangle$ (Eq. (4.10)). As a first step, we calculate the explicit expressions for the states $|\Psi_\alpha\rangle$ and $|\Psi_\beta\rangle$ in the Fourier transform basis (i.e., time-time basis) using $f_+(\omega_s + \omega_1) = \delta(\omega_s + \omega_1 - \omega_p)$ in Eqs. (4.7) and (4.10). The 2-photon state $|\Psi_\alpha\rangle$ in the time-time basis is given by

$$|\Psi_\alpha\rangle = \frac{1}{\sqrt{\mathcal{M}_\alpha \tau_P}} \int dt_s \int dt_1 \exp \left(-\frac{(t_1 - t_s)^2 (\Delta\omega)^2 (\Delta\Omega)^2}{4 ((\Delta\omega)^2 + (\Delta\Omega)^2)} \right) \times [\mathcal{F}(t_1 - t_s)]^2 |t_s; t_1\rangle, \quad (\text{F.1})$$

and the time-time slice $w^\alpha(t_s; t_1)$ corresponding to $|\Psi_\alpha\rangle$ is

$$w^\alpha(t_s; t_1) = \frac{1}{\mathcal{M}_\alpha \tau_P} \exp \left(-\frac{(t_1 - t_s)^2 (\Delta\omega)^2 (\Delta\Omega)^2}{2 ((\Delta\omega)^2 + (\Delta\Omega)^2)} \right) |\mathcal{F}(t_1 - t_s)|^4,$$

where $\tau_P = 1\text{s}$ (introduced for dimensional purposes),

$$\mathcal{F}(t_1 - t_s) = \sum_n \exp \left(\frac{i(t_1 - t_s) n \bar{\omega} (\Delta\Omega)^2}{2 ((\Delta\omega)^2 + (\Delta\Omega)^2)} \right),$$

and the normalisation constant is

$$\mathcal{M}_\alpha = \frac{\pi}{\mu_0} \sum_{m, n, m', n'} \exp \left(-\frac{(n - n' + m' - m)^2 \bar{\omega}^2 (\Delta\Omega)^2}{2 (\Delta\omega)^2 ((\Delta\omega)^2 + (\Delta\Omega)^2)} \right), \quad (\text{F.2})$$

where $\mu_0 = \left(\frac{\pi (\Delta\Omega)^2 (\Delta\omega)^2}{2 ((\Delta\Omega)^2 + (\Delta\omega)^2)} \right)^{1/2}$.

Similarly, the other 2-photon state $|\Psi_\beta\rangle$ in the time-time basis is given by

$$|\Psi_\beta\rangle = \frac{1}{\sqrt{\mathcal{M}_\beta \tau_P}} \int dt_s \int dt_1 \exp \left(-\frac{(t_1 - t_s)^2 (\Delta\omega)^2 (\Delta\Omega)^2}{4 ((\Delta\omega)^2 + (\Delta\Omega)^2)} \right) \times \mathcal{G}(t_1 - t_s) \mathcal{F}(t_1 - t_s) |t_s; t_1\rangle, \quad (\text{F.3})$$

and the time-time slice corresponding to $|\Psi_\beta\rangle$ is

$$w^\beta(t_s; t_1) = \frac{1}{\mathcal{M}_\beta \tau_P} \exp \left(-\frac{(t_1 - t_s)^2 (\Delta\omega)^2 (\Delta\Omega)^2}{2 ((\Delta\omega)^2 + (\Delta\Omega)^2)} \right) \left| \mathcal{G}(t_1 - t_s) \mathcal{F}(t_1 - t_s) \right|^2,$$

where,

$$\mathcal{G}(t_1 - t_s) = \sum_n (-1)^n \exp \left(\frac{i(t_1 - t_s) n \bar{\omega} (\Delta\Omega)^2}{2 ((\Delta\omega)^2 + (\Delta\Omega)^2)} \right),$$

and the normalisation constant \mathcal{M}_β is essentially the same as \mathcal{M}_α with an extra factor of $(-1)^{n+n'}$ within the summation in Eq. (F.2).

REFERENCES

- [1] K. Bartkiewicz, A. Černoč, K. Lemr, and A. Miranowicz. *Priority choice experimental two-qubit tomography: Measuring one by one all elements of density matrices*. Sci. Rep. **6**, 19610 (2016). URL <https://doi.org/10.1038/srep19610>.
- [2] Z. Hou, H.-S. Zhong, Y. Tian, D. Dong, B. Qi, L. Li, Y. Wang, F. Nori, G.-Y. Xiang, C.-F. Li, and G.-C. Guo. *Full reconstruction of a 14-qubit state within four hours*. New J. Phys. **18**, 083036 (2016). URL <https://doi.org/10.1088%2F1367-2630%2F18%2F8%2F083036>.
- [3] T. Baumgratz, A. Nijßeler, M. Cramer, and M. B. Plenio. *A scalable maximum likelihood method for quantum state tomography*. New J. Phys. **15**, 125004 (2013). URL <https://doi.org/10.1088%2F1367-2630%2F15%2F12%2F125004>.
- [4] J. G. Titchener, M. Gräfe, R. Heilmann, A. S. Solntsev, A. Szameit, and A. A. Sukhorukov. *Scalable on-chip quantum state tomography*. npj Quantum Inf. **4**, 19 (2018). URL <https://doi.org/10.1038/s41534-018-0063-5>.
- [5] X. Li, J. Shang, H. K. Ng, and B.-G. Englert. *Optimal error intervals for properties of the quantum state*. Phys. Rev. A **94**, 062112 (2016). URL <https://link.aps.org/doi/10.1103/PhysRevA.94.062112>.
- [6] A. K. Ekert, C. M. Alves, D. K. L. Oi, M. Horodecki, P. Horodecki, and L. C. Kwek. *Direct estimations of linear and nonlinear functionalities of a quantum state*. Phys. Rev. Lett. **88**, 217901 (2002). URL <https://link.aps.org/doi/10.1103/PhysRevLett.88.217901>.
- [7] P. Horodecki and A. Ekert. *Method for direct detection of quantum entanglement*. Phys. Rev. Lett. **89**, 127902 (2002). URL <https://link.aps.org/doi/10.1103/PhysRevLett.89.127902>.
- [8] F. A. Bovino, G. Castagnoli, A. Ekert, P. Horodecki, C. M. Alves, and A. V. Sergienko. *Direct measurement of nonlinear properties of bipartite quantum states*. Phys. Rev. Lett. **95**, 240407 (2005). URL <https://link.aps.org/doi/10.1103/PhysRevLett.95.240407>.
- [9] R. Blume-Kohout, J. O. S. Yin, and S. J. van Enk. *Entanglement verification with finite data*. Phys. Rev. Lett. **105**, 170501 (2010). URL <https://link.aps.org/doi/10.1103/PhysRevLett.105.170501>.
- [10] K. Vogel and H. Risken. *Determination of quasiprobability distributions in terms of probability distributions for the rotated quadrature phase*. Phys. Rev. A **40**, 2847 (1989). URL <http://link.aps.org/doi/10.1103/PhysRevA.40.2847>.

- [11] A. Ibort, V. I. Man'ko, G. Marmo, A. Simoni, and F. Ventriglia. *An introduction to the tomographic picture of quantum mechanics*. Phys. Scripta **79**, 065013 (2009). URL <http://stacks.iop.org/1402-4896/79/i=6/a=065013>.
- [12] A. I. Lvovsky and M. G. Raymer. *Continuous-variable optical quantum-state tomography*. Rev. Mod. Phys. **81**, 299 (2009). URL <http://link.aps.org/doi/10.1103/RevModPhys.81.299>.
- [13] D. Lv, S. An, M. Um, J. Zhang, J.-N. Zhang, M. S. Kim, and K. Kim. *Reconstruction of the Jaynes-Cummings field state of ionic motion in a harmonic trap*. Phys. Rev. A **95**, 043813 (2017). URL <https://link.aps.org/doi/10.1103/PhysRevA.95.043813>.
- [14] I. Averbukh and N. Perelman. *Fractional revivals: Universality in the long-term evolution of quantum wave packets beyond the correspondence principle dynamics*. Phys. Lett. A **139**, 449 (1989). URL <http://www.sciencedirect.com/science/article/pii/037596018990943>.
- [15] R. Robinett. *Quantum wave packet revivals*. Phys. Rep. **392**, 1 (2004). URL <http://www.sciencedirect.com/science/article/pii/S037015730300043>.
- [16] K. Tara, G. S. Agarwal, and S. Chaturvedi. *Production of Schrödinger macroscopic quantum-superposition states in a Kerr medium*. Phys. Rev. A **47**, 5024 (1993). URL <http://link.aps.org/doi/10.1103/PhysRevA.47.5024>.
- [17] M. Rohith and C. Sudheesh. *Visualizing revivals and fractional revivals in a Kerr medium using an optical tomogram*. Phys. Rev. A **92**, 053828 (2015). URL <http://link.aps.org/doi/10.1103/PhysRevA.92.053828>.
- [18] G. S. Agarwal and J. Banerji. *Fractional revivals in systems with two time scales*. Phys. Rev. A **57**, 3880 (1998). URL <http://link.aps.org/doi/10.1103/PhysRevA.57.3880>.
- [19] R. Bluhm and V. A. Kostelecký. *Long-term evolution and revival structure of Rydberg wave packets for hydrogen and alkali-metal atoms*. Phys. Rev. A **51**, 4767 (1995). URL <http://link.aps.org/doi/10.1103/PhysRevA.51.4767>.
- [20] S. J. Seltzer, P. J. Meares, and M. V. Romalis. *Synchronous optical pumping of quantum revival beats for atomic magnetometry*. Phys. Rev. A **75**, 051407 (2007). URL <http://link.aps.org/doi/10.1103/PhysRevA.75.051407>.
- [21] C. K. Hong and L. Mandel. *Higher-order squeezing of a quantum field*. Phys. Rev. Lett. **54**, 323 (1985). URL <https://link.aps.org/doi/10.1103/PhysRevLett.54.323>.
- [22] M. Hillery. *Amplitude-squared squeezing of the electromagnetic field*. Phys. Rev. A **36**, 3796 (1987). URL <http://link.aps.org/doi/10.1103/PhysRevA.36.3796>.
- [23] A. Wünsche. *Tomographic reconstruction of the density operator from its normally ordered moments*. Phys. Rev. A **54**, 5291 (1996). URL <http://link.aps.org/doi/10.1103/PhysRevA.54.5291>.

- [24] I. Białynicki-Birula and J. Mycielski. *Uncertainty relations for information entropy in wave mechanics*. Commun. Math. Phys. **44**, 129 (1975). URL <https://doi.org/10.1007/BF01608825>.
- [25] T. Yu and J. Eberly. *Sudden death of entanglement*. Science **323**, 598 (2009). URL <https://doi.org/10.1126/science.1167343>.
- [26] P. Laha, B. Sudarsan, S. Lakshmibala, and V. Balakrishnan. *Entanglement dynamics in a model tripartite quantum system*. Int. J. Theor. Phys. **55**, 4044 (2016). URL <https://doi.org/10.1007/s10773-016-3033-8>.
- [27] M. Rohith and C. Sudheesh. *Signatures of entanglement in an optical tomogram*. J. Opt. Soc. Am. B **33**, 126 (2016). URL <http://josab.osa.org/abstract.cfm?URI=josab-33-2-126>.
- [28] N. Fabre, G. Maltese, F. Appas, S. Felicetti, A. Ketterer, A. Keller, T. Coudreau, F. Baboux, M. I. Amanti, S. Ducci, and P. Milman. *Generation of a time-frequency grid state with integrated biphoton frequency combs*. Phys. Rev. A **102**, 012607 (2020). URL <https://link.aps.org/doi/10.1103/PhysRevA.102.012607>.
- [29] J. Paye. *The chronocyclic representation of ultrashort light pulses*. IEEE J. Quantum Elect. **28**, 2262 (1992). URL <https://ieeexplore.ieee.org/document/159533>.
- [30] S. Pal, P. Batra, T. Paterek, and T. Mahesh. *Experimental localisation of quantum entanglement through monitored classical mediator*. arXiv preprint arXiv:1909.11030 (2019).
- [31] A. Zavatta, S. Viciani, and M. Bellini. *Single-photon excitation of a coherent state: Catching the elementary step of stimulated light emission*. Phys. Rev. A **72**, 023820 (2005). URL <http://link.aps.org/doi/10.1103/PhysRevA.72.023820>.
- [32] D. Stoler, B. E. A. Saleh, and M. C. Teich. *Binomial states of the quantized radiation field*. Optica Acta **32**, 345 (1985). URL <https://doi.org/10.1080/713821735>.
- [33] C. M. Caves and B. L. Schumaker. *New formalism for two-photon quantum optics. I. Quadrature phases and squeezed states*. Phys. Rev. A **31**, 3068 (1985). URL <https://link.aps.org/doi/10.1103/PhysRevA.31.3068>.
- [34] B. Sharmila, K. Saumitran, S. Lakshmibala, and V. Balakrishnan. *Signatures of nonclassical effects in optical tomograms*. J. Phys. B: At. Mol. Opt. **50**, 045501 (2017). URL <https://doi.org/10.1088/1361-6455/aa51a4>.
- [35] B. Sharmila, S. Lakshmibala, and V. Balakrishnan. *Signatures of avoided energy-level crossings in entanglement indicators obtained from quantum tomograms*. arXiv preprint arXiv:2006.13536 (2020).
- [36] B. Sharmila, S. Lakshmibala, and V. Balakrishnan. *Estimation of entanglement in bipartite systems directly from tomograms*. Quantum Inf. Process. **18**, 236 (2019). URL <https://doi.org/10.1007/s11128-019-2352-0>.

- [37] B. Sharmila, S. Lakshmibala, and V. Balakrishnan. *Tomographic entanglement indicators in multipartite systems*. Quantum Inf. Process. **19**, 127 (2020). URL <https://doi.org/10.1007/s11128-020-02625-5>.
- [38] S. N. Filippov and V. I. Man'ko. *Optical tomography of Fock state superpositions*. Phys. Scripta **83**, 058101 (2011). URL <http://stacks.iop.org/1402-4896/83/i=5/a=058101>.
- [39] G. Kirchmair, B. Vlastakis, Z. Leghtas, S. E. Nigg, H. Paik, E. Ginossar, M. Mirrahimi, L. Frunzio, S. M. Girvin, and R. J. Schoelkopf. *Observation of quantum state collapse and revival due to the single-photon Kerr effect*. Nature **495**, 205 (2013). URL <https://doi.org/10.1038/nature11902>.
- [40] Z. Leghtas, S. Touzard, I. M. Pop, A. Kou, B. Vlastakis, A. Petrenko, K. M. Sliwa, A. Narla, S. Shankar, M. J. Hatridge, M. Reagor, L. Frunzio, R. J. Schoelkopf, M. Mirrahimi, and M. H. Devoret. *Confining the state of light to a quantum manifold by engineered two-photon loss*. Science **347**, 853 (2015). URL <https://science.sciencemag.org/content/347/6224/853>.
- [41] E. T. Holland, B. Vlastakis, R. W. Heeres, M. J. Reagor, U. Vool, Z. Leghtas, L. Frunzio, G. Kirchmair, M. H. Devoret, M. Mirrahimi, and R. J. Schoelkopf. *Single-photon-resolved cross-Kerr interaction for autonomous stabilization of photon-number states*. Phys. Rev. Lett. **115**, 180501 (2015). URL <https://link.aps.org/doi/10.1103/PhysRevLett.115.180501>.
- [42] M. Reagor, W. Pfaff, C. Axline, R. W. Heeres, N. Ofek, K. Sliwa, E. Holland, C. Wang, J. Blumoff, K. Chou, M. J. Hatridge, L. Frunzio, M. H. Devoret, L. Jiang, and R. J. Schoelkopf. *Quantum memory with millisecond coherence in circuit QED*. Phys. Rev. B **94**, 014506 (2016). URL <https://link.aps.org/doi/10.1103/PhysRevB.94.014506>.
- [43] A. Biswas and G. S. Agarwal. *Nonclassicality and decoherence of photon-subtracted squeezed states*. Phys. Rev. A **75**, 032104 (2007). URL <http://link.aps.org/doi/10.1103/PhysRevA.75.032104>.
- [44] C. Sudheesh, S. Lakshmibala, and V. Balakrishnan. *Squeezing and higher-order squeezing of photon-added coherent states propagating in a Kerr-like medium*. J. Opt. B: Quantum S. O. **7**, S728 (2005). URL <http://stacks.iop.org/1464-4266/7/i=12/a=040>.
- [45] L. Sanz, M. H. Y. Moussa, and K. Furuya. *Generation of generalized coherent states with two coupled Bose-Einstein condensates*. Ann. Phys. (N.Y.) **321**, 1206 (2006). URL <http://www.sciencedirect.com/science/article/pii/S00034916050015>.
- [46] L.-M. Kuang, F.-B. Wang, and Y.-G. Zhou. *Coherent states of a harmonic oscillator in a finite-dimensional Hilbert space and their squeezing properties*. J. Mod. Opt. **41**, 1307 (1994). URL <http://dx.doi.org/10.1080/09500349414551261>.
- [47] A. Orłowski. *Information entropy and squeezing of quantum fluctuations*. Phys. Rev. A **56**, 2545 (1997). URL <http://link.aps.org/doi/10.1103/PhysRevA.56.2545>.

- [48] M. A. Nielsen and I. L. Chuang. *Quantum Computation and Quantum Information*. Cambridge University Press, Cambridge (2010).
- [49] G. Vidal, J. I. Latorre, E. Rico, and A. Kitaev. *Entanglement in quantum critical phenomena*. Phys. Rev. Lett. **90**, 227902 (2003). URL <https://link.aps.org/doi/10.1103/PhysRevLett.90.227902>.
- [50] J. Karthik, A. Sharma, and A. Lakshminarayan. *Entanglement, avoided crossings, and quantum chaos in an Ising model with a tilted magnetic field*. Phys. Rev. A **75**, 022304 (2007). URL <https://link.aps.org/doi/10.1103/PhysRevA.75.022304>.
- [51] S. Oh, Z. Huang, U. Peskin, and S. Kais. *Entanglement, Berry phases, and level crossings for the atomic Breit-Rabi Hamiltonian*. Phys. Rev. A **78**, 062106 (2008). URL <https://link.aps.org/doi/10.1103/PhysRevA.78.062106>.
- [52] O. Bohigas, M. J. Giannoni, and C. Schmit. *Characterization of chaotic quantum spectra and universality of level fluctuation laws*. Phys. Rev. Lett. **52**, 1 (1984). URL <https://link.aps.org/doi/10.1103/PhysRevLett.52.1>.
- [53] F. Haake. *Quantum Signatures of Chaos*. Springer, Berlin (2010).
- [54] P. Cejnar and J. Jolie. *Quantum phase transitions studied within the interacting boson model*. Phys. Rev. E **61**, 6237 (2000). URL <https://link.aps.org/doi/10.1103/PhysRevE.61.6237>.
- [55] W. D. Heiss. *The physics of exceptional points*. J. Phys. A: Math. Theor. **45**, 444016 (2012). URL <https://doi.org/10.1088%2F1751-8113%2F45%2F44%2F444016>.
- [56] M. S. Santhanam, V. B. Sheorey, and A. Lakshminarayan. *Effect of classical bifurcations on the quantum entanglement of two coupled quartic oscillators*. Phys. Rev. E **77**, 026213 (2008). URL <https://link.aps.org/doi/10.1103/PhysRevE.77.026213>.
- [57] M. S. Santhanam, V. B. Sheorey, and A. Lakshminarayan. *Chaos and localization in coupled quartic oscillators*. Pramana **48**, 439 (1997). URL <https://doi.org/10.1007/BF02845655>.
- [58] M. Pyzh, S. Krönke, C. Weitenberg, and P. Schmelcher. *Spectral properties and breathing dynamics of a few-body Bose–Bose mixture in a 1D harmonic trap*. New J. Phys. **20**, 015006 (2018). URL <https://doi.org/10.1088%2F1367-2630%2Faa9cb2>.
- [59] J. M. Hutson, E. Tiesinga, and P. S. Julienne. *Avoided crossings between bound states of ultracold cesium dimers*. Phys. Rev. A **78**, 052703 (2008). URL <https://link.aps.org/doi/10.1103/PhysRevA.78.052703>.
- [60] C. Dembowski, H.-D. Gräf, H. L. Harney, A. Heine, W. D. Heiss, H. Rehfeld, and A. Richter. *Experimental observation of the topological structure of exceptional points*. Phys. Rev. Lett. **86**, 787 (2001). URL <https://link.aps.org/doi/10.1103/PhysRevLett.86.787>.

- [61] I. Barke, F. Zheng, T. K. Rügheimer, and F. J. Himpsel. *Experimental evidence for spin-split bands in a one-dimensional chain structure.* Phys. Rev. Lett. **97**, 226405 (2006). URL <https://link.aps.org/doi/10.1103/PhysRevLett.97.226405>.
- [62] G. S. Agarwal and R. R. Puri. *Collapse and revival phenomenon in the evolution of a resonant field in a Kerr-like medium.* Phys. Rev. A **39**, 2969 (1989). URL <https://link.aps.org/doi/10.1103/PhysRevA.39.2969>.
- [63] P. Macha, G. Oelsner, J.-M. Reiner, M. Marthaler, S. André, G. Schön, U. Hübner, H.-G. Meyer, E. Il'ichev, and A. V. Ustinov. *Implementation of a quantum metamaterial using superconducting qubits.* Nat. Commun. **5**, 5146 (2014). URL <https://doi.org/10.1038/ncomms6146>.
- [64] D. S. Shapiro, P. Macha, A. N. Rubtsov, and A. V. Ustinov. *Dispersive response of a disordered superconducting quantum metamaterial.* Photonics **2**, 449 (2015). URL <https://www.mdpi.com/2304-6732/2/2/449>.
- [65] M. Tavis and F. W. Cummings. *Exact solution for an N -molecule—radiation-field Hamiltonian.* Phys. Rev. **170**, 379 (1968). URL <https://link.aps.org/doi/10.1103/PhysRev.170.379>.
- [66] L. Viola and W. G. Brown. *Generalized entanglement as a framework for complex quantum systems: Purity versus delocalization measures.* J. Phys. A: Math. Theor. **40**, 8109 (2007). URL <http://stacks.iop.org/1751-8121/40/i=28/a=S17>.
- [67] R. Smith. *A mutual information approach to calculating nonlinearity.* Stat **4**, 291 (2015). URL <https://onlinelibrary.wiley.com/doi/abs/10.1002/sta4.96>.
- [68] G. Masada and A. Furusawa. *On-chip continuous-variable quantum entanglement.* Nanophotonics **5**, 469 (2016). URL <https://www.degruyter.com/view/journals/nanoph/5/3/article-p469>.
- [69] T. M. Cover and J. A. Thomas. *Elements of Information Theory.* Wiley-Interscience, Hoboken (2006).
- [70] S. Kullback and R. A. Leibler. *On information and sufficiency.* Ann. Math. Stat. **22**, 79 (1951). URL <https://doi.org/10.1214/aoms/1177729694>.
- [71] C. Bishop. *Pattern Recognition and Machine Learning.* Springer, New York (2006).
- [72] T. Kailath. *The divergence and Bhattacharyya distance measures in signal selection.* IEEE T. Commun. Techn. **15**, 52 (1967). URL <https://doi.org/10.1109/TCOM.1967.1089532>.
- [73] R. T. Thew, K. Nemoto, A. G. White, and W. J. Munro. *Qudit quantum-state tomography.* Phys. Rev. A **66**, 012303 (2002). URL <https://link.aps.org/doi/10.1103/PhysRevA.66.012303>.
- [74] C. A. Trugenberger. *Probabilistic Quantum Memories.* Phys. Rev. Lett. **87**, 067901 (2001). URL <https://link.aps.org/doi/10.1103/PhysRevLett.87.067901>.

- [75] S. Weigert and M. Wilkinson. *Mutually unbiased bases for continuous variables*. Phys. Rev. A **78**, 020303 (2008). URL <https://link.aps.org/doi/10.1103/PhysRevA.78.020303>.
- [76] C. Sudheesh, S. Lakshmibala, and V. Balakrishnan. *Manifestations of wave packet revivals in the moments of observables*. Phys. Lett. A **329**, 14 (2004). URL <http://www.sciencedirect.com/science/article/pii/S03759601040091>
- [77] W. G. Brown, L. F. Santos, D. J. Starling, and L. Viola. *Quantum chaos, delocalization, and entanglement in disordered Heisenberg models*. Phys. Rev. E **77**, 021106 (2008). URL <https://link.aps.org/doi/10.1103/PhysRevE.77.021106>.
- [78] H. D. I. Abarbanel. *Analysis of Observed Chaotic Data*. Springer, New York (1996).
- [79] P. Grassberger and I. Procaccia. *Characterization of strange attractors*. Phys. Rev. Lett. **50**, 346 (1983). URL <https://link.aps.org/doi/10.1103/PhysRevLett.50.346>.
- [80] H. D. I. Abarbanel, R. Brown, and M. B. Kennel. *Local Lyapunov exponents computed from observed data*. J. Nonlinear Sci. **2**, 343 (1992). URL <https://doi.org/10.1007/BF01208929>.
- [81] R. Hegger, H. Kantz, and T. Schreiber. *Practical implementation of nonlinear time series methods: The TISEAN package*. Chaos **9**, 413 (1999). URL <https://doi.org/10.1063/1.166424>.
- [82] D. Gottesman, A. Kitaev, and J. Preskill. *Encoding a qubit in an oscillator*. Phys. Rev. A **64**, 012310 (2001). URL <https://link.aps.org/doi/10.1103/PhysRevA.64.012310>.
- [83] M. Beck, M. G. Raymer, I. A. Walmsley, and V. Wong. *Chronocyclic tomography for measuring the amplitude and phase structure of optical pulses*. Opt. Lett. **18**, 2041 (1993). URL <http://ol.osa.org/abstract.cfm?URI=ol-18-23-2041>.
- [84] T. Opatrný and D.-G. Welsch. *Density-matrix reconstruction by unbalanced homodyning*. Phys. Rev. A **55**, 1462 (1997). URL <https://link.aps.org/doi/10.1103/PhysRevA.55.1462>.
- [85] G. Brida, M. Genovese, M. Gramegna, P. Traina, E. Predazzi, S. Olivares, and M. Paris. *Toward a full reconstruction of density matrix by on/off measurements*. Int. J. Quantum Inf. **7**, 27 (2009). URL <https://doi.org/10.1142/S0219749909004888>.
- [86] R. Nehra, A. Win, M. Eaton, R. Shahrokhshahi, N. Sridhar, T. Gerrits, A. Lita, S. W. Nam, and O. Pfister. *State-independent quantum state tomography by photon-number-resolving measurements*. Optica **6**, 1356 (2019). URL <http://www.osapublishing.org/optica/abstract.cfm?URI=optica-6-10>
- [87] Z. X. Man, Y. J. Xia, and N. B. An. *Entanglement dynamics for the double Tavis-Cummings model*. Eur. Phys. J. D. **53**, 229 (2009). URL <https://doi.org/10.1140/epjd/e2009-00095-7>.

- [88] W. Vogel and R. L. d. M. Filho. *Nonlinear Jaynes-Cummings dynamics of a trapped ion*. Phys. Rev. A **52**, 4214 (1995). URL <https://link.aps.org/doi/10.1103/PhysRevA.52.4214>.
- [89] F. Deppe, M. Mariani, E. Menzel, A. Marx, S. Saito, K. Kakuyanagi, H. Tanaka, T. Meno, K. Semba, H. Takayanagi, E. Solano, and R. Gross. *Two-photon probe of the Jaynes-Cummings model and controlled symmetry breaking in circuit QED*. Nat. Phys. **4**, 686 (2008). URL <https://doi.org/10.1038/nphys1016>.
- [90] A. Retzker, E. Solano, and B. Reznik. *Tavis-Cummings model and collective multiqubit entanglement in trapped ions*. Phys. Rev. A **75**, 022312 (2007). URL <https://link.aps.org/doi/10.1103/PhysRevA.75.022312>.
- [91] *IBM Q: Documentation and support*. <https://quantum-computing.ibm.com/support>
- [92] *Qiskit: An open-source framework for quantum computing*. <https://qiskit.org>.
- [93] J. Ma, X. Wang, C. Sun, and F. Nori. *Quantum spin squeezing*. Phys. Rep. **509**, 89 (2011). URL <http://www.sciencedirect.com/science/article/pii/S03701573110022>
- [94] M. Kitagawa and M. Ueda. *Squeezed spin states*. Phys. Rev. A **47**, 5138 (1993). URL <https://link.aps.org/doi/10.1103/PhysRevA.47.5138>.
- [95] H. Maassen and J. B. M. Uffink. *Generalized entropic uncertainty relations*. Phys. Rev. Lett. **60**, 1103 (1988). URL <https://link.aps.org/doi/10.1103/PhysRevLett.60.1103>.
- [96] S. M. Barnett and P. M. Radmore. *Methods in Theoretical Quantum Optics*. Clarendon Press, Oxford (1997).
- [97] A. M. Fraser and H. L. Swinney. *Independent coordinates for strange attractors from mutual information*. Phys. Rev. A **33**, 1134 (1986). URL <https://link.aps.org/doi/10.1103/PhysRevA.33.1134>.
- [98] P. Grassberger and I. Procaccia. *Measuring the strangeness of strange attractors*. Physica D **9**, 189 (1983). URL <http://www.sciencedirect.com/science/article/pii/016727898390298>
- [99] H. D. Abarbanel, R. Brown, and M. B. Kennel. *Variation of Lyapunov exponents on a strange attractor*. J. Nonlinear Sci. **1**, 175 (1991). URL <https://doi.org/10.1007/BF01209065>.

LIST OF PAPERS BASED ON THESIS

Papers in refereed journals

1. Signatures of nonclassical effects in optical tomograms,
B. Sharmila, K. Saumitran, S. Lakshmibala, and V. Balakrishnan
J. Phys. B.: At. Mol. Opt. Phys. **50**, 045501 (2017).
2. Estimation of entanglement in bipartite systems directly from tomograms,
B. Sharmila, S. Lakshmibala, and V. Balakrishnan
Quantum Inf. Process. **18**, 236 (2019).
3. Tomographic entanglement indicators in multipartite systems,
B. Sharmila, S. Lakshmibala, and V. Balakrishnan
Quantum Inf. Process. **19**, 127 (2020).

Manuscript submitted for publication

1. Signatures of avoided energy-level crossings in entanglement indicators obtained from quantum tomograms,
B. Sharmila, S. Lakshmibala, and V. Balakrishnan
ArXiv arXiv:2006.13536 [quant-ph], (2020).

CURRICULUM VITAE

Name : B. Sharmila
Date of Birth : October 7, 1991
Nationality : Indian
Permanent Address : Nachiar Kudil, 32, Sundaresan Nagar
Chennai, 600095.
Tamil Nadu, India

Education:

2014- Ph.D. Physics, Department of Physics
Indian Institute of Technology Madras, Chennai.
Date of registration: July 2014.

2012-2014 M.Sc. Physics,
Indian Institute of Technology Madras, Chennai.

2009-2012 B.Sc. Physics, Women's Christian College(Autonomous)
Tamil Nadu, India.

DOCTORAL COMMITTEE

Supervisor: Dr. S. Lakshmi Bala
Professor
Dept. of Physics, IIT Madras

Members: Dr. Suresh Govindarajan
Professor
Dept. of Physics, IIT Madras

Dr. Sunethra Ramanan
Assistant Professor
Dept. of Physics, IIT Madras

Dr. R. Radha
Professor
Dept. of Mathematics, IIT Madras